High Frequency Surface Wave Radar Demonstrator

Presented by:
Johann Burger

Prepared for:
Assoc. Prof. D.W. O'Hagan and Assoc. Prof. A.J. Wilkinson

A dissertation submitted to the Department of Electrical Engineering, University of Cape Town, in partial fulfilment of the requirements for the degree of Masters of Science in Engineering.

September 25, 2018

Declaration

I know the meaning of plagiarism and declare that all the work in the document, save for that which is properly acknowledged, is my own. This thesis/dissertation has been submitted to the Turnitin module (or equivalent similarity and originality checking software) and I confirm that my supervisor has seen my report and any concerns revealed by such have been resolved with my supervisor.

Signature of Author : Signed by candidate

Cape Town
September 25, 2018

Abstract

High Frequency Surface Wave Radar (HFSWR) is used around the globe for the mapping of sea currents and coastal monitoring of the Exclusive Economic Zone. Decision to build an HF radar at the University of Cape Town (UCT) was made by Daniel O'Hagan and Andrew Wilkinson in February 2015 immediately after seeing a demonstration of the CODAR system at IMT. Their intention was subsequently discussed at several meetings, including a South African Radar Interest Group (SARIG) meeting and one at IMT in order to gauge interest and raise funding. There was both interest (mainly for ocean current monitoring) and scepticism (expressed by CSIR and SARIG members) of the value of HF radar for ship monitoring.

This reports the design, construction, test, and evaluation of the UCT HFSWR demonstrator. A modular approach was taken in its design and construction making it easy to replicate and upscale. A pillar of this work is to prove the feasibility of a software defined radar (SDR) based HF radar demonstrator.

Every part of the demonstrator was designed and constructed from scratch as UCT had no prior HF activities, and therefore no legacy antennas or components to utilise. A low-cost RF frontend follows the HF antennas, which were also designed for this project. Combined with an SDR platform known as the Red Pitaya (RP), a complete HF radar demonstrator was assembled and trials were conducted at the UCT rugby field and at the IMT facilities in Simon's Town. A preliminary assessment of the results reveal the effects of Bragg resonance scatter and detection of two stationary targets (mountains) distinguishable by both range and azimuth. This assessment of the results indicates that the demonstrator is operational.

For Reuben and Harriet.

Acknowledgements

I would like to first and foremost thank everyone in the Radar Remote Sensing Group (RRSG) at UCT for the many technical discussions, comments, and expert advice by both the staff and colleagues. You have truly demonstrated what peer learning is about.

My supervisors Daniel W O'Hagan and Andrew J Wilkinson who have given me expert guidance both technically and towards this Dissertation. Also for the support of publicity within SARIG and the larger radar and oceanographic community, and for the manual labour of carting around heavy equipment over long distances.

Tighe Barris whose own masters project fits neatly with my own. We wouldn't have a radar now if it weren't for your work on the Red Pitaya. Thomas Düsterwald who also did an interesting project in the realm of HF and who helped me with the Red Pitaya.

Zubeida Patel whose exceptional work on the broadband antenna truly helped push the project from theory to practice. Sayur Mahabeer who has kept the HF torch alive with his work on an improved RF switch and introduction to FMICW radar. Nicholas Antoniades who helped with the grunt work during my trials and constantly kept a positive attitude.

To one of my greatest friends Peter Bates who helped construct the antennas and who designed and 3D printed the end connectors for the conical antenna using his own home brew 3D printer.

To all the poor suckers who helped me with all the manual labour of setting up

antennas, running cables, and packing up afterwards. I just hope that I was equally as useful to you.

To Stephen Payne who has been able to answer every question I pose to him. And to Randy Cheng who helped me understand antennas and answered any questions I had during my course work. Both Stephen and Randy's exceptional work in the RRSG has ensured its good culture.

To Darryn Jordan from whom I had many discussions regarding radar concepts and signal processing issues. We managed to answer any challenging question. Michael Malape who has always been extremely helpful and who always showed an interest in my work. Philly Pilane who helped me understand concepts in Radar Cross Section.

To my parents who have had to endure an extra two years of putting up with me and to all my immediate family who have always been there for encouragement and advice.

I would also like to thank Telkom and the Centre of Excellence for funding my undergraduate and postgraduate studies and providing me with support when I needed it.

Contents

List of Figures

List of Tables

List of Symbols

c	—	Speed of light in a vacuum (3×10^8) [m/s]
g	—	Acceleration due to gravity in Cape Town (9.796) [m/s^2]
k	—	Boltzmann constant ($1.38064852 \times 10^{-23}$) [J/K]
SNR	—	Signal to noise ratio before signal processing [dB]
SNR_{proc}	—	Signal to noise ratio after signal processing [dB]
λ_c	—	Operating wavelength of radar [m]
f_c	—	Operating frequency of radar [Hz]
PRI	—	Pulse repetition interval [sec]
PRF	—	Pulse repetition frequency [Hz]
F	—	Noise figure [dB]
F_a	—	Noise figure due to external sources [dB]
f_a	—	Noise factor due to external sources [1]
B	—	Bandwidth [Hz]
T	—	Temperature [K]
T_0	—	Standard noise temperature (290) [K]
T_s	—	System noise temperature [K]
P_n	—	Noise power [W]
P_r	—	Target echo receive power [W]
P_t	—	Radar transmit power [W]
P_{avg}	—	Average transmit power [W]
τ_i	—	Coherent Processing Interval (CPI) [sec]
τ	—	Pulse length [sec]
$N_{integrate}$	—	Number of range lines integrated [1]
L_p	—	Free Space Path Loss (FSPL) or Norton path loss [dB]

G_t — Gain of transmit antenna [dBi]

G_r — Gain of receive antenna [dBi]

d — Array element spacing [m]

σ — Radar Cross Section (RCS) of a target [m^2]

D — Target ship's full load displacement [kilotonnes]

v_c — ocean surface current velocity [m/s]

Δf — Frequency shift between expected Bragg scatter Doppler frequency and actual Bragg scatter Doppler frequency [Hz]

f_D — Doppler frequency [Hz]

L — Wavelength of gravity wave component [m]

M — Refractivity

G_e — Total gain of receiver [dB]

G_n — Gain of n'th RF component in receiver [dB]

T_e — Equivalent noise temperature of receiver [K]

T_n — Noise temperature of n'th component in receiver [K]

v_B — Phase velocity of deep water gravity waves [m/s]

f_B — Doppler frequency as a result of Bragg scatter [Hz]

Nomenclature

HF—High Frequency band between 3 MHz and 30 MHz.

VHF—Very High Frequency band between 30 MHz and 300 MHz.

HFSWR—High Frequency Surface Wave Radar referring to radar exploiting surface wave propagation to achieve beyond the horizon ranges.

HFOTH—High Frequency Over The Horizon referring to radar exploiting sky wave propagation to achieve beyond the horizon ranges.

LoS—The maximum range not obstructed by the curvature of the Earth and still within Line of Sight.

OTH—Beyond the Line of Sight of the observer is Over The Horizon.

SARIG—South African Radar Interest Group.

RRSG—Radar Remote Sensing Group.

SDR—Software Defined Radio.

ADC—Analog to Digital Converter.

DAC—Digital to Analog Converter.

DDC—Digital Down Converter.

EEZ—Exclusive Economic Zone.

SNR—Signal to Noise Ratio.

FPGA—Field Programmable Gate Array.

DDS—Direct Digital Synthesis.

RP—The Red Pitaya device used for SDR synthesizing, recording, and processing.

RF—Radio Frequency.

Gravity wave—Ocean waves generated by gravity as the restoration force.

Bragg scatter—Constructive radio interference due to ocean waves with a wavelength of half the radio wavelength.

Direction Finding—Technique to determine the angle of arrival using magnitude and phase comparisons between two or more antennas.

FMCW—Frequency Modulated Continuous Wave.

FMICW—Frequency Modulated Interrupted Continuous Wave.

Norton path loss—Ratio of power captured by an isotropic receive antenna with the power transmitted by an isotropic transmit antenna in direct Line of Sight.

FSPL—Free Space Path Loss. Identical definition to Norton path loss.

Transmit chain—RF electronics that may include amplifiers and filters used for transmitting.

Receive chain—RF electronics that may include amplifiers, filters, and switches used to condition a signal before sampling.

Node—Part of the radar that contains a Red Pitaya and may include a transmit chain and two receive chains.

Element—Receive antenna and receive chain.

Pulse Interval—Interval of time where a pulse is transmitted and the reflections received. This corresponds to a PRI or range line.

Trial—Procedure of operating the radar and gathering the results.

HPA—High Power Amplifier.

LNA—Low-noise Amplifier.

BPF—Band-pass Filter.

BG— www.banggood.com retail electronics website.

CPI— Coherent Processing Interval.

RG58— Radio Guide 58 coaxial cable.

Chapter 1

Introduction

Ocean monitoring of the Exclusive Economic Zone (EEZ), the first 200 nmi (nautical miles) from the coast, is of great importance to oceanographers and the South African Navy. Oceanographers are interested in ocean current data, specifically the Agulhas current. The Navy require ocean current information prior to executing special operations missions and are also interested in monitoring and deterring illegal fishing and smuggling.

A radar is considered over-the-horizon (OTH) if it is capable of detecting targets beyond the radar line-of-sight (LoS), where the LoS is approximately 4/3 of the true horizon. This can be achieved by two different forms of propagation phenomena known as surface wave and sky wave. Both of these propagation phenomena are practically exploitable in the HF band between 3 MHz and 30 MHz.

It is proposed to develop an HFSW OTH radar to determine the feasibility of constructing a low-cost software defined radio (SDR) based demonstrator from scratch.

The next section will provide a background to the project, explaining in detail how the project came to be. The requirements of the project in the form of a problem statement is provided, leading to a project aim. The chapter is concluded with a plan of development which provides an outline of the rest of this dissertation.

1.1 Background

South African interest in an HFSWR capability stretches back quite a few years. In 2013, Don Barrick of CODAR [1] visited several potential radar locations around the coast of South Africa. The Agulhas coast received particular attention due to its importance to oceanographers. Prof. Frank Shillington and Prof. Mike Inggs were both involved in the initial effort to purchase HFSWRs from CODAR. Unfortunately, the modest amount of government funding that would have been required never materialise and to date, there is no commercial HFSWR deployed in South Africa, despite increasing demand. A 2015 SARIG meeting setup by D. O'Hagan intended to determine who among the local radar industry in SA would be willing to undertake the development of an HFSWR. All parties present declared their interest in the technology, but, understandably, none could commit to undertake to develop a system given uncertain economic conditions. O'Hagan and Wilkinson declared that they would create a Masters project on HFSWR. This project is the outcome of their initiative to develop an HF radar competency in South Africa.

1.2 Problem Statement

HFSWR is capable of mapping ocean surface currents by exploiting the Bragg scatter phenomena, making it a useful sensor amongst oceanographers. HF radar also has the advantage of detecting remote targets beyond the horizon (up to 200 km and beyond for certain systems) making this type of radar useful for surveillance of the Exclusive Economic Zone (EEZ) which is the first 370 km off the coast.

1.2.1 Oceanography and Climatology

Figure 1.1 illustrates the Agulhas current flowing down the east coast of Africa along the southwest border of the Indian Ocean where it approaches the Atlantic Ocean off the southern tip of Africa. At this point parts of the warm Indian Ocean water leaks current rings into the Benguela Current heading northward

and Agulhas current rings translate westward into the Atlantic Ocean along the Agulhas Extension. The complex features of the Agulhas Current along the coast of South Africa significantly affects global ocean circulation and as a result has an effect on global climate [2]. These complex ocean features and their consequences are of interest to oceanographers and climatologists from across the globe [3].

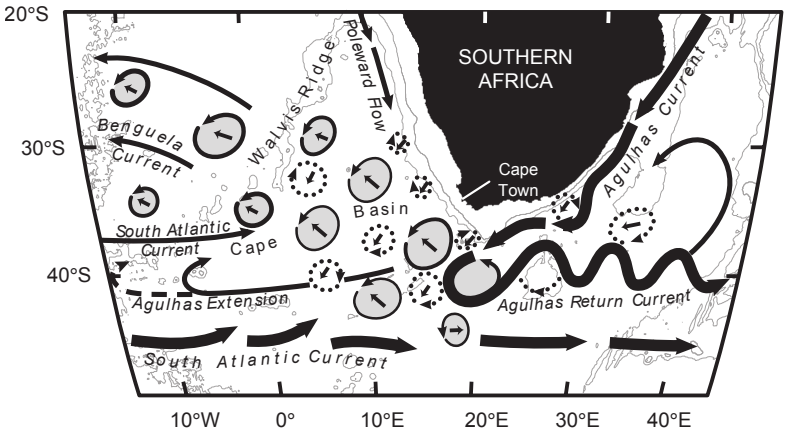

Figure 1.1: Map of Agulhas current along the east coast of South Africa along with the resultant leakage currents and retroreflection. Taken from [3].

Ocean current measurements along South Africa are measured with the aid of surface drifters and subsurface floats [3]. Surface drifters float on the ocean surface and travel with the currents while taking measurements such as location, salinity and temperature. The coordinates of the drifter are received over time via satellite and is used to determine the surface current velocity. A subsurface float is a floating device that is attached to a line moored into the ocean floor. Sensors are attached to the line that measure the ocean currents at different depths. A map of ocean currents can be stitched together with a combination of data gathered from drivers and floater current sensors and by using existing ocean models.

Many surface drifters and subsurface floats are required to get accurate and reliable data on ocean current sensing. These devices are however expensive to maintain and are prone to failure. Despite measurements from hundreds of surface drifters and subsurface floaters and decades of trials, measuring and mapping of the Agulhas current and its leakage currents with other currents around South Africa prove to be challenging. Surface drifters often fail before reliable current leakage

data can be acquired. Sparse data acquired by using multiple sensors relies on an accurate ocean model to be able to predict leakage currents and other features.

There is a clear need for an ocean current sensor by oceanographers and climatologists that can map the surface currents of a large area in real time.

1.2.2 Military and Coastal Monitoring

Maritime nations have exclusive rights to all the natural resources within the EEZ which is part of that nations blue economy [4]. South Africa's blue economy consists largely of fishing including that of abalone (perlemoen), hake, west coast rock lobster, squid and pelagics. Abalone is poached from South African waters and shipped overseas where it is considered a delicacy. All international voyaging ships with 300 or more gross tonnage along with all passenger ships, regardless of size, must relay their unique identification, position, course, and speed using an automated identification system (AIS) with accordance to the International Convention for the Safety of Life at Sea. AIS systems provide port authorities with a passive means of monitoring maritime traffic. A vessel with malice intent may easily turn off its AIS systems to prevent them from being monitored by port authorities which raises the need for an active sensing approach [5].

Monitoring of the EEZ in South Africa is dependent on patrols led by the department of environment and tourism and by law enforcement [4] along with cooperative vessels voluntarily communicating their intentions to local shore authorities. Considering that South Africa has 1.5 million square kilometers of EEZ, the task of monitoring the EEZ ocean using patrol is expensive and means that only small portions of the ocean surface can be monitored at a time.

Microwave radars are limited to LoS and when deployed for vessel surveillance usually comprise a large mast to extend their coverage. Detection range of microwave radar may extend to 70 km in cases when installed atop of tall cliffs. HFSWR can potentially provide an effective real-time, persistent and active surveillance of maritime targets far within the EEZ with an installation close to sea level.

1.3 Aim

The aim of this project was to construct a flexible HFSWR demonstrator for research purposes on a low-budget of approximately USD 1500 and using a modern software defined radar (SDR) platform. An SDR based approach has the potential to dynamically adjust the frequency of operation which is advantageous in a demonstrator that operates in a shared frequency band. The entire demonstrator was created from scratch: from conceptual design through to data processing and display.

An HFSWR demonstrator was constructed that can be set up along the coast and operated to detect large stationary targets at beyond the horizon ranges and that can measure ocean surface currents. Within the scope of this thesis, the operating frequency was between 12.5 MHz and 25 MHz constrained mainly by the increasing dimensions of the antennas and antenna array, and by the propagation loss. The project has fulfilled the objective of being feasible and has also been a conduit for developing competency in this technological domain.

1.4 Scope and Limitations

The objective of this project was to determine the feasibility that a low-budget SDR based HFSWR could achieve over-the-horizon performance. The designers specifically avoided setting performance criteria because part of the effort was to develop technical know-how and to determine its capability for HFSWR functionality.

The HF radar described in this report is an active quasi-monostatic pulsed radar. Fundamental radar concepts and equations are reproduced in this text, however derivations and explanations are referenced and not included in this dissertation. This includes topics such as the Doppler effect, pulse compression, and range and velocity ambiguities. The definitions for many of the fundamental radar parameters follows closely the definitions and theoretical development of Eaves and Reedy in [6].

The signal to noise ratio (SNR) of target echoes are explored in this report taking into account the surface wave propagation loss. Propagation loss is calculated using an external program called GRWAVE and is assumed to be accurate [7].

The HF radar described in this dissertation was assembled by the author although collaborative help was obtained from other students who focused on individual aspects of the radar. The SDR implementation on the Red Pitaya was done by [8] along with the Matlab scripts used to remotely control the Red Pitaya. The broadband conical antenna used on transmit was simulated, designed, and tested by [9]. The conical antenna [9] and digital transmitter and receiver implementations [8] are not within the scope of this project.

RF circuits and transmission line concepts were necessary for many of the components designed, constructed and tested in this project. Since the wavelength of HF is in the order of meters, many design requirements in RF circuits can be relaxed such as transmission line matching of PCB tracks and the need for specialised RF components.

The radar antenna array length is limited to approximately 50 metres resulting in one transmitter and six receivers. This limitation is due to several reasons: the limited space available at the Institute for Maritime Technology (IMT) test facility is limited to 50 metres, financial constraints limited the number of receivers to six, and larger setups will take longer to install.

Target detection and ocean current sensing is not within the scope of this dissertation however some of the theory for ocean current sensing is included in this dissertation along with preliminary attempts to detect large stationary targets (mountains) and to sense the Bragg scatter phenomenon.

1.5 Plan of Development

Chapter 2 explores the literature covered in this dissertation. An introduction to the different wave propagation models such as the flat Earth and spherical Earth models are outlined. Ocean phenomena unique to HF and Medium Frequency (MF) radar such as first and second order Bragg scatter are provided along with

a technique to calculate ocean surface currents using Bragg scatter. A review of existing HFSWR systems is provided.

The HFSW radar equation is derived in Chapter 3 and is compared to the conventional radar equation used in microwave radar. Surface wave propagation is expanded upon in this chapter where the GRWAVE package used for calculating surface wave path loss is introduced. Noise at HF is dominated by external noise and is considered in the signal to noise ratio. Chapter 3 concludes with radar equation results and comparisons with literature.

Chapter 4 contains all the details on the HFSWR demonstrator developed for this dissertation. The digital hardware [8] is first outlined. The RF frontend transmit and receive chains are then characterised with details provided on each component. Details on the conical antenna [9] is provided along with other antenna designs and considerations provided by the author.

Chapter 5 contains preliminary results of trials conducted at the Institute for Maritime Technology in Simon's Town and at the UCT rugby field.

Conclusions are drawn in Chapter 6 along with recommendations for improving the demonstrator.

Chapter 2

Literature Survey

Operating in the HF band has many advantages which intersect with the objectives of this project however special care must be taken when operating in this band. The HF band is from 3 MHz to 30 MHz which corresponds to a wavelength of 100 m to 10 m. Such big operating wavelengths means that circuits with relatively short transmission lines (a few centimetres) of mismatched characteristic impedance will have little effect on the overall network. Such large operating wavelengths also imply large antennas and real estate.

This chapter will begin with the IEEE definitions of the three different propagation schemes and will focus on surface wave propagation. Surface wave propagation is the dominant propagation mode in the HF band, and its over the horizon propagation range makes it the principal advantage of HF radar. Theory behind resonant Bragg scatter and its practical use in oceanography are also discussed. Other targets are also considered and some radar cross section (RCS) approximations are provided for maritime targets. This chapter finishes off with a review of existing radars such as SeaSonde, WERA and Raytheon's SWR-503.

2.1 RF Wave Propagation Models and HF Propagation

The most advantageous characteristic feature of operating in the HF band is the ability to exploit surface wave propagation and the low propagation loss experienced in this band. As a result, ranges of 20 to 200 km are achievebale with an installation height close to sea level. These ranges are well beyond the radio horizon of approximately 10 km for a practical installation height of 6 m above sea level. Space wave propagation - typically experienced in microwave radar - is compared with surface wave propagation in Figure 2.1 which is practically exploitable in the HF band (along with the VHF and MF bands [10]). Another mode of propagation used in HF is sky wave propagation which can also be exploited to achieve over the horizon ranges. Radars that exploit sky wave propagation are called HFOTH (High Frequency Over The Horizon) to distinguish them from surface wave radars referred to as HFSWR (High Frequency Surface Wave Radar). Sky wave radars detect targets at OTH ranges by receiving echoes that travel along the same sky wave path, allowing these radars to detect targets up to 3000 km away [11].

The history of wave propagation modelling can go as far back as 1893 [12] by Heinrich Hertz and Surface Wave propagation modelling was popularized by Sommerfeld in 1909 [13]. Widespread utilization was made possible by Norton who reduced Sommerfeld's expressions to graphs and extended the results to spherical surfaces.

The prior half of the 20th century consisted of controversy and disagreements regarding the physical and mathematical definition of a Surface Wave along with a sign mistake made by Sommerfeld [13] which remained unnoticed for a little over a decade. A historical background is important since concatenated errors makes fact checking challenging.

A more thorough historical background may be found in Barrick [14], Goubau [15] and the more recent paper by Wait [16] who all give a thorough historical account of the field. Other important papers and authors are explained in their respective subsections below. A more detailed analysis on path loss and surface wave path

loss is provided in Section 3.1.

2.1.1 Wave Propagation Definitions

One aspect that is not consistently defined in the earlier papers (prior to 1950) is the surface wave and its distinction from a space wave, ground wave and sky wave. The disagreements led to a much needed meeting amongst experts to agree on a suitable set of definitions. This meeting was set up by the Internatinal Scientific Radio Union (URSI) and was held in the late 1950's under the chairmanship of Wait. The set of definitions agreed upon were those defined by Norton [17, 18, 19] and are listed in the appendix of [16]. A physics approach of explaining the different waves is presented in [15].

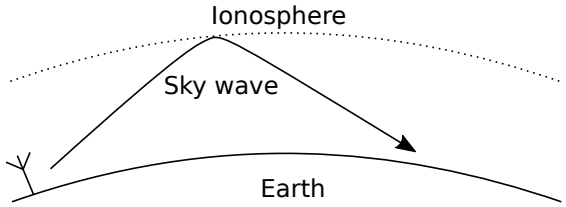

(a) Sky wave propagation

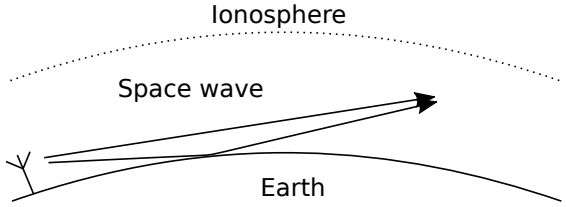

(b) Space wave propagation

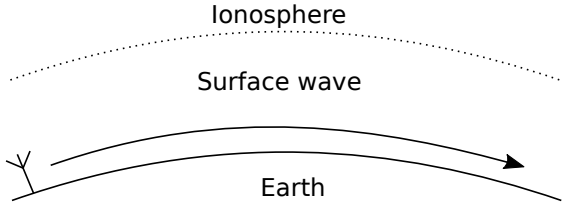

(c) Surface wave Propagation

Figure 2.1: Simplified illustrations of different propagation terms.

A wave radiated from an antenna above the Earth's surface will propagate towards another observation point above the Earth as a combination of sky wave and

ground wave components [20]. The sky wave component is a result of reflection from the ionosphere as illustrated in Figure 2.1(a). The ground wave component itself comprises of space waves and surface waves illustrated in Figures 2.1(b) and 2.1(c) respectively. The space wave component consists of the direct wave and ground reflect wave components. Direct waves are waves that propagate directly from the radiating source to the point of observation and the ground reflect waves are waves that appear at the point of observation after reflecting off the ground. Finally, surface waves are the remaining waves that exist at the observation point that are not a space wave or sky wave. More formally, a surface wave is "The propagating electromagnetic wave produced by a source over or on the ground. The Norton wave consists of the total field minus the geometrical-optics field" [20].

2.1.2 Flat Earth Model

The flat Earth model consists of two homogeneous media with a planar interface. One medium is conducting (Earth) and the other acts as an insulator (air). The radiating element in this model exists in the insulating medium. This model was solved by Sommerfeld [13] and later reduced to graphs suitable for engineering applications by Norton [17] [18]. The results from the flat Earth model became known as the Norton-Sommerfeld results [14] or simply as the Norton model [21].

The Norton-Sommerfeld model does not effectively represent a spherical Earth, however the results are a good approximation at distances within the optical region. At distances beyond the optical horizon, it is important to use the spherical Earth model.

2.1.3 Spherical Earth Model

Watson [22] was the first to treat wave propagation around a perfect electrical conducting (PEC) spherical Earth. The merit in Watson's solutions is his convergent residue series in the shadow region [16] which means Watson's results are useable at distances beyond the horizon. Watson's solution was extended to a finitely conducting Earth by Van Der Pol and Bremmer [23]. Norton took the problem

even further by taking into account the exponentially increasing refractive index of the atmosphere with height [19] and simplified the results to a set of graphs.

2.2 Measuring Sea Characteristics at HF

The complex ocean wave structure can be represented as the sum of waves with different direction, velocity and significant wave height. This sum can be narrowed down to three different physical phenomena resulting in capillary waves, wind waves and gravity waves [24]. Capillary waves are as a result of the water surface tension, typically have wavelengths of a few centimeters and are often referred to as ripples. Wind waves are as a result of persistent localised wind resulting in wavelengths in the order of ripples to that comparable to the longer gravity waves between 1.5 m and 1400 m [24]. The direction of the ocean currents in wind waves is in the direction of the wind, however the direction of the ocean currents often lag that of the wind by several hours. Gravity waves are generated by wind waves and can travel towards an area without the same wind conditions. Gravity waves propagate as a result of the force of gravity trying to restore equilibrium to an uneven ocean surface.

This section elaborates on the sensing of deep ocean gravity wave characteristics by the presence of Bragg resonance scatter.

2.2.1 Bragg Scatter

Sea clutter echoes from HF radars at low grazing angles result in resonant backscatter from ocean waves with lengths exactly half the radio wavelength. This phenomenon is similar to Bragg's law and hence ocean clutter resonating with the ocean wavelengths is known as Bragg scatter.

In the case of microwave radar where the wavelength is short compared to the ocean waves, backscatter will be received from capillary wave facets whose normals point towards the radar[25]. This is similar to scintillation reflection of the moon from rough water. The smaller ocean details are however masked by the larger wavelengths of HF. The longer ocean waves are as a result of gravity waves and will

appear to the HF radio wave as long smooth reflectors. Since gravity waves travel in the direction normal to its wavefront and its smooth appearance to HF radio waves, backscatter will only appear from those gravity wave components travelling directly towards or away from the radar and any other gravity waves will reflect echoes away from the radar.

Deep ocean gravity waves are those waves where the gravity wave's wavelength is comparable or smaller than the depth of the ocean water. The phase velocity of deep ocean gravity waves is clearly defined [25] and is directly proportional to the square root of the ocean wavelength:

$$v_B = \sqrt{\frac{gL}{2\pi}}, \tag{2.1}$$

where L is the ocean wavelength and g is the force of gravity which is approximately 9.796 m/s^2 in Cape Town. As illustrated in Figure 2.2, echoes from ocean waves that have a wavelength exactly half of the radar's operating wavelength (λ_c),

$$L = \frac{\lambda_c}{2}, \tag{2.2}$$

will add constructively forming a high resonance peak on receive. This resonance peak will have a Doppler frequency corresponding to the phase velocity of the resonant waves. Doppler frequency of a target moving at v [m/s] is derived as [6]

$$f_D = \frac{2v}{\lambda_c}. \tag{2.3}$$

The Doppler frequency of Bragg resonant gravity waves can be calculated by setting v in (2.3) to the phase velocity of gravity waves in (2.1) (v_B) and noting that the dominant gravity wave component that will be sensed by the radar is when (2.2) is obeyed [26]:

$$f_B = \pm\sqrt{\frac{g}{\lambda_c \pi}}. \tag{2.4}$$

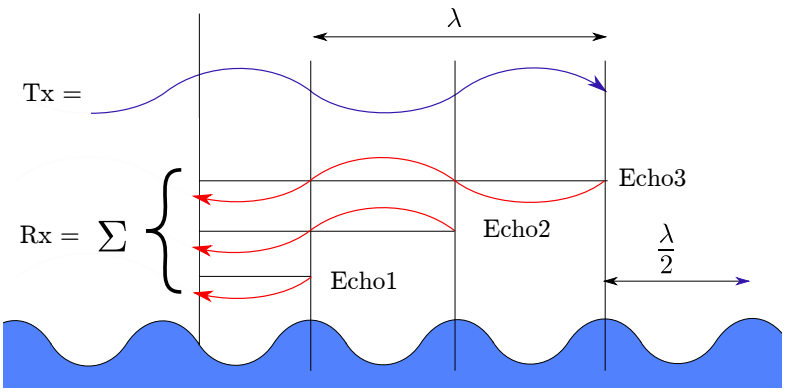

Figure 2.2: Illustration of Bragg scatter for HF radar. Echoes from ocean waves that have a wavelength exactly half of the radar's operating wavelength will add constructively forming a high resonance peak on receive.

2.2.2 Second Order Bragg Scatter

The Bragg scatter phenomenon is mostly dominated by gravity wave components that obey the Bragg scatter criteria in (2.2) and is referred to as first-order Bragg scatter. Resonant Bragg scatter may also arise due to multiple ocean wave components in the appropriate geometry. This is referred to as second-order Bragg scatter [10, 11] and can appear as peaks or a continuum in the Doppler power spectrum. Bragg scatter can occur over any area in which multiple reflections occur in phase within the range resolution of the radar (typically 500 m to 15 km).

Two causes of second-order Bragg scatter are shown in Figure 2.3. The first phenomena shown in Figure 2.3(a) is due to two wave trains that are exactly perpendicular to each other and that obey the relationship

$$\frac{2}{\lambda_c} = \frac{\cos\psi}{L_1} + \frac{\sin\psi}{L_2}, \tag{2.5}$$

where L_1 and L_2 are the ocean wavelengths of wave trains 1 and 2 respectively and ψ is the angle between the radial look angle and the velocity vector of the first wave train. The second ocean phenomena that causes second-order Bragg scatter is shown in Figure 2.3(b). Hydrodynamic interaction between crossing water waves results in a third set of interaction waves shown as dashed lines in Figure 2.3(b).

These interaction waves do not propagate freely, however they do contribute to second-order Bragg scatter as long as the interaction wave's wavelength is double the radio wavelength.

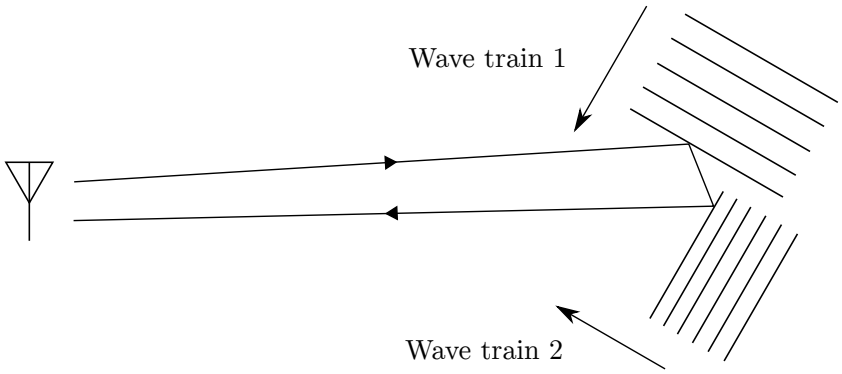

(a) Second-order Bragg scatter due to corner-reflector scattering.

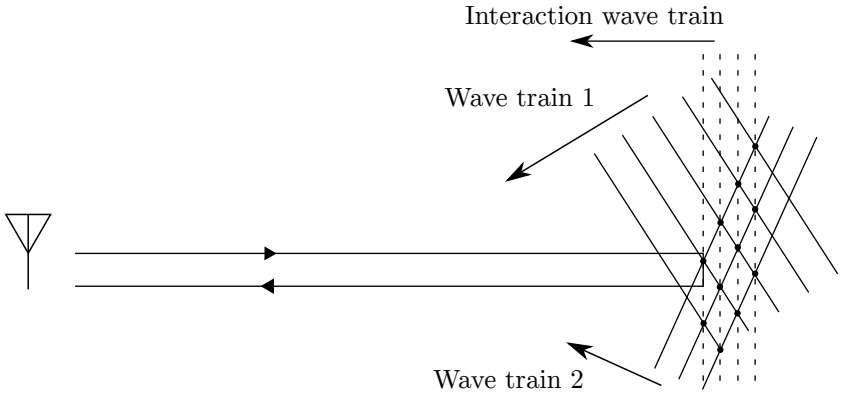

(b) Second-order Bragg scatter due to ocean wave interaction. Dashed lines represent the hydrodynamic interaction wave train causing Bragg scatter.

Figure 2.3: Two ocean phenomena that result in second-order Bragg scatter. Adapted from [10] and [11].

The combination of the ocean phenomena illustrated in Figure 2.3 result in second-order Bragg scatter present in the Doppler spectrum as extra peaks and a continuum. Further details of extracting wave information from the second-order scatter may be found in [10, 11, 25] and a tutorial on simulating the second-order Bragg Doppler power spectrum in MATLAB can be found in [27].

2.2.3 Ocean Surface Currents

Equation (2.4) implies that the position of the Bragg resonant peaks are dependent only on the operating wavelength. This assumes that ocean gravity waves only experience a phase velocity and that no surface current is present. With a surface current present, both the Bragg peaks defined in (2.4) will be shifted by a frequency shift defined by (2.3) where v is the radial velocity of the surface current. Ocean surface current velocity is an important ocean feature that can be sensed by HFSWR and is achieveable by measuring the frequency difference of the Bragg peaks from where they are expected to be (f_{Bragg}) to where they are measured (f_{peak}) as illustrated in Figure 2.4. This change in frequency (Δf) is used to calculate the surface current [28] using

$$v_c = \frac{\Delta f}{2\lambda_c}, \tag{2.6}$$

where $\Delta f = f_{Bragg} - f_{peak}$.

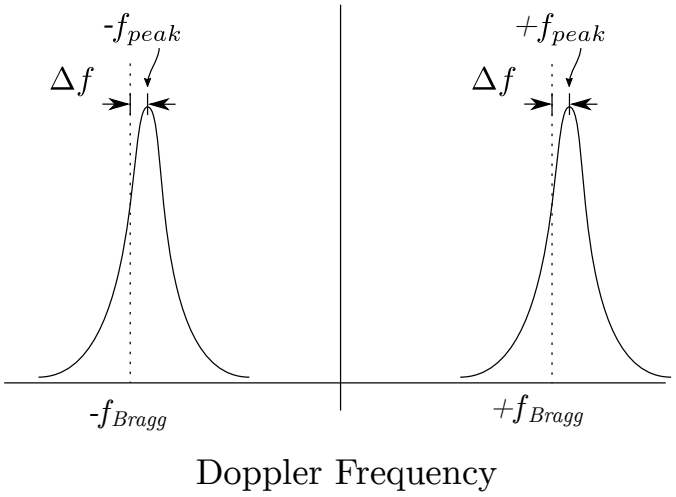

Figure 2.4: Simplified Doppler plot illustrating where the Bragg peaks are expected and how Δf is measured. Note that targets and second order Bragg scatter are absent from this Figure.

2.3 Measuring Targets at HF

The detectability of a target is determined by its radar cross section (RCS) which is a quantity in m^2 or dBsm (dB relative to a square meter) representing a fictitious area near the target where RF energy is absorbed and reradiated back to the radar. Targets may be submerged in sea clutter or ionospheric clutter. Targets of interest for EEZ monitoring include ships, aircraft, and missiles. These targets vary greatly in size and are comparable to the wavelength in HF. This influences the operating frequency considerations since the RCS of each target will vary greatly with different radar wavelengths. This section will discuss the three scattering regimes and focus on the Rayleigh and Mie regimes. RCS approximations for large and smaller vessels are also discussed.

2.3.1 Three Scattering Regimes

The direction of wave incidence and scatter field play a role on the RCS and for the case of monostatic radar both incidence and scatter field will be in the same direction. The RCS is also dependent on the materials and geometry of the target. Target geometry can be broadly broken up into three groups depending on its size (l) relative to the radio wavelength (λ_c): Rayleigh region, resonance region and optical region [29, 30, 31, 32]:

- Rayleigh, or low frequency region when the target's size is much smaller than the wavelength ($\lambda_c \gg l$)
- Resonant (Mie), or medium frequency region when the target's size is comparable to the wavelength ($\lambda_c \approx l$)
- Optical, or high frequency region when the target's size is much larger than the wavelength ($\lambda_c \ll l$)

These three regions are shown in Figure 2.5 for a perfectly conducting sphere. HFSWR utilizes vertical polarisation and therefore vertically tall targets will have a larger RCS. The wavelength for HF radar is in the order of tens of meters

which means targets will mostly be in the Rayleigh and resonant regions and predominantly in the latter.

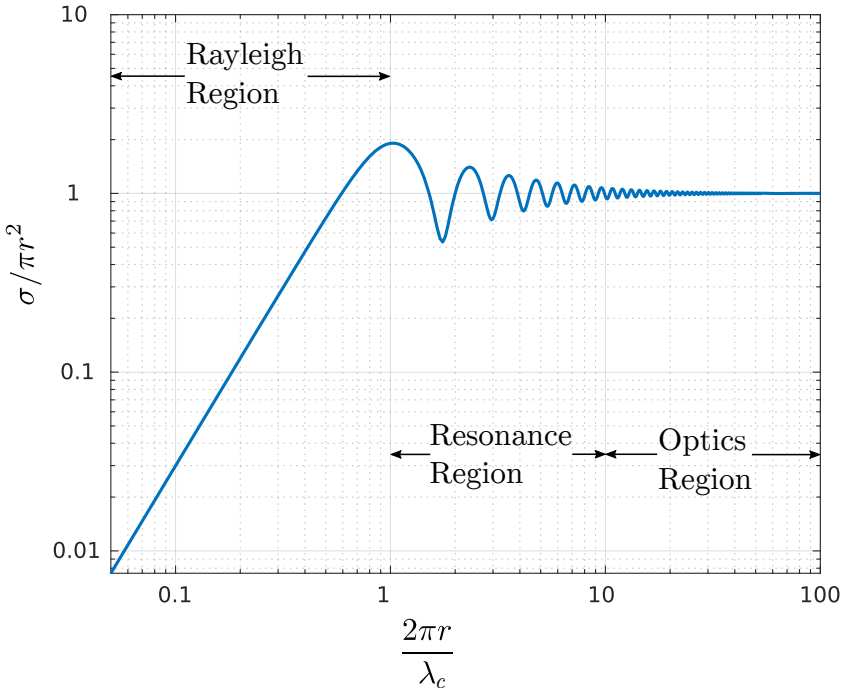

Figure 2.5: Scattering characteristics of a Perfect Electrically Conducting (PEC) sphere over the Rayleigh, resonance and optics regions. The y-axis is the RCS of the sphere normalised by its 2 dimensional area and the x-axis is the sphere circumference in wavelengths. Adapted from [30].

The **optics** region is the most studied due to the high presence of mirowave radar. In this region the target RCS is roughly the same as the physical size of the target and is investigated statistically for realistic targets. At HF, targets must be in the order of hundreds of meters for it to be considered in the optics region and therefore the optics region will not be considered further.

In the **Rayleigh** region very little phase variation exists between individual scatterers. As a result, a larger target (or a smaller operating wavelength) with more scatterers will have a larger RCS. The RCS of these targets are proportional to the fourth power of frequency ($\sigma \propto f_c^4$) and the target's volume squared ($\sigma \propto volume^2$). These proportionalities imply that targets much smaller than the wavelength ($\lambda_c \gg l$) have a much lower RCS than targets of size comparable to

the wavelength. For example, targets such as missiles, small fishing trawlers, and rubber duck boats often go undetected by HF radars. The target's RCS is influenced by its gross dimensions instead of its detailed structures and fluctuates less over azimuth [11]. Figure 2.6 illustrates the RCS of a triangular prism viewed by a radar with a wavelength an order of magnitude larger than the size of the prism (left) and with a wavelength four times smaller than the size of the prism (right). The RCS in the low frequency case has a significantly smaller RCS and fluctuates less over azimuth than that of the medium frequency case.

The RCS of a target in the **resonant** region can fluctuate significantly due to the high phase variation of the incident field over the length of the target. Lumped sections of a target can cause constructive and destructive interference which can cause a target to appear to have a larger or smaller RCS and may cause significant change in RCS over azimuth [30]. An interesting example of such a phenomena is presented by Sevgi [33] where he explains why a ship leaving a large oil platform will disappear from the radar when the ship is spaced a particular distance from the platform.

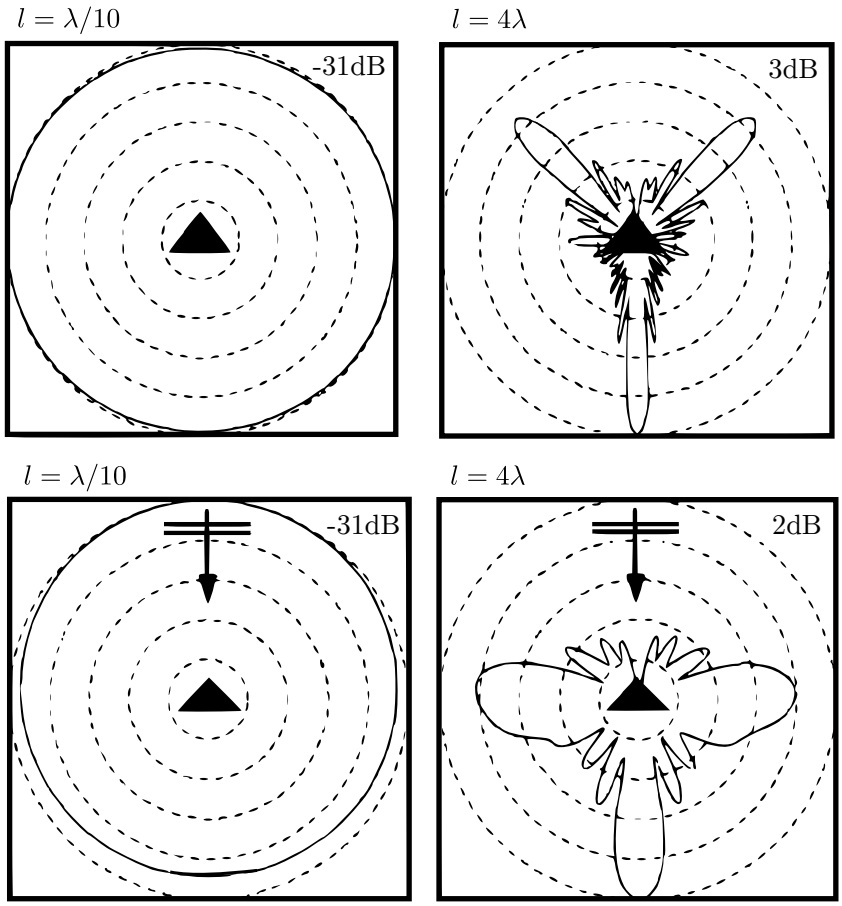

Figure 2.6: Angular RCS pattern of a triangular prism at two different operating frequencies in the resonance region. The size of the prism l relative to the operating wavelength is shown above each panel. The top two panels are for the monostatic case and the bottom two panels are for the bistatic case. Taken from [29].

2.3.2 RCS Approximations

The RCS of targets at HF have been studied extensively in [29, 32, 34] by means of Method of Moments (MoM) and Finite Difference Time Domain (FDTD) methods. An empirical approximation for the free space RCS of large vessels ($D > 1$ kilotonnes) can be calculated using [35]

$$\sigma = 52 f_{MHz} D^{3/2}, \tag{2.7}$$

where f_{MHz} is the radar operating frequency in MHz and D is the ship's full load displacement in kilotonnes.

The RCS of smaller vessels is determined by the size of their vertical masts and whether the mast is grounded or not. A grounded mast will approximate a monopole reflector whereas an isolated mast approximates a dipole. The RCS of a resonant monopole in free space is approximated as [26]

$$\sigma \approx \frac{(G\lambda_c)^2}{\pi}, \tag{2.8}$$

where G is the gain of a resonant monopole in free space. The RCS of a resonant dipole in free space is 6 dB greater than that of (2.8). The dipole considered in this scenario is not in free space but rather exists over a conducting surface (a metal boat electrically isolated from the saline ocean). As a result, only half the energy is captured by this dipole and, since a target scatterer must both capture and reradiate, the RCS of a dipole on top of a conducting surface is a quarter (-6dB) of the same dipole in free space. The RCS approximation of both a grounded and non-grounded mast on a ship are therefore equivalent. Approximating the RCS of a non-resonant monopole/dipole is derived from (2.8) and assuming that the RCS decreases by f_c^8 [26]. The approximate RCS for both cases appears in [26] and is plotted in Figure 2.7. The dashed curve in Figure 2.7 is the RCS of a resonant antenna calculated using (2.8) and the solid diagonal lines are the RCS of electrically smaller targets derived from the dashed curve and using the f_c^8 reduction approximation. As an example, a 6 m tall vessel is resonant at 12.5 MHz (red diagonal line) and the RCS of this target at 12 MHz is 17 dB (red horizontal

line). This example is used in the RCS calculations in Section 3.3.

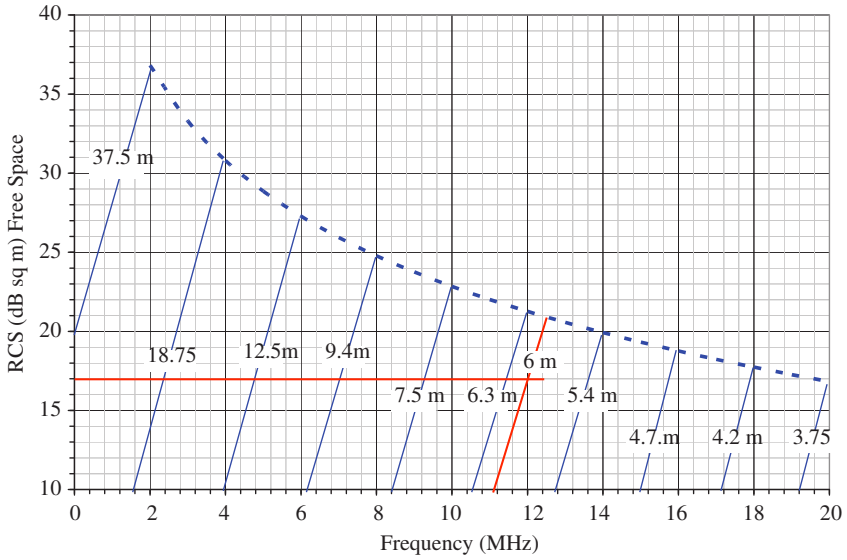

Figure 2.7: RCS approximation of smaller vessels where the vertical mast is the dominant scatterer. The dashed curve is the RCS of a resonant antenna calculated using (2.8) and the solid diagonal lines are the RCS of electrically smaller targets derived from the dashed line and using the f_c^8 reduction approximation. Taken from [26].

2.3.3 Target Detection in Sea Clutter

Sea clutter due to first and second order Bragg scatter can completely cover maritime vessel detections, especially when the targets are travelling at the same velocity as the phase velocity of the resonant (Bragg) gravity waves. The resonant gravity waves velocity (v_B) is calculated from (2.3) by making v the subject of the formula and making $f_D = f_B$ from (2.4):

$$v_B = \pm\sqrt{\frac{g\lambda_c}{4\pi}}. \tag{2.9}$$

For a radar operating at 16 MHz ($\lambda_c = 18.75$ m), the Bragg scatter peaks appear in the Doppler spectrum at $f_B = \pm\, 0.4079$ Hz or $v_B = \pm\, 3.826$ m/s. This velocity is comparable to the radial velocity of a ship and a target that does not want to be detected may take advantage of Bragg clutter to remain hidden.

The Doppler frequency shift due to a moving target calculated from (2.3) is directly proportional to the carrier frequency ($f_D \propto f_c$) whereas (2.4) indicates that the Doppler frequency due to Bragg scatter is directly proportional to the square root of the carrier frequency ($f_B \propto f_c$). An active solution to detect targets covered in Bragg clutter is to operate the radar at two different radio frequencies thus $f_D = f_B$ may be true at one radio frequency but not the other.

2.4 Existing HFSWR Systems

HFSWR has found two different target markets. National defence is interested in HFSWR OTH range capabilities along with target detection for monitoring the EEZ of that nation [4]. Oceanographers and climatologists are interested in HF radar for monitoring ocean currents, significant wave height and wave directional spectra [3].

HFSWR systems have been developed in the USA (CODAR), Germany (WERA), Canada (Raytheon's SWR-503), Australia (SECAR) [36], China (OSMAR2000) [37], and Japan [38]. CODAR and WERA are commercial systems developed for the use in Ocean current and sea state monitoring and are marketed towards oceanographers and climatologists however both systems claim to detect targets. Raytheon have developed a military grade HFSWR aimed at target detection. These radar systems are evaluated in this section.

2.4.1 CODAR

CODAR started at the NOAA (National Oceanic and Atmospheric Administration) by Barrick [1] after he noticed large sea echos present while developing a HFSWR for military use. CODAR was the first HFSWR developed purely for ocean current mapping and was the first to incorporate Direction Finding (DF) for azimuth discrimination as opposed to beam forming.

The original NOAA systems developed by Barrick consisted of a transmit YAGI antenna and a four element receive array in a DF square topology [39]. This system radiated 2.5 kW peak pulse power in 20 μs bursts every millisecond therefore

transmitting an average of 50 W. The operating frequency was 25 MHz. The receiver incorporated Sensitivity Time Control (STC). This system was capable of measuring ocean currents at a range of 70 km.

CODAR have since used a DF crossed-loop antenna design consisting of two orthogonal loop antennas and a whip antenna all colocated. Their initial design is pictured in an advert in Figure 2.8(a) and have since made the antenna far more compact in their SeaSonde design as pictured in Figure 2.8(b). The benefit of having such compact antennas was at the cost of poor antenna efficiency. A less efficient antenna captures less of the signal energy however since noise in HF is dominated by external noise, a less efficient antenna also captures less noise thus the Signal to Noise Ratio remains the same [31]. A numerical example is given in Section 4.3.7. This is exploitable up to a point when the receiver thermal noise starts dominating external captured noise.

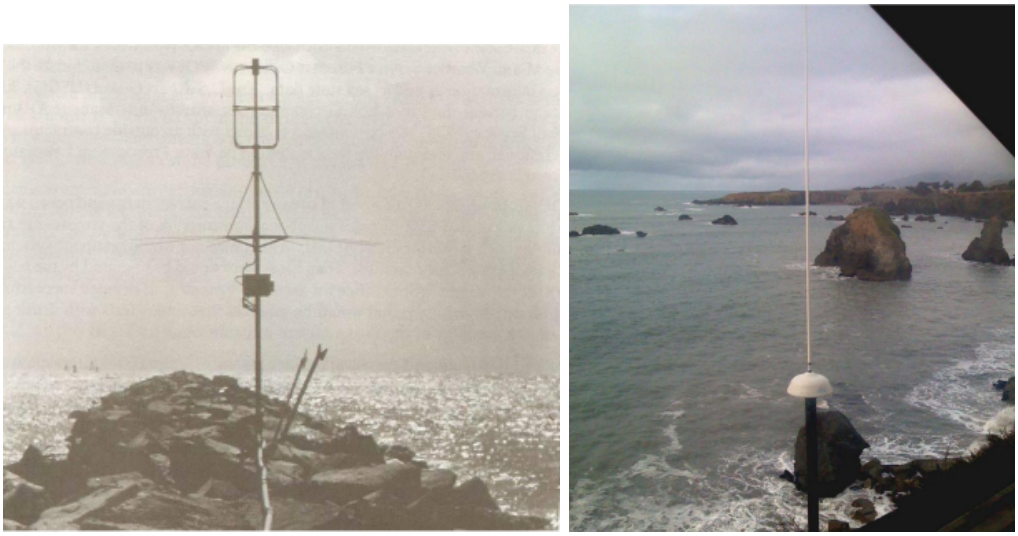

(a) CODAR commercial of the DF crossed-loop antenna [1]

(b) Latest SeaSonde DF crossed-loop antenna [1]

Figure 2.8: Compact DF crossed-loop antennas by CODAR. Taken from [1].

Technical Specifications of SeaSonde

The latest CODAR SeaSonde allows for three different configurations: Standard, Hi-Res and Long-Range. all configurations have a selectable angular resolution

between 1°and 5°. The output radiated power is 80 watts peak with an FMICW duty cycle of 50% [40].

Standard configuration operates with a center frequency between 11.5 MHz and 14 MHz or between 24 MHz and 27 MHz with a selectable bandwidth between 25 kHz and 350 kHz depending on the required range resolution. Achieveable range in this configuration is between 20 km and 75 km with a selectable range resolution between 200 m and 500 m. The transmit antenna is separate to the receive antennas and is 4.8 m high for 11 MHz to 14 MHz operation.

Hi-Res configuration can operate with a center frequency between 24 MHz and 27 MHz or between 40 MHz and 45 MHz with a bandiwdth above 350 kHz. Achieveable range using Hi-Res configuration is between 200 m and 500 m with a typical range between 15 km and 30 km. The transmit antenna is combined with the receive antenna.

Long-Range configuration operates between 4.3 MHz and 5.4 MHz with a bandwidth below 25 kHz. Achieveable range in Long-Range configuration is between 100 km and 220 km with a selectable range resolution between 3 km and 12 km. A separate transmit monopole 9 m high must be installed for this configuration.

Direction Finding

The beam patterns of all three antennas are illustrated in Figure 2.9. Define the received voltage waveforms as V_1 and V_2 for the blue and red beam patterns respectively and V_3 for the yellow beam pattern representing the monopole. Note that the beam patterns can be plotted as a function of look angle θ as $\sin\theta$ and $\cos\theta$ for the blue and red beam patterns respectively. The negative halves of the beam pattern (where $\sin\theta$ and $\cos\theta$ are less than zero) represents a 180° phase shift on the received waveform. A propagating wave approaching the antennas at angle ϕ will induce a voltage envelope at each antenna: $V_1 = A\sin\phi$, $V_2 = A\cos\phi$, $V_3 = A$. From these three equations it is possible to unambiguously calculate the direction ϕ.

A more practical way to understand DF is to compare the signs and magnitudes

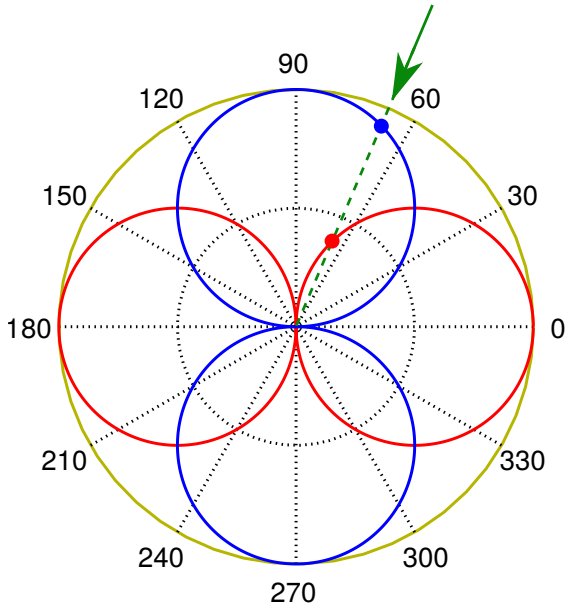

Figure 2.9: Beam pattern of the DF loop antenna design consisting of two orthogonal loop antennas (red and blue) and a whip antenna (yellow).

of the two received signals from the loop antennas. Considering the example in Figure 2.9 of the approaching wave at 65°, it is clear from comparing the voltage magnitudes of V_1 and V_2 that the signal is approaching either 65°or 245°. The sign of V_1 is positive when the signal is approaching from the North and is negative when it is approaching from the South. The sign of V_2 is positive when the signal is approaching from the East and is negative when it is approaching from the West. The sign of V_1 and V_2 therefore narrows down the angle of arrival to 65°. The signs of V_1 and V_2 can be derived by comparing their individual phases with that of V_3.

Recent Advancements

A major challenge faced by HF radar engineers is isolation between the transmit and receive antennas since directional antennas at HF are large. Isolation between the transmit and receive antennas are required when operating with an FMCW (Frequency Modulated Continuous Wave) scheme which has the benefit of requiring less peak power. CODAR were interested in using FMCW and at the same time wanted to keep their compact antenna design.

To solve this isolation issue, CODAR developed a scheme known as FMICW [41] (Frequency Modulated Interrupted Continuous Wave) which periodically interrupts the transmitted chirp while receiving. FMICW at 50% duty cycle has allowed CODAR to operate at 40 W average using a 80 W peak transmitter.

A more recent development by CODAR is including a GPS synchroniser to their radar [42]. This allows nearby SeaSonde to synchronise together and help mitigate interference when nearby SeaSonde are operating at the same frequency. Synchronisation of multiple SeaSonde's also allows for Multistatic configuration providing more useful data.

2.4.2 WEllen RAdar (WERA)

WERA, or WEllen RAdar, was developed at the University of Hamburgh as an alternative to CODAR for ocean current sensing [43]. The WERA system can provide azimuth discrimination using either Direction Finding (same as CODAR) or beam steering. WERA employs four monopole antennas in a square topology for transmit and a linear array of 2.5 m high antennas on receive. Frequency Modulated Continuous Wave (FMCW) is used for range discrimination which requires constant transmission. To avoid coupling between the poorly directional monopoles, the transmit antenna steers a null towards the receive antennas and the transmit and receive antennas are separated by at least 150 metres [44]. WERA's beamsteering approach [43] helps overcome some of the shortcomings of CODAR which can't reliably resolve wave-induced second-order spectral bands necessary for extracting more wave characteristics. A block diagram of the WERA system is illustrated in Figure 2.10 [43].

FMCW is achieved by using a common Direct Digital Synthesizer (DDS) between transmit and receive. Each of the 16 receive antennas are mixed coherently with the DDS generator to create 16 baseband IQ signals, all of which are quantized simultaneously using a 32 channel ADC. On each of the 32 channels is an anti-aliasing low-pass filter and a high-pass filter to suppress the direct path signal from the transmit antenna. Attenuating the direct path interference from the transmit antenna using a high-pass filter makes using FMCW without interruptions possible

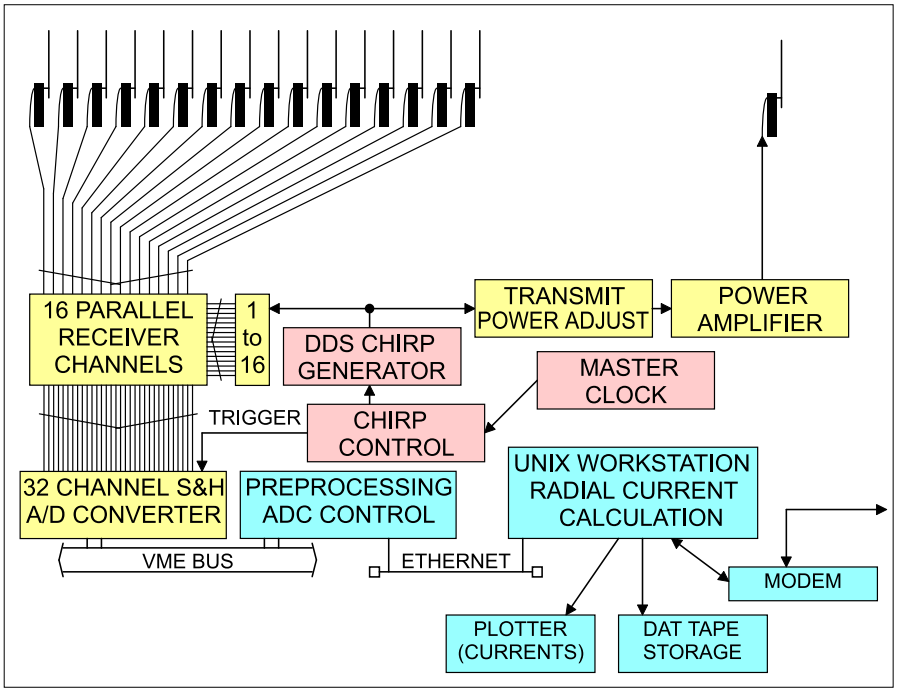

Figure 2.10: Block diagram of the WERA system taken from [43].

and reduces the required peak power on transmit, however this also requires that the RF signal be mixed down to baseband before being sampled. This requires extra analogue RF components adding extra complexity, cost and potentially more phase noise.

Technical Specifications of WERA

The latest WERA HF Radar can be set up in either compact or array type configurations [45, 46, 47] where both configurations require a separate transmit antenna. Compact configuration consists of only four receive antennas in a square topology with diagonal spacing of 5.42 m at 27.65 MHz, similar to that of the earlier CODAR HF Radar. This topology uses DF techniques for azimuthal resolution which can only be used to measure ocean surface currents and can not be used to measure other sea state characteristics such as significant wave height and wave directional spectra.

Array type configuration consists of a linear array of 8, 12 or 16 antennas. Using a

linear array allows the radar to measure ocean currents along with other sea state characteristics such as significant wave height and wave directional spectra. A greater number of antennas results in finer angular accuracy and a larger angular field of view as a result of a finer azimuthal beam width. The angular resolution is advertised to always be better than 1°.

WERA is capable of operating at MF, HF and VHF frequencies. Operating at a lower frequency allows for further range however has coarser range resolution and requires larger array element spacing. Higher frequencies provides finer range resolution at the expense of range. VHF frequencies are limited to LoS range.

When operating at 16.5 MHz WERA is capable of measuring ocean currents for 80 km and ships as far as 55 km. The range resolution at 16.5 MHz can be selected from options 3000 m, 1500 m, and 1000 m.

At operating frequencies between 24.5 MHz and 26.5 MHz WERA has an ocean current measurement range of 50 km and can determine wind direction from 35 km away. Advertised range resolution at these operating frequencies are 1000 m, 500 m, and 300 m.

Transmit Antenna

WERA use two rows of 2 element linear array antennas on transmit [48] as shown in Figure 2.11. The linear array spacing is 0.5λ and the two arrays are spaced by 0.15λ. All the antennas are attached to the same power amplifier via a power splitter and four cables of different length. Cables A and D are the same length and so are cables B and C. The difference in cable length (ΔL) between A, D and B, C is determined by $\Delta L = 0.35\lambda \times V$ where V is the propagation speed factor of the cable and is typically 0.66. The cables B and C must be longer than A and D.

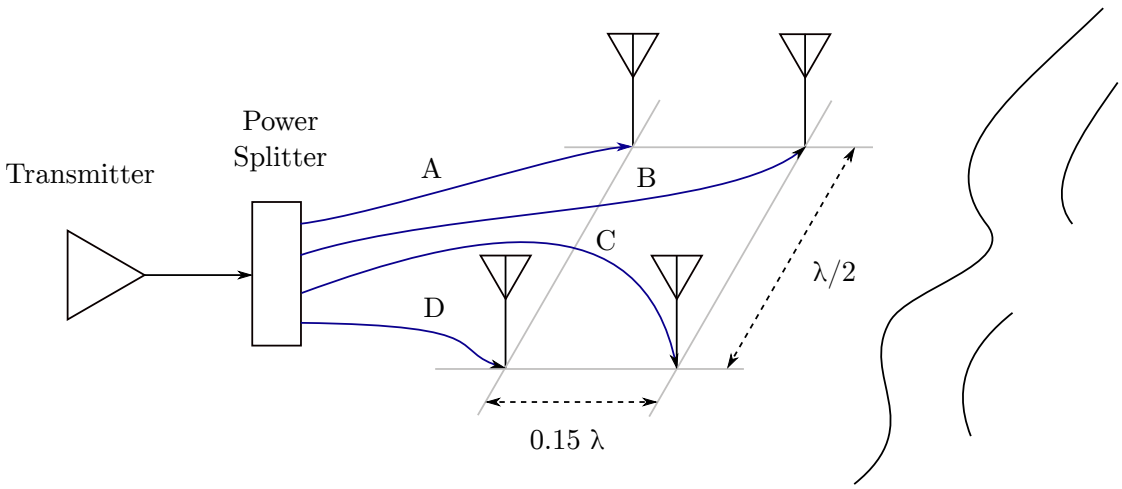

Figure 2.11: Illustration of the WERA transmit antenna. Adapted from [48].

2.4.3 Raytheon: Cape Race and Cape Bonavista to Third Generation Radar

Raytheon Systems Canada have over 20 years of HFSWR research and development experience. Their aim was to develop a military grade radar system in collaboration with the Canadian Department of National Defence that is capable of 24-hour, real-time, over the horizon surveillance of the Canadian EEZ. The result of this collaboration is the formation of the Integrated Maritime Surveillance (IMS) system which consists of a number of complementary sensors including a HFSWR called the SWR-503. A SWR-503 was installed in Cape Race and Cape Bonavista, Newfoundland in 1999 [49, 31, 50].

The SWR-503 in [49] operated between 3 MHz and 5 MHz with a bandwidth of 20 kHz using a waveform consisting of a sequence of phase codes. A 7-element log-periodic monopole was used on transmit with an approximate gain of 8 dBi and a peak and average transmit power of 16 kW and 1.6 kW respectively. An array of 16 monopole doublets were used for beam steering on receive to provide angular discrimination. Figure 2.12 is taken from [49] and shows approximate detection ranges for a variety of targets at different operating frequencies and is used to verify the author's range calculations in Chapter 3. The remaining radar parameters used in Figure 2.12 are those described above in this paragraph.

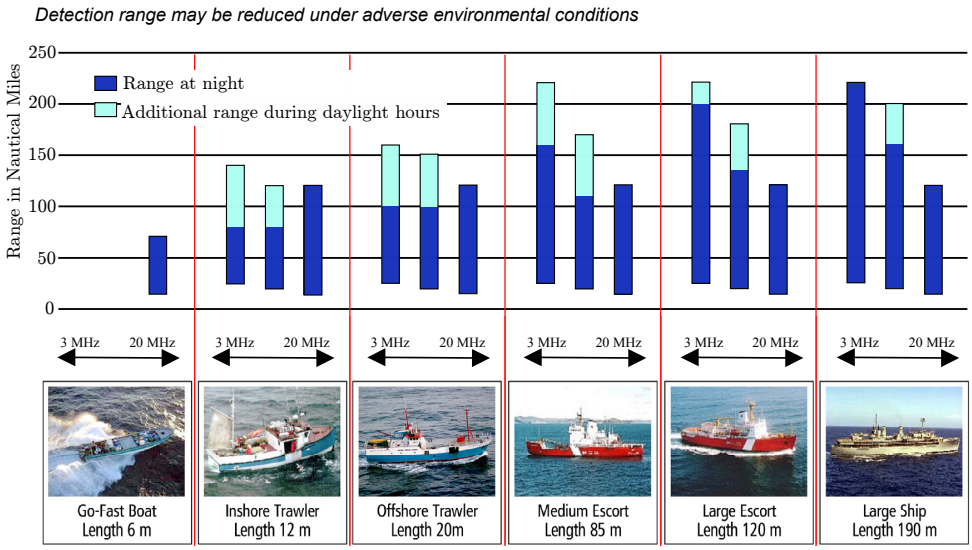

Figure 2.12: Typical detection ranges for HF radar. Taken from [49].

Processing Techniques

The primary target for a military HFSWR is small to large maritime targets and hence clutter and external interference must be suppressed [51]. Self-interference sources such as ocean clutter and ionospheric clutter is suppressed using sub-space-processing techniques exploiting the poor spatial correlation of ocean clutter. This processing technique was patented by Raytheon Canada Limited [52]. Figure 2.13 presents this processing technique by comparing the normal pulse Doppler map in Figures 2.13(a) and 2.13(b) with the pulse Doppler map after applying sub-space-processing in Figures 2.13(c) and 2.13(d) [49].

Co-channel interference from amateur radio users is a source of external interference that causes a significant impact on radar performance. This source of interference is mitigated by passing the recorded signal through a mismatch filter designed to suppress the radar echo resulting in a recording consisting of only interference [51]. This mismatched recording is subtracted from the original recording leaving only those components associated with the radar pulse behind.

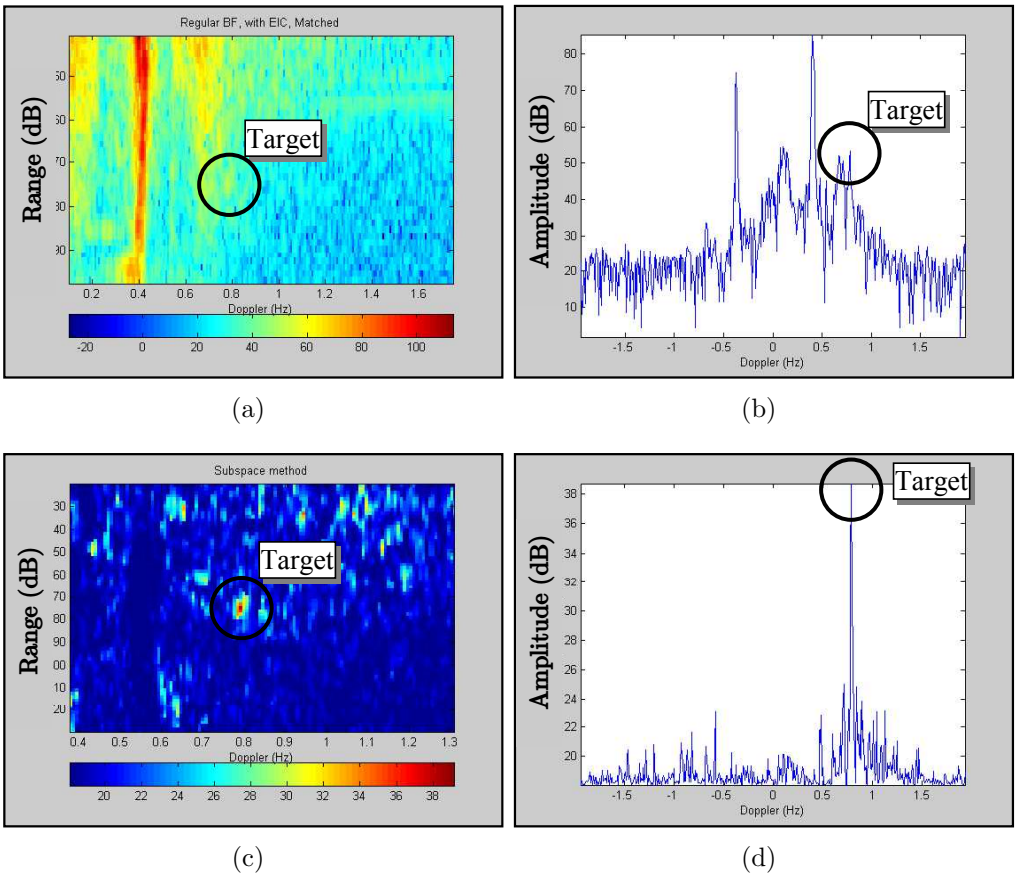

Figure 2.13: Example of applying sub-space-processing [52] to detect a small target. Subplots (a) and (b) show the target suppressed in Bragg scatter clutter and subplots (c) and (d) is the same data after sub-space-processing is applied. Taken from [49].

Third Generation Radar

The two SWR-503 radar systems in Newfoundland were decommissioned in 2007 due to the radar's co-channel interference with civillian HF communications operators. This initiated development on a new HFSWR demonstrator in 2011 for the Persistent Active Surveillance of the EEZ (PASE) [53]. This system employs a number of advances in radar technology since the deployment of the two SWR-503 in Newfoundland. The main objectives of PASE is reduced equipment and operational costs and to maintain no interference with HF communications. The first objective was achieved by making extensive use of COTS (Commercial Off

The Shelf) components, does direct sampling in RF and utilises SDR to replace many of the original analogue components.

Interference with HF communications was solved by implementing a Pro-Active Remote Intelligent Spectrum Management (PRISM) system. This system has a database of historical radio spectrum occupancy and a dynamic channel occupancy analyzer which together control the radar operating frequency. The radar itself can readily shift between bands.

Chapter 3

HFSW Radar Equation

The standard radar Signal to Noise Ratio (SNR) equation can be found in any radar textbook. This equation is well derived by Scheer in Principles of Modern Radar (PoMR) [6] amongst other popular radar texts. The assumptions made to derive the SNR radar equation in [6] are however not valid in the HF band due to the surface wave mode of propagation and the dominant external noise sources at HF.

The HF radar equation is derived starting from the one way free space path loss (FSPL) communications equation. Two way propagation is considered by using Norton's more generalised definition of path loss. Finally the HFSW SNR equation after pulse compression and coherent integration is derived. With the HFSW SNR equation defined, individual parameters such as path loss at HF and external noise are defined and justified. The chapter is concluded with radar range calculations done by the author and compared with the approximations done by [49].

3.1 Surface Wave Propagation Loss

It is often assumed in radar and radio engineering that the direct path between the transmitter/receiver and target is the most dominant term when calculating propagation. As discussed in Section 2.1, the direct path becomes negligible and the surface wave term supersedes the direct path when the target is beyond the

horizon. The FSPL term in the radar equation is discussed in this section as well as the steps taken to reduce the FSPL term to the more generalised Norton path loss definition [54].

3.1.1 Line of Sight Propagation

In radio communications, it is typical to calculate the one-way path loss between a transmitter and a receiver (such as in Figure 3.1) by first calculating the power density present at a distance R from the radiating source:

$$\Phi_t = \frac{P_t G_t}{4\pi R^2} \quad [W/m^2], \tag{3.1}$$

where Φ_t is power density due to the transmitter, R is the one-way path length,

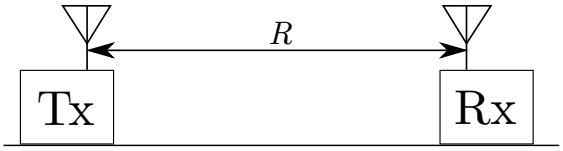

Figure 3.1: Typical wireless communications link between a transmitter and receiver.

P_t is the instantaneous transmit power and G_t is the transmit antenna gain. The power measured at the receiver antenna terminals is the product of the power density per unit area (flux) with the effective aperture area:

$$P_r = \Phi_t A_e = \frac{P_t G_t}{(4\pi) R^2} A_e \quad [\mathrm{W}], \tag{3.2}$$

where the effective aperture is

$$A_e = \frac{G_r \lambda_c^2}{4\pi} \quad [\mathrm{m}^2]. \tag{3.3}$$

G_r is the receiver antenna gain and λ_c is the operating wavelength. The power captured by the receiver in Figure 3.1 is

$$P_r = \frac{P_t G_t G_r \lambda_c^2}{(4\pi)^2 R^2} \quad [\mathrm{W}]. \tag{3.4}$$

3.1.2 Norton Path Loss

Transmission loss (also known as path loss, L_p) was defined by Norton [55] as the ratio of the received power and the transmit power assuming no system losses and isotropic antennas. Norton also derived the path loss in free space by setting the antenna gains in (3.4) to unity and rearranging to make the ratio of the transmit and receive power the subject of the formula,

$$L_p \equiv \frac{P_t}{P_r} = \left(\frac{4\pi R}{\lambda_c}\right)^2. \tag{3.5}$$

Expressing (3.5) in decibels with R_{km} in km and f_{cMHz} in MHz results in the standard telecommunications Free Space Path Loss (FSPL) formula:

$$L_p = 32.44 + 20log(R_{km}) + 20log(f_{cMHz}) \quad [dB]. \tag{3.6}$$

Norton's definition of path loss is commonly used in telecommunications due to its ease of use. The received power can be calculated simply by subtracting the path loss from the sum of the transmit power and antenna gains in decibels. This is equivalent to combining (3.5) with (3.4) resulting in

$$P_r = \frac{P_t G_t G_r}{L_p} \quad [W]. \tag{3.7}$$

In radar it is preferred to use (3.4) as opposed to (3.7) since range is one of the target parameters to be sensed. It should be noted that the FSPL can be easily calculated from (3.5) as long as the range and operating frequency are both known. This is not the case for surface wave propagation loss.

3.1.3 Two-Way Propagation

Another difference between communications and radar is that radar must consider two-way propagation. The two can be related when considering the target as a receiver (with an associated effective aperture) and a radiator. Starting over from (3.1) which is the radiated power flux from the transmit antenna, the radar target

will intercept a certain amount of power and reradiate this power depending on its size and geometry. The effective area that the target is capable of intercepting and reradiating is known as the RCS (σ) and is expressed in square metres. The effective isotropically radiated power from the target is

$$Q = \Phi_t \sigma = \frac{P_t G_t \sigma}{4\pi R^2}. \quad [\mathrm{W}]. \tag{3.8}$$

For the monostatic case, the propagation path from the radar to the target will be the same as the propagation path from the target to the radar. The power flux from the radiating target is therefore

$$\Phi_r = \frac{Q}{4\pi R^2} \quad [W/m^2]. \tag{3.9}$$

Similar to (3.4), the received power is the product of the receiver antenna's effective aperture with the power flux from the radiating target:

$$P_r = \Phi_r A_e \quad [W]. \tag{3.10}$$

Substituting (3.3), (3.8), and (3.9) into the received power (3.10) results in the well known radar equation,

$$P_r = \frac{P_t G_t G_r \lambda_c^2 \sigma}{(4\pi)^3 R^4}. \tag{3.11}$$

It is important to note that (3.11) assumes the radar and the target are in free space with no or few obstructions. This is a fair assumption when considering microwave radar where the radar antennas and targets are several wavelengths above the ground and the targets are within line of sight of the radar antennas. This is not the case for HFSWR where the antennas are within a wavelength above the ground and the target is shadowed from the radar behind the curvature of the Earth. Because the free space approximation is not feasable for HFSWR, it is important to remove the FSPL factors in (3.11) and use Norton's more general expression for path loss. More formally, the path loss can be generalised by replacing the two way FSPL factor $\left(\frac{4\pi R}{\lambda_c}\right)^4$ in (3.11) with L_p^2 by using (3.5). A more general form of

(3.11) with no assumptions to the mode of propagation is

$$P_r = \frac{P_t G_t G_r \sigma (4\pi)}{L_p^2 \lambda_c^2}. \tag{3.12}$$

3.2 HFSWR Signal to Noise Ratio

At frequencies above HF, the most dominant noise is due to thermal agitation causing random electron motion. Thermal noise power is mostly present in the receiver components and is calculated as

$$P_n = kT_sB = kT_0(F-1)B,$$

where F is the noise figure, T_s is the system temperature given by $T_0(F-1)$, B is the receiver bandwidth and k is Boltzmann's constant (1.38×10^{-23} [J/K]). The product kT_s is the power spectral density of thermal noise and is assumed constant over all frequencies. Thermal noise can be found in the radar's amplifiers, filters, cables and other subsystems. This means that target detection can always be improved by acquiring better quality (low-noise) equipment or by keeping the amplifier's temperature low. The signal to noise ratio (SNR) without signal processing is

$$SNR = \frac{P_t G_t G_r \sigma (4\pi)}{L_p^2 \lambda_c^2 (kT_sB)}. \tag{3.13}$$

A linear FM chirp has a pulse compression gain derived by its time-bandwidth product (τB) [6] and coherent integration gain is simply the number of pulses $N_{integrate}$ that are coherently integrated. The average transmitted power is the product of peak power with duty cycle ($P_{avg} = P_t\delta$) where duty cycle (δ) is a function of the pulse length and the PRF ($\delta = \tau \cdot PRF$). The number of coherently integrated pulses ($N_{integrate}$) is the integration time (τ_i) multiplied by the PRF ($N_{integrate} = \tau_i \cdot PRF$). Thus the SNR of incorporating integration gain may be expressed as

$$SNR_{proc} = \frac{P_{avg}}{\delta} \frac{G_t G_r \sigma (4\pi)}{L_p^2 \lambda_c^2 (kT_sB)} \Big(\frac{\delta}{PRF} B \Big) (\tau_i \cdot PRF),$$

$$SNR_{proc} = \frac{P_{avg} G_t G_r \sigma (4\pi) T_i}{L_p^2 \lambda_c^2 (kT_s)}. \tag{3.14}$$

The remainder of this section will elaborate on external noise and will explore all the parameters in (3.14)

3.2.1 HF Noise

In the HF band, the dominant noise source comes from external sources such as cosmic, galactic and man-made noise. The ITU [56] define the external noise factor (f_a) as the available noise power captured by an antenna relative to the thermal noise power from a matched source resistor of standard temperature ($T_0 = 290$ [K]),

$$f_a = \frac{P_n}{kT_0 B}. \tag{3.15}$$

The external noise figure (F_a) is the external noise factor expressed in decibels ($F_a = 10log(f_a)$) and is plotted over frequency in Figure 3.2. Equation (3.14) requires the noise spectral density N_0:

$$N_0 = f_a kT_0 = T_n k \ \ [\text{W/Hz}],$$

or expressed in dBm/Hz,

$$N_{0dBm} = F_a - 174 \ \ [\text{dBm/Hz}],$$

where F_a is extracted from Figure 3.2. The most dominant noise source is considered by extracting the data on the red curve in Figure 3.2.

External noise measurements were taken from the Menzies building in the Department of Electrical Engineering at UCT using the conical antenna discussed in Section 4.4 with no matching circuit and attached to an Agilent E4407B spectrum analyzer. The spectrum analyzer bandwidth resolution and video bandwidth were both set to 1 kHz and averages power over 10 sweeps. The antenna's frequency response was taken into account by adding the loss due to reflections in dB over

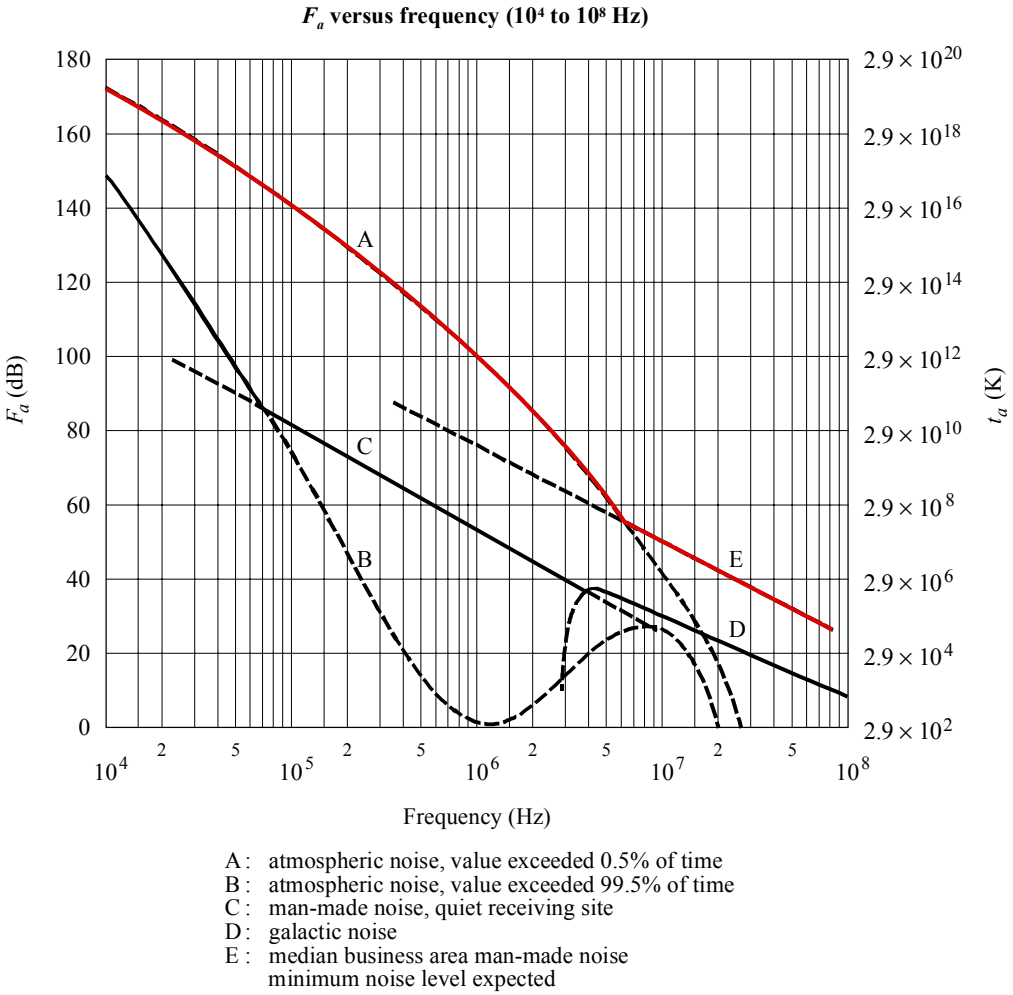

Figure 3.2: Global mean noise figure plotted over frequency [56].

frequency. The power loss due to antenna reflections is calculated as

$$L_{ref} = 1 - \rho(f)^2, \tag{3.16}$$

where $\rho(f)$ is the reflection coefficient of the antenna across frequency. The inverse of (3.16) is multiplied with the measured noise power to cancel out the reflection loss. Reflection loss cancellation is plotted in dB in Figure 3.3. This method of cancelling reflection loss is less accurate outside the operating frequency range of the antenna where the thermal noise of the spectrum analyzer becomes the dominant noise source. Antenna resistive losses are not taken into account.

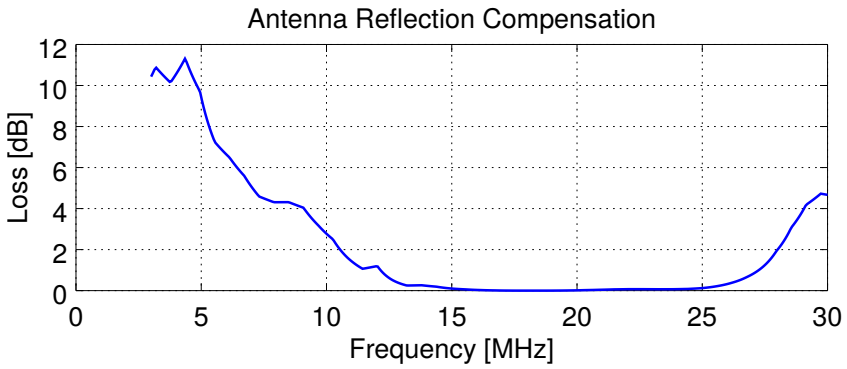

Figure 3.3: Antenna reflection loss compensation calculated from the inverse of (3.16) and $\rho(f)$ measured using the Agilent Field Fox on the antenna used for the noise measurements. This compensation is added to the measured noise power and the result is the blue curve in Figure 3.4.

The derived external noise power spectral density outside of the Menzies building is plotted in Figure 3.4 in blue along with the ITU recommended power spectral density in red. The local peaks from the blue plot in Figure 3.4 is due to other spectrum users.

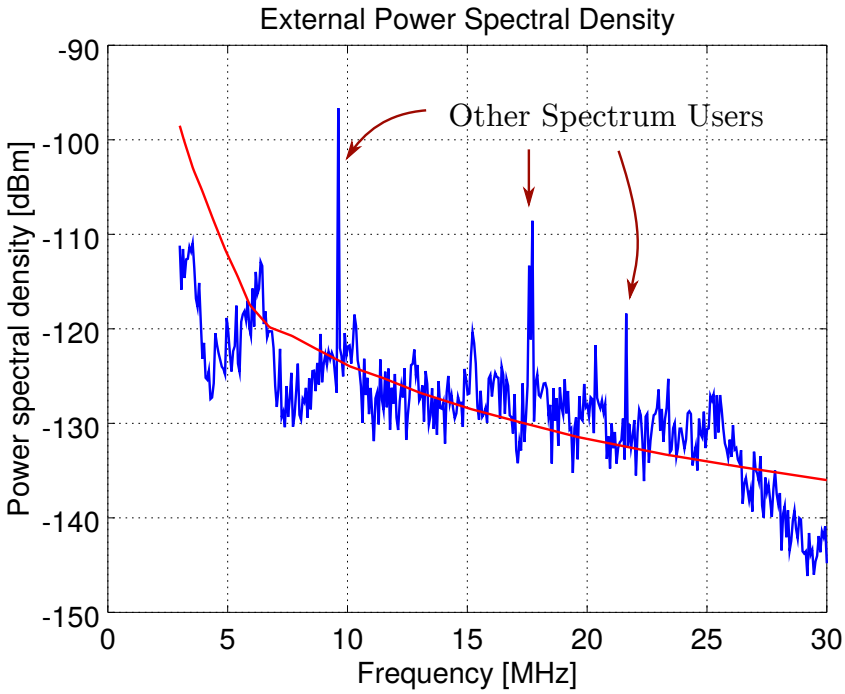

Figure 3.4: Noise power spectral density in dBm recorded from outside the Menzies building (blue) plotted with the ITU [56] recommended power spectral density (red).

3.2.2 Integration Time

The integration time τ_i, also known as dwell time or coherent processing interval (CPI), improves the Doppler resolution and increases the SNR linearly with time. The CPI must be long enough to detect a target suppressed under high external noise and to have a fine enough Doppler resolution to sense the mHz Doppler shifts due to ocean currents. A CPI that is too long will cause range and Doppler smearing for fast moving targets. These conflicting requirements means that the CPI must be changed depending on its purpose. For example, the CPI for detecting aircraft using HF radar varies from $\tau_i = 1$ to 4 seconds and for ship detection $\tau_i =$ 10 to 40 seconds or greater [11]. These CPIs are up to 1000 times longer than those used by microwave radar which is attributed to the coarse range resolution of HF radar [11]. For ocean current sensing the CPI is in the order of $\tau_i = 200$ to 400 seconds and multiple (typically 13) CPI power spectrums are incoherently

averaged [10] resulting in a total recording time between 30 minutes and a couple hours.

3.2.3 Propagation Loss

The ITU recommend a program called GRWAVE [57, 58] to calculate one way path loss using the Wait model for the shadow region and the flat-earth model for the near region. GRWAVE outputs the transmission loss between a transmit and receive antenna based on the following input parameters:

- Carrier frequency
- Relative permittivity of surface
- Conductivity of surface
- Polarisation
- Transmitter height
- Receiver height
- Range
- Refractivity of troposphere at surface of the Earth (designated as M)
- Scale height of the troposphere

Design parameters include the carrier frequency, transmitter and receiver heights and range. The boundary conditions of a PEC (Perfect Electric Conductor) states that the electric field along the surface of the PEC must be perpendicular to the surface. The radiated electric field must therefore be vertically polarized to allow SW propagation along the highly conductive saline ocean. The relative permittivity and conductivity of the surface are set to that of the saline ocean (70 and 5 S/m respectively).

Refractive index is the ratio of the velocity of an electromagnetic wave in a vacuum to its velocity in a specified medium. An EM wave bends as it passes between

two mediums with different refractive indexes. An EM wave that travels from a medium with a lower refractive index to a medium with a higher refractive index will bend closer to the normal of the surface of the two mediums and will bend away from the normal if the mediums were swapped. The parameter M, known as refractivity, is preferred over refractive index when dealing with air since the refractive index of air does not vary far from 1 (the refractive index of air at Standard Temperature and Pressure is 1.000277). If refractive index is m, then refractivity is defined as,

$$M = (m - 1) \times 10^6 = \frac{77.6}{T}(\Gamma + 4810\frac{e}{T}) \tag{3.17}$$

where Γ is atmospheric pressure in hPa, e is the water vapour pressure in hPa (inversely proportional to temperature) and T is temperature in Kelvin. Equation 3.17 shows an inversely proportional relationship with temperature and a strong dependence on water vapour pressure. Since atmospheric pressure (Γ) decreases exponentially with height, so too does the refractivity. It is well established in [59] that the mean dependence of the refractive index is defined by an exponential law. The refractivity at the Earth's surface M_s of height h_s can be calculated using,

$$M_s = M_0 e^{-h_s/h_0} \tag{3.18}$$

where M_0 and h_0 are reference refractivity and heights. The ITU [60] provide recommendations for M_0 at a fixed reference height h_0 of 7.35 km and is shown in Figure 3.5. An average refractivity of $M_0 = 335$ has been chosen. Since the SW radar will be located as close to the coast as possible, the height above sea level will be approximately zero resulting in $M_s = 335$.

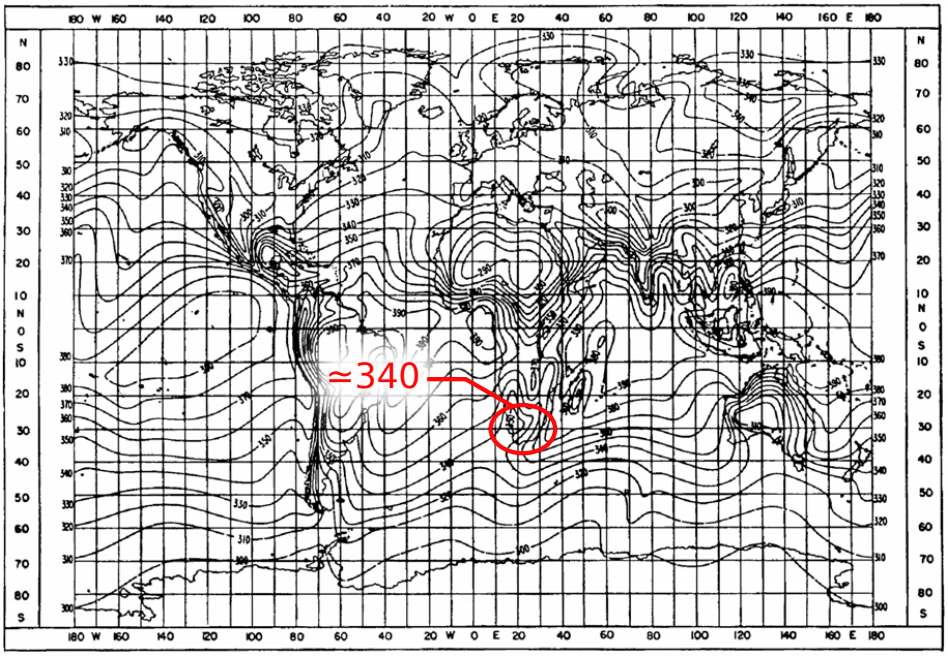

(a) Monthly mean values of M_0: February

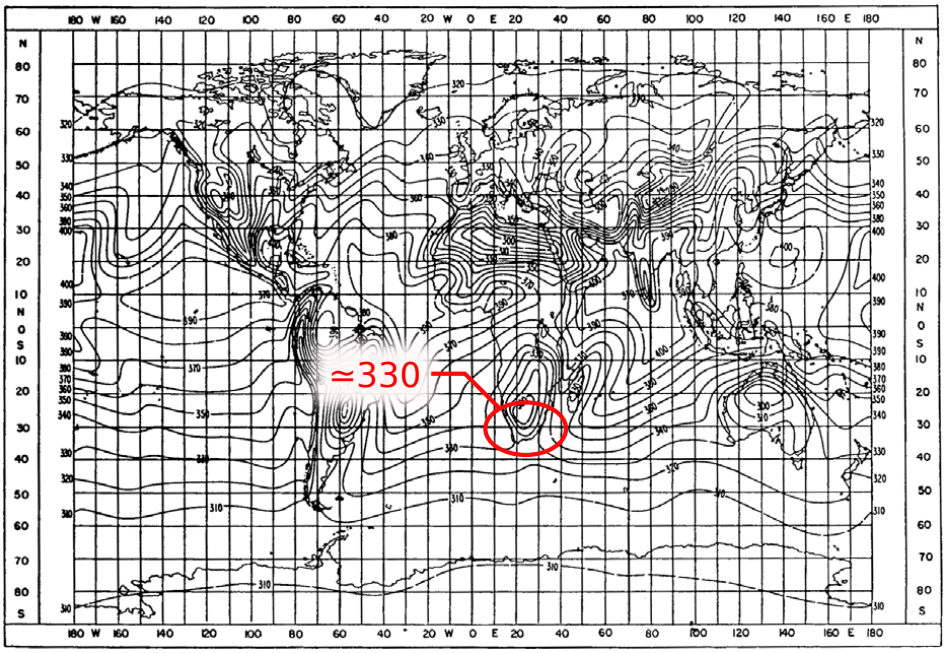

(b) Monthly mean values of M_0: August

Figure 3.5: Monthly mean values of M_0 at different parts of the world. Marked in red is an approximate value for M_0 along the coast of South Africa. Taken from [60].

The GRWAVE predicted path loss for different carrier frequencies is plotted in Figure 3.6. The transmitter and receiver heights above sea level are both set to one metre since the transmitter and all receivers were set up as close to the sea as possible. The results in Figure 3.6 indicate that the propagation loss increases with range and frequency as expected.

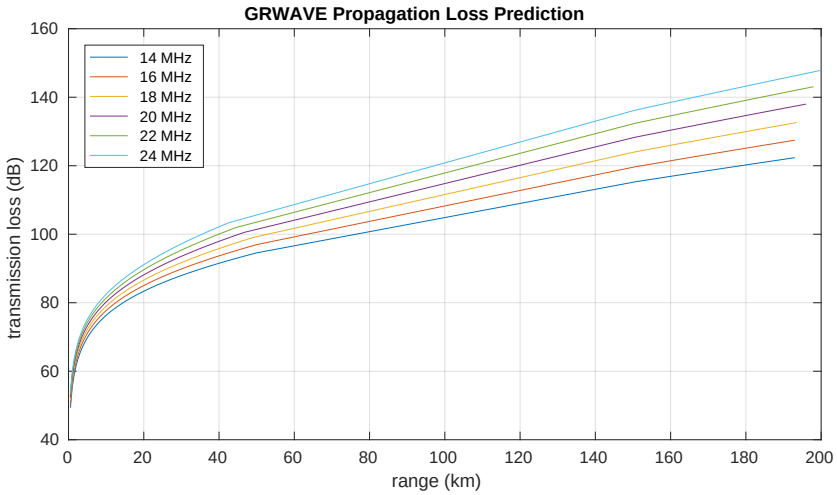

Figure 3.6: GRWAVE path loss prediction plotted over range for different carrier frequencies.

Added propagation loss due to ocean roughness was investigated by Barrick and a thorough set of results was plotted for center frequencies 5 MHz, 7 MHz, 10 MHz, 15 MHz, 20 MHz, 30 MHz, and 50 MHz and for sea states 1, 2, 3, 4, 5, and 6 in [14]. Both the Neumann-Pierson and Phillips isotropic ocean wave spectrum models were used in [14] to calculate the added propagation loss. The SNR results plotted in Section 3.3 uses the Phillips isotropic ocean wave spectra to calculate propagation loss since this model does not depend on wind direction from look angle. An example of the added propagation loss due to sea state at 15 MHz is plotted in Figure 3.7.

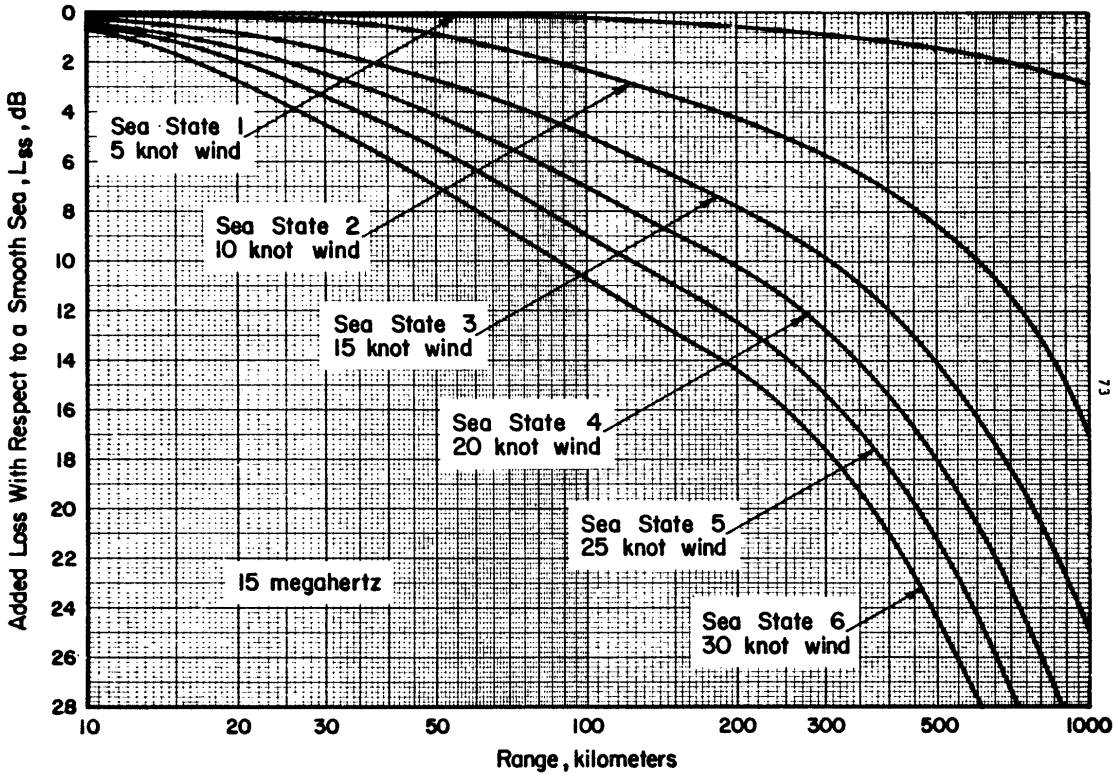

Figure 3.7: Added transmission loss due to sea state at 15 MHz. Antennas are located just above the surface. Phillips isotropic ocean-wave spectrum. Taken from [14].

3.3 SNR Results

Equation (3.14) was implemented in MATLAB with P_r as the subject of the formula and plotted over range. The Raytheon Cape Race setup discussed in Section 2.4.3 is used as a comparison. Figure 2.12 is taken from [49] which also provides the parameters of the HF radar set up in Cape Race. Its operating frequency is selectable between 3 MHz and 5 MHz, transmit antenna has a gain of 8 dBi, peak transmit power of 16 kW and bandwidth of 20 kHz.

The USNS Salvor (T-ARS-52) is used as a case study. This ship has a length of 78 m and a full load displacement of 3,300 tonnes which corresponds to an approximate RCS of 1250 m^2 at 4 MHz using (2.7). The USNS Salvor falls under that of a medium escort in Figure 2.12. Required transmit power over range of the

Cape Race HF radar with the USNS Salvor as the target is plotted in Figure 3.8 along with a horizontal red line at 16 kW. The two graphs in Figure 3.8 intersect at 338 km (181 nautical miles). This is in agreement with 2.12 during daylight hours.

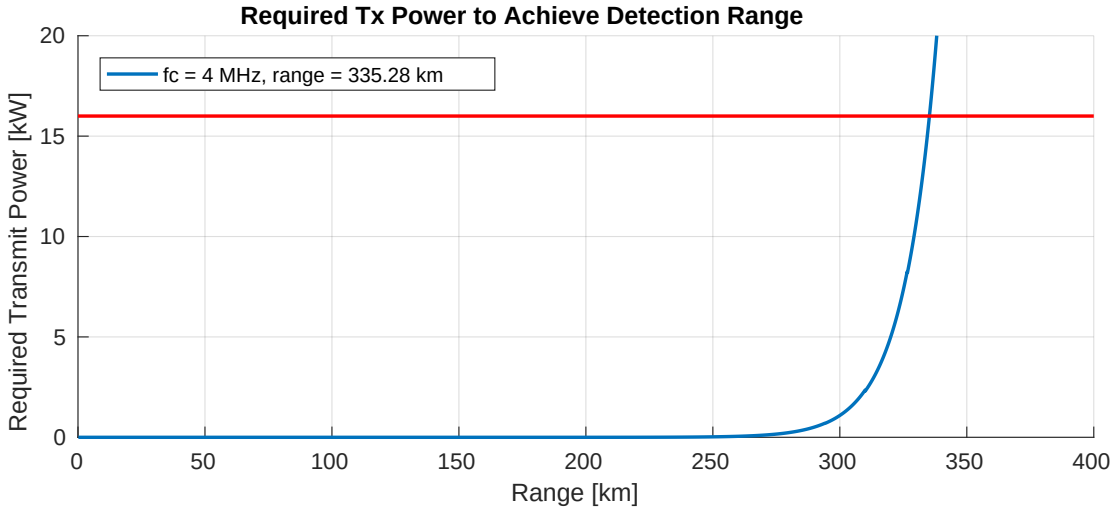

Figure 3.8: Transmit power required to detect the USNS Salvor over range at 4 MHz. The horizontal red line intersects at 16 kW.

Another example provided is that of an offshore trawler (tuna longliner). The trawler considered is 23.8 m long and its height above the ocean is approximately 6 m high which is resonant at 12.5 MHz. The RCS of this target is shown in Figure 2.7 in red and is approximately 17 dB. The required transmit power over range of this target is plotted in Figure 3.9 and the intersection is at 201 km (108.5 nautical miles). This is in agreement with 2.12.

SNR calculations are also done for the UCT radar and is shown in Figure 3.10 at different operating frequencies. The target is assumed to be the USNS Salvor. Other radar parameters include: peak transmit power of 300 W is assumed, bandwidth of 150 kHz, transmitter gain of 5.2 dBi (monopole), receiver antenna gain of 15.3 dBi (calculated at 16 MHz and steered 30° from broadside), PRI of 500 µs, integration time of 40 s, and pulse length of 30 µs. These results do not take system losses and sea clutter into account.

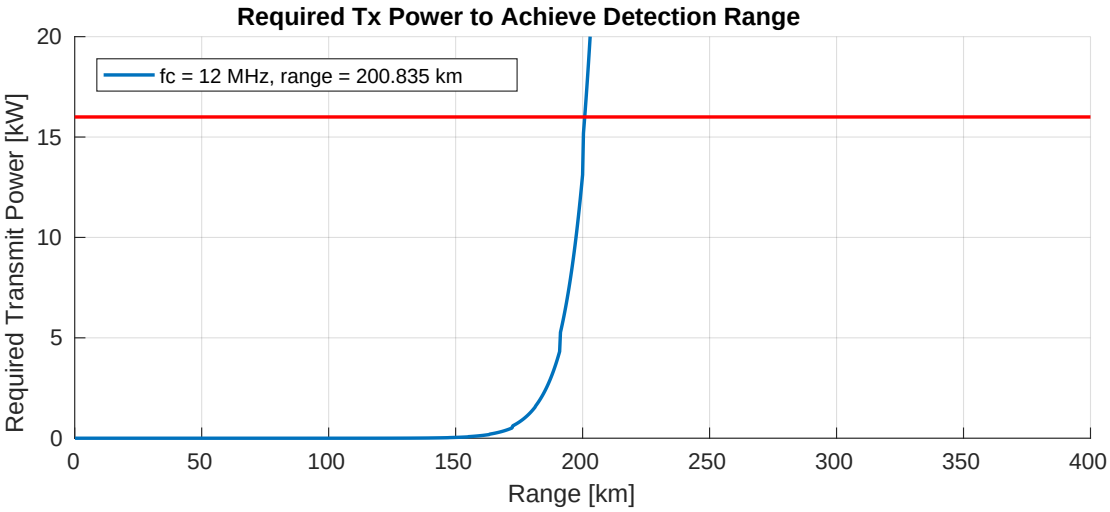

Figure 3.9: Transmit power required to detect a tuna longliner trawler over range at 20 MHz. The horizontal red line intersects at 16 kW. Trawler is of length 23.8 m and has a displacement of 90 tonnes.

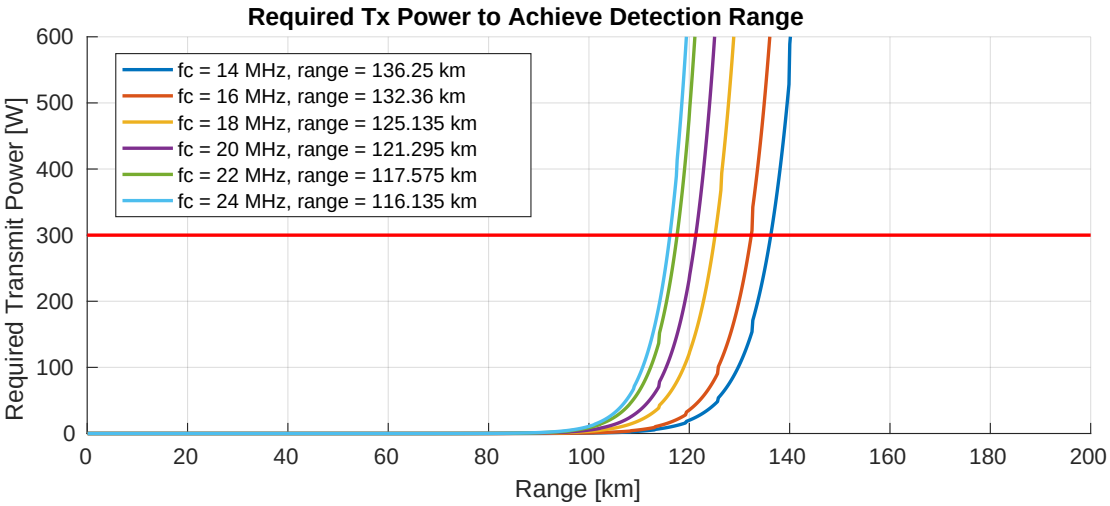

Figure 3.10: Transmit power required to detect the USNS Salvor over range and frequency. The horizontal red line intersects at 300 W.

Chapter 4

HFSWR Demonstrator

The design aim for the radar system is to have a single node designed that by itself may act as a complete monostatic radar [61]. This node can consist of (but not necessarily include) a complete RF transmit chain and two RF receive chains and must contain digital samplers and synthesizers for each RF chain. A design overview of one of these monostatic nodes is illustrated in Figure 4.1 and the final design for a single monostatic node is illustrated in Figure 4.2. This monostatic node can be replicated multiple times and attached together to form a larger array of nodes as illustrated in Figure 4.3.

Each node consists of a Red Pitaya (RP) digital signal processing (DSP) platform (expanded on in Section 4.1) which will synthesize the transmit waveform, record

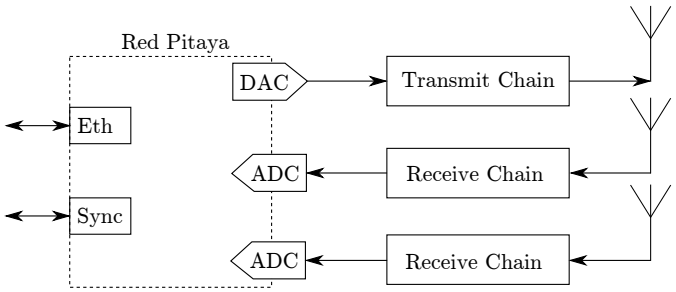

Figure 4.1: Architecture of a single node in Fig. 4.3. Each node may contain a maximum of two transmitters and two receivers.

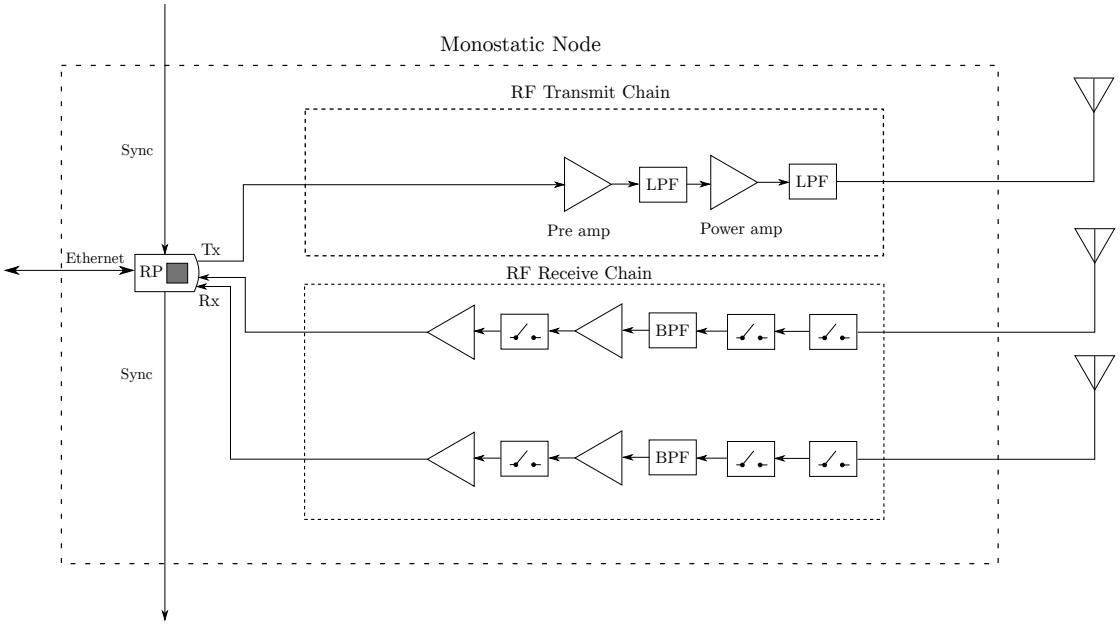

Figure 4.2: Complete design for a node. A single node must have a Red Pitaya and may consist of an RF transmit chain and two RF receive chains, depending on the purpose of that node. The Red Pitaya has an Ethernet port for control and two SATA ports for bus topology synchronisation.

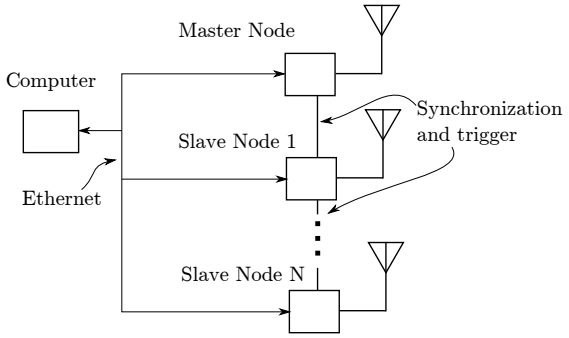

Figure 4.3: HF radar demonstrator simplified block diagram. Up to four antennas can be attached to each node.

on receive, synchronise with other Red Pitayas, and temporarily store the recording until retrieved by the operator. Each node may consist of a RF transmit chain and one or two RF receive chains, depending on the purpose of that particular node. The RF Frontend will be expanded on in Sections 4.2 and 4.3.

4.1 Digital Hardware

The Red Pitaya (RP) SDR platform (pictured in Figure 4.4) is used for synthesizing the radar waveform and sampling on receive along with controlling external hardware and synchronising with other RPs. SDR is advantageous for HFSWR systems which must operate on a non-allocated and non-interference basis. SDR has the potential to dynamically adjust the frequency of operation to avoid causing interference to other users [62].

Another advantage of using an SDR platform is the ease of control. Conventionally a radio frontend needs narrow bandpass filters operating in the frequency of interest and a mixer to transform the transmit signal to RF and the received signal to baseband. This can become expensive for a demonstrator system where the operator may wish to record data at different frequencies and bandwidths and would therefore need a variety of bandpass filters. With an SDR device such as the RP, digital bandpass filters can be synthesized on demand without any extra cost or difficulty. The transmit waveform can also be easily modified. All that is required from the frontend are anti-aliasing filters, low-noise amplifiers (LNA) to improve the sensitivity of the receiver and a power amplifier to increase the SNR.

A complete SDR radar was implemented on the RP by Barris [8] from which minor modifications were applied for this project.

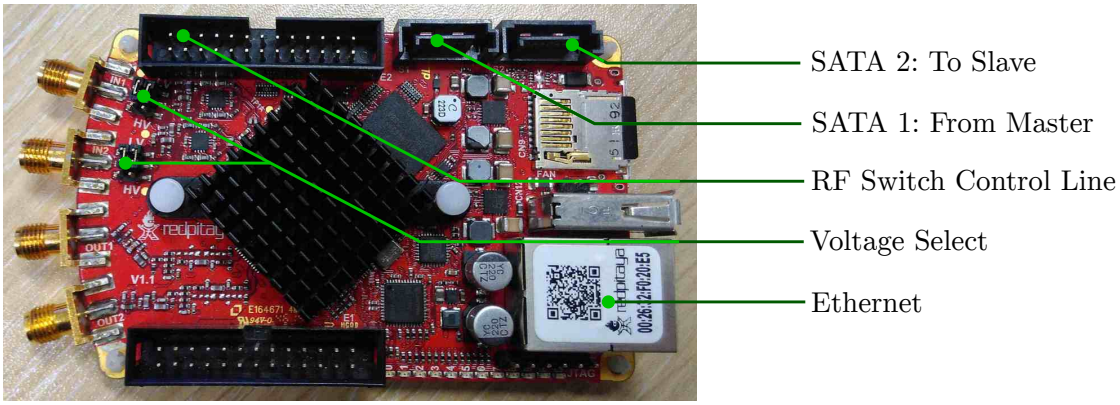

Figure 4.4: Picture of the Red Pitaya (RP) with ports relevant to this project labelled.

4.1.1 Red Pitaya Hardware and Limitations

The RP is a credit card sized development board that houses an Xilinx Zynq 7010 and costs about ZAR 4,000 each. The Zynq range of FPGA's have the advantage of including both an ARM Cortex-A9 processor and FPGA logic fabric all on the same chip. The ARM processor is powerful enough to run a headless version of linux Operating System (OS) and support an Ethernet device, making communication with the RP possible via Secure Shell (SSH) or through a custom server-client application. The FPGA fabric allows for high speed digital signal processing (DSP) of the receive waveform (the necessity of this fact will be made clear) and for the accurate timing requirements of the radar system.

The RP also contains two ADCs and two DACs attached to the FPGA, each with 14 bit resolution and 125 Msps sampling rate. Each ADC results in a total influx of data of 250 MBps (after each 14 bit sample is stored in a 16 bit word) which means both ADCs results in a total data rate of 500 MBps. The Zynq 7 chip contains a simplex High Performance (HP) bus between the FPGA and the CPU capable of streaming data at 476 MBps which is less than the required 500 MBps. The CPU is also bottlenecked by the low 10 MBps write speed of the SD card.

The solution to this data rate limitation implemented by [8] is to use the 512 MB of random access memory (RAM) that is shared between the FPGA and the ARM

CPU by allocating 4 MB of RAM to the FPGA. The CPU constantly probes the 4 MB block RAM for new data and subsequently passes that data to either the SD card or a larger block of RAM. It was experimentally determined [8] that samples can only be effectively captured if the sampling rate is reduced by a factor of 5 (25 Msps for a single ADC or 100 MBps for both ADCs) and the samples transferred directly to RAM using direct memory access (DMA). Only once the experiment is over can the data be transferred from the high speed RAM to the low speed SD card. This means that the recording time is limited by the shared 512 MB of RAM. The OS requires a dynamic portion of RAM to function correctly leaving only 200 MB of RAM for both ADC channels. The result is that only 2 seconds of recordings can be captured coherently where several minutes of coherent data is required for HFSWR.

An integrator similar to that used by [63] was implemented at the end of the processing chain except that successive range lines were integrated together instead of power spectra. The sample resolution is also increased from 14 bit to 32 bit to prevent overflow from integration. The maximum number of range lines that can be integrated without overflow (assuming the largest possible number of 2^{14}-1 is integrated) is 262160 (close to 2^{18}). Coherent integration by this means affects velocity ambiguity because the sampling frequency across range lines scales down by the number of integrations. The Doppler frequency of a moving target is calculated using (2.3). The sampling frequency across slow time is the pulse repetition frequency which must be larger than double the Doppler frequency to obey Nyquist and measure velocity unambiguously:

$$PRF_{integrated} = 2f_{Dmax} = \frac{4v_{max}}{\lambda_c}, \tag{4.1}$$

where $PRF_{integrated}$ is the PRF after slow time integration and scales down with the number of integrations,

$$PRF_{integrated} = \frac{PRF}{N_{integrate}},$$

where $N_{integrate}$ is the number of range lines integrated. Maximum unambiguous

velocity is therefore

$$v_{max} = \frac{\lambda_c \cdot PRF}{4N_{integrate}}. \tag{4.2}$$

This ambiguity constraint is not an issue for HFSWR since λ_c is in the decameter range which is 2 to 3 orders of magnitude greater than that of microwave radar and the PRF is typically 500 Hz to 1 kHz which is less than a single order of magnitude lower than microwave radar. Potential targets for HF radar include gravity waves and large ocean vessels, both of which are reasonably low speeds. Faster targets such as intercontinental missiles and aeroplanes are affected by the velocity ambiguity limitation however these targets require a much lower CPI (to prevent range and Doppler smearing) and therefore $N_{integrate}$ can be reduced to detect these targets. A reasonable number of integrations is in the order of hundreds for measuring Bragg scatter and detecting ocean vessels.

4.1.2 Digital Implementation

A complete pulse radar implementation was completed by [8] including synchronising and timing considerations. The transmit waveform samples are generated by the ARM processor and passed to a buffer in the FPGA. This transmit waveform can be easily changed to any form limited by 30 μs and the bandwidth of the RF transmitter. The digital receive chain implemented in the FPGA is shown in Figure 4.5. The digital receiver contains a decimator that passes only every 5th sample, an integrator which integrates M number of range lines, and finally a RAM writer that stores the samples in RAM. A program running on the ARM processor constantly probes the RAM writer pointer and moves the data from the 4 MB buffer into another portion of RAM to prevent overflow. More thorough details of the implementation can be found in [8] except for the implementation of the integrator.

Standard pulsed radar timing requirements apply. The transmit pulse is transmitted every PRI seconds and has a pulse length of τ seconds. Another important timing consideration is synchronisation between multiple RP devices. As shown in Figure 4.3, the radar can be expanded by simply duplicating the nodes and connecting them together. For all the transmitters and receivers to work together

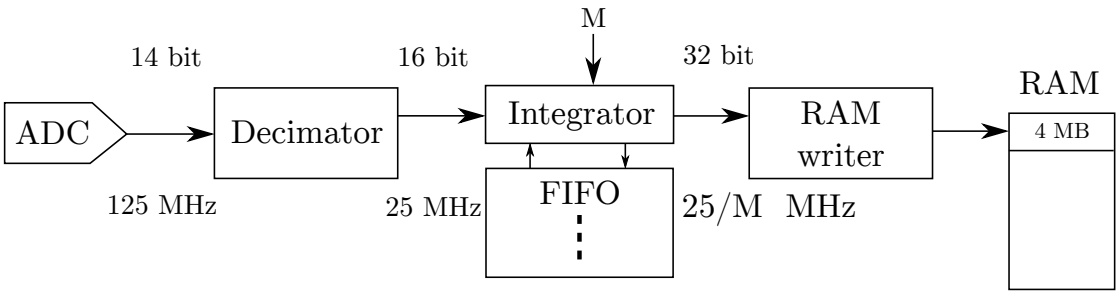

Figure 4.5: High level illustration of the digital receiver implemented on the FPGA. Numbers on top of the lines represent the sample resolution and numbers at the bottom represent the sample frequency in MHz.

coherently, it is vital that all RPs share the same 125 MHz clock. All the RPs must start the experiment at the exact same time to ensure that the RF switches are in the correct states at the correct times. Both of these issues are solved by daisy chaining multiple RPs using the two SATA ports in Figure 4.4 and configuring each individual RP to either be a master or a slave. In any setup, there must be one master and one master only. There may exist no slaves in a setup and there is no apparent upper limit to the number of slaves.

A SATA connector contains two differential pairs with the intention to communicate serial data at high speeds (6 Gbps) over short distances (0.5 m). Instead the SATA connectors are used to send a 125 MHz CLK signal and a RESET signal over the two differential pairs over a much further distance (excess of 10 m). This is illustrated in Figure 4.6 for N+1 RPs. The SATA cable is extended using Category 5 (Cat 5) cable. Both the SATA cable's differential pair and Cat 5 twisted pair have a characteristic impedance of 100 Ω. Transmission delays between each successive RP exists due to the cable length. The 125 MHz CLK signal is a continuous monochrome signal and the largest possible phase error between successive RPs is $2\pi\frac{25\text{MHz}}{125\text{MHz}} = 1.256$ radians. This error can be minimised by adjusting the cable length and using good quality transmission line to prevent phase variation. The RESET line indicates to the slave RP that the experiment has started and that the next slave must be notified. A propagation delay exists between each successive RP which means the master node will start before the next slave, which will start before the following slave and so on. This delay is solved by including a

delay timer in the FPGA where each node has a separately preprogrammed delay equal to the propagation delay from that node to the very last slave, including the master. As an example consisting of a master and two slave nodes: once the master has been triggered to start the experiment, the master will immediately start its delay timer and activate the RESET line. Once the first slave has been activated, it will immediately start its own internal delay timer and activate the next RESET line. Finally, once the second slave's RESET line has been activated, the second slave will start the experiment immediately since there is no more slaves in the chain. By this time the two delay timers in the master and the first slave will have reached zero and they both will start the experiment at the exact same time as the second slave.

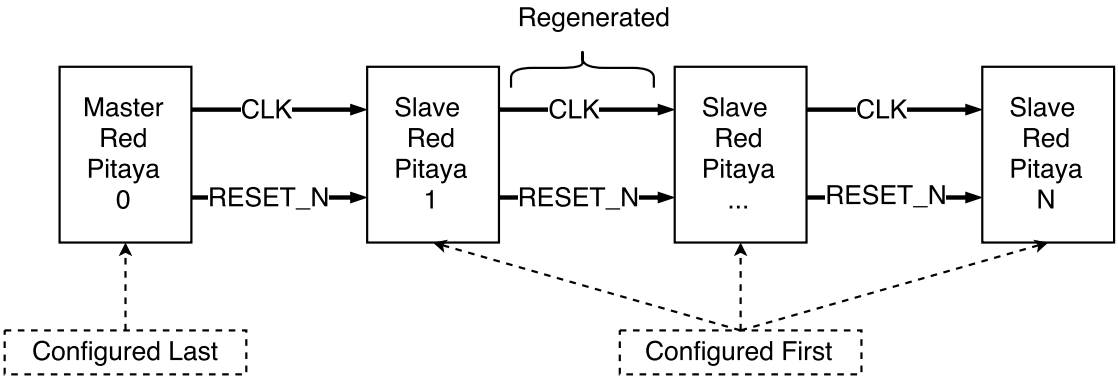

Figure 4.6: Example of N RPs attached together in a daisy chain bus topology containing 1 master and N slaves. Figure taken from [8].

4.2 RF Frontend: Transmit

The transmit chain exists to amplify the synthesized chirp from the Red Pitaya to an appropriate power level before radiating from the antenna. It is also important for the transmit chain to filter out any spurious signals and harmonics generated by the DAC and amplifiers to prevent interfering with other users of the RF spectrum.

The RF transmit chain of Figure 4.1 is expanded on in Figure 4.7 and consists of two low-pass filters, a preamplifier and a power amplifier. The preamplifier is used to amplify the 10 mW signal from the Red Pitaya to a more suitable power required by the power amplifier. The first low-pass filter removes harmonics

generated by the DAC and preamplifier. The power amplifier further increases the power to a selectable level up to 600 W. The low-pass filter after the power amplifier removes harmonics generated by the amplifiers and must be able to handle the transmit power. The output power level is controlled by attaching variable attenuators before the preamplifier. This section will characterise the subcomponents in Figure 4.7.

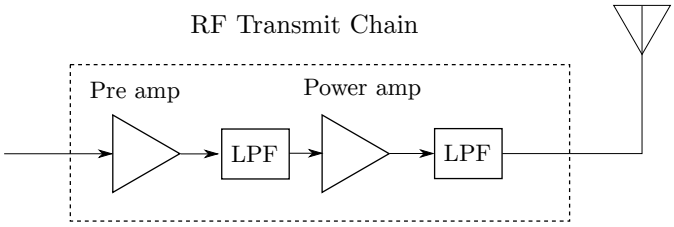

Figure 4.7: RF frontend Transmit Chain from Fig. 4.1.

4.2.1 PA10W Preamplifier

The preamplifier model PA10W shown in Figure 4.8 was purchased new on eBay from eb104.ru for USD 60 (ZAR 806.47 on the day of purchase). This amplifier is used to boost the RF power from the 10 mW provided by the Red Pitaya DAC to the 1 to 10 W required by the power amplifier. This amplifier is advertised to operate between 1.8 MHz and 160 MHz and maximum output power of 15 W continuous wave. It was designed to be used as a preamplifier for amateur radio amplifiers which often expect an input power of between 1 W and 10 W. The gain was not clearly indicated however, the supplier states that supplying 10 mW will result in an output power of 10 W which implies a gain of 30 dB.

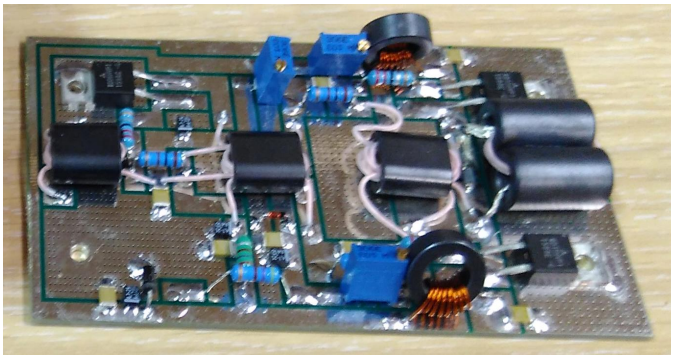

Figure 4.8: Picture of the preamplifier PA10W purchased from eb104.ru on eBay.

4.2.2 Pre-filter

The pre-filter appears between the preamplifier and the power amplifier and is used to remove harmonics caused by the preamplifier. This filter is pictured in Figure 4.9 and its circuit diagram is illustrated in Figure 4.10. The inductor in Figure 4.10 was not predetermined but was rather tuned by changing the number of turns of the inductor around a ferrite rod and changing the inductor's length.

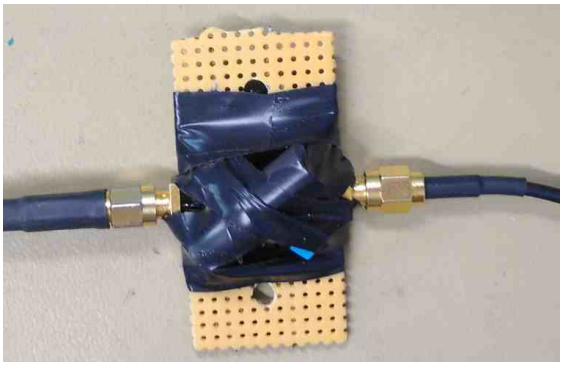

Figure 4.9: Picture of the pre-filter constructed on veroboard.

The magnitude and phase of the pre-filter is shown in Figure 4.11. The insertion loss varies by 3 dB within the pass band and is plotted in Figure 4.12. This filter should be replaced with a 6 element Bessel low-pass filter with a cutoff frequency of 25 MHz which can be easily achieved using the PCB and process discussed in Section 4.3.1

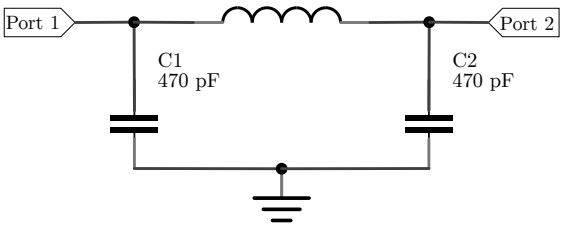

Figure 4.10: Filter circuit diagram.

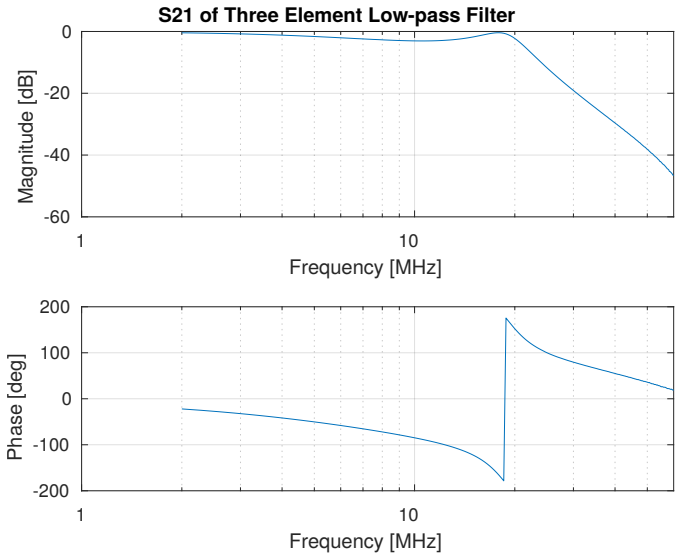

Figure 4.11: Measured S21 response of the pre-filter in Figure 4.9.

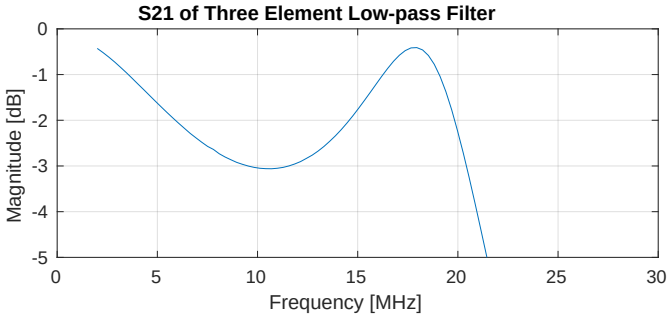

Figure 4.12: Measured S21 response of the pre-filter in Figure 4.9. The insertion loss varies by 3 dB.

4.2.3 PA600W Power Amplifier

The power amplifier model PA600W shown in Figure 4.13 was purchased new on eBay from eb104.ru for USD 260 (ZAR 3494.72 on the day of purchase) and is used to increase the transmit power. The purchased amplifier is rated maximum power of 600 W continuous wave and can operate between 1.8 MHz and 54 MHz. The gain is not specified by the supplier however it is advertised to transmit 600 W output power with an input power between 2 W and 3 W implying a gain between 23 and 24 dB.

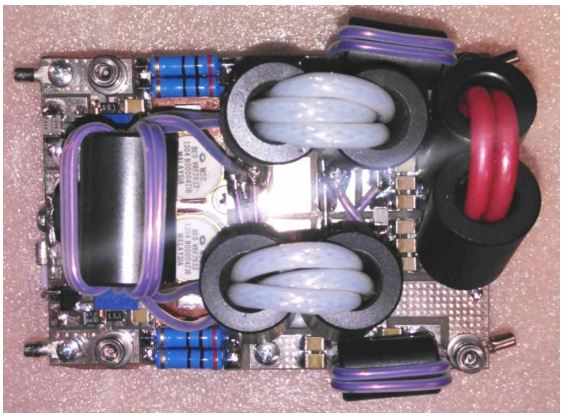

Figure 4.13: Picture of the power amplifier PA600W purchased on eBay from eb104.ru.

The complete RF transmit chain excluding the power low-pass filter was tested at 16 MHz to measure the total gain of the transmitter and to measure the 2nd and 3rd order harmonics. The results are plotted in Figure 4.14 and least squares (not plotted) is applied to the total power curve to calculate the y-intercept and therefore the gain. The total gain of the transmitter less the power filter is 57.38 dB. It is clear from the harmonics present in Figure 4.14 that an extra filter is needed after the power amplifier.

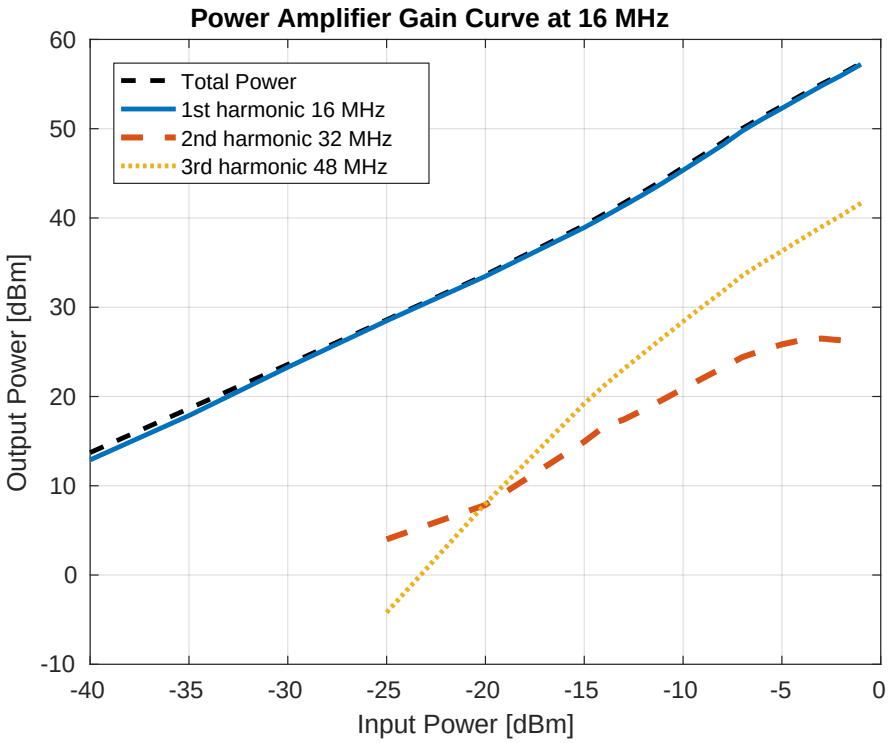

Figure 4.14: Gain curve of transmit chain including preamplifier, pre-filter, and power amplifier and not including power filter. The solid blue curve is the first harmonic which is the signal of interest and the orange dashed and yellow dotted lines are the second and third order harmonics respectively.

4.2.4 Power Low-pass Filter

As shown in Figure 4.14, the 600 W power amplifier generates high harmonics well before reaching its rated 600 W maximum output power. An 800 W filter was purchased new on eBay from eb104.ru for USD 180 (ZAR 2419.42 on the day of purchase) and is used to remove the harmonics generated by the power amplifier. This filter is pictured in Figure 4.15.

The 800 W low-pass filter can be switched between six different filters by switching the mechanical relays. Each of the six filters has the topology shown in Figure 4.16 with different component values. The six different filters each offer a different cutoff frequency as shown in Figure 4.17. The six different cutoff frequencies are 2.56 MHz, 5.35 MHz, 9.69 MHz, 18.56 MHz, 30 MHz, and 34 MHz. The operating

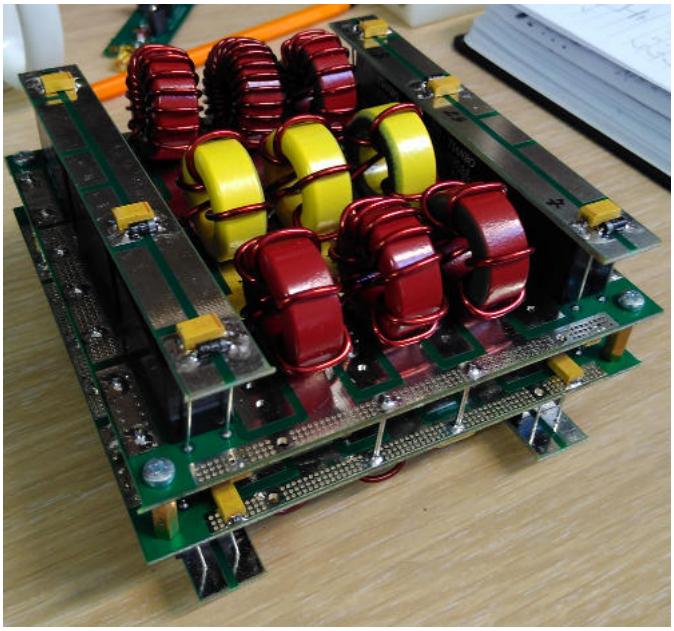

Figure 4.15: Picture of the power filter purchased on eBay.

frequencies used during the trials were 14 MHz, 16 MHz, 18 MHz, 20 MHz, 22 MHz, and 24 MHz and therefore the cutoff frequency of the 800 W amplifier was chosen to be 30 MHz for all the trials. It is also feasable to use a lower cutoff frequency of 18.56 MHz when operating below 18 MHz. The magnitude and phase response of the power filter with a cutoff frequency of 30 MHz is plotted in Figure 4.18.

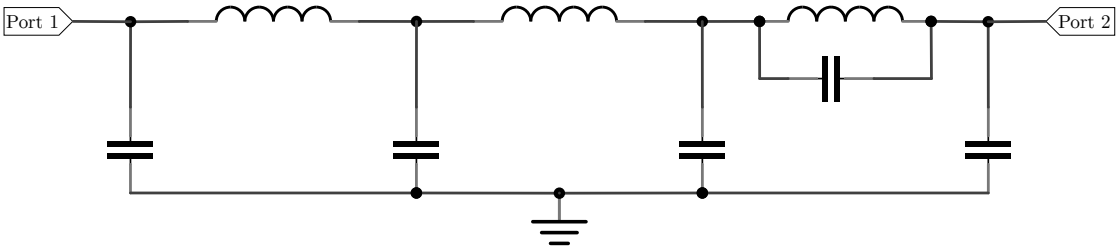

Figure 4.16: Circuit diagram of one of the six filters present on the power amplifier in Figure 4.15. All six filters have an identical topology.

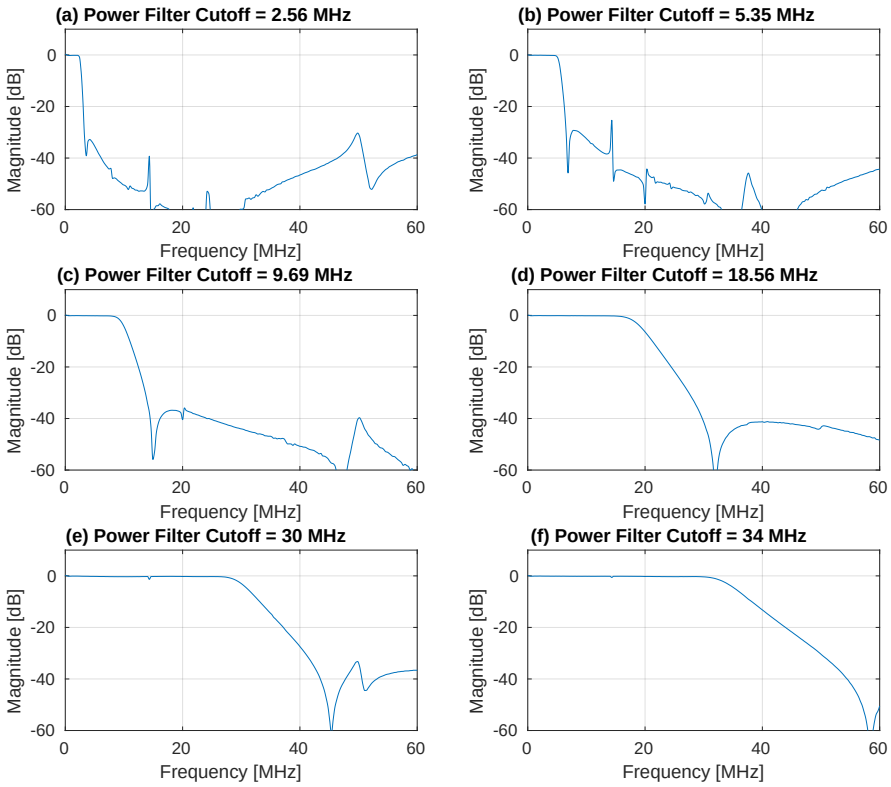

Figure 4.17: S21 magnitude plots of all six filters present on the power filter.

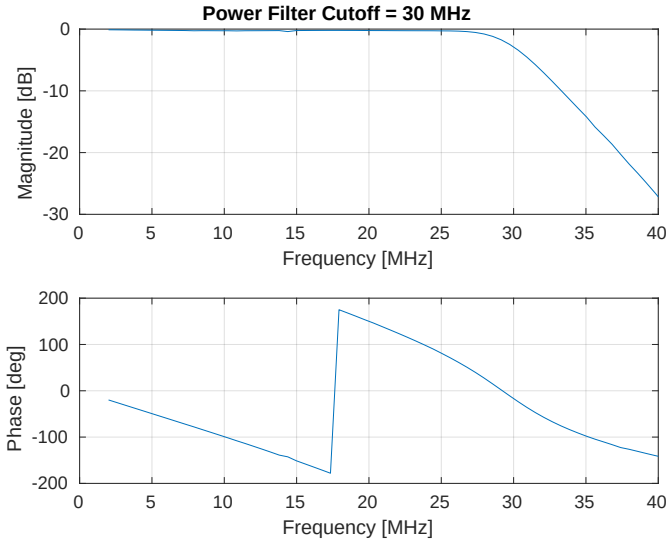

Figure 4.18: S21 magnitude and phase plots of the power filter switched to 30 MHz cutoff.

4.3 RF Frontend: Receive

The RF receive chain of Figure 4.1 is expanded as two different options in Figure 4.19. The band-pass filters exist to reduce external noise power, and to prevent unwanted aliasing while sampling at 25 MHz. The omnidirectional beam patterns of the transmit and receive antennas result in high feed through coupling. The RF switches help protect the sensitive receiver components by redirecting the high RF energy to a 50 Ω load while the radar is transmitting. The switch must have a switching frequency higher than the PRF (the UCT demonstrator has a PRF of 2 kHz) and short turn on and turn off times so that the ADC can record signals soon after the pulse has been transmitted. The RP input impedance is plotted in Figure 4.20 and is in the range of several kiloohm in the frequencies of interest. The RF inputs are matched to the receiver by inserting a 50 Ω load to each RF input using a BNC T-connector and 50 Ω BNC terminator.

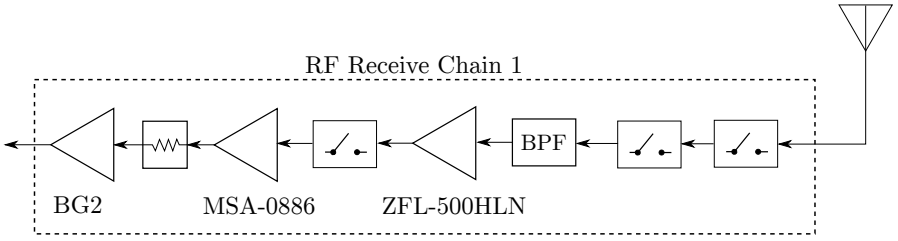

(a) First RF receive chain design. This design was used for the first two receivers during the trials. This receiver has a total calculated gain of 50.9 dB and equivalent thermal noise temperature of 1277 K.

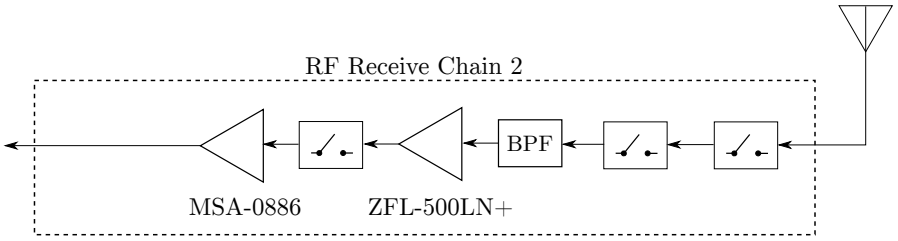

(b) Second RF receive chain design. This design was used for the remaining last four receivers during the trials. This receiver has a total calculated gain of 46.1 dB and equivalent thermal noise temperature of 971.6 K.

Figure 4.19: RF frontend receive chain from Figure 4.1.

Both the receive chains in Figures 4.19(a) and 4.19(b) were implemented. Ideally

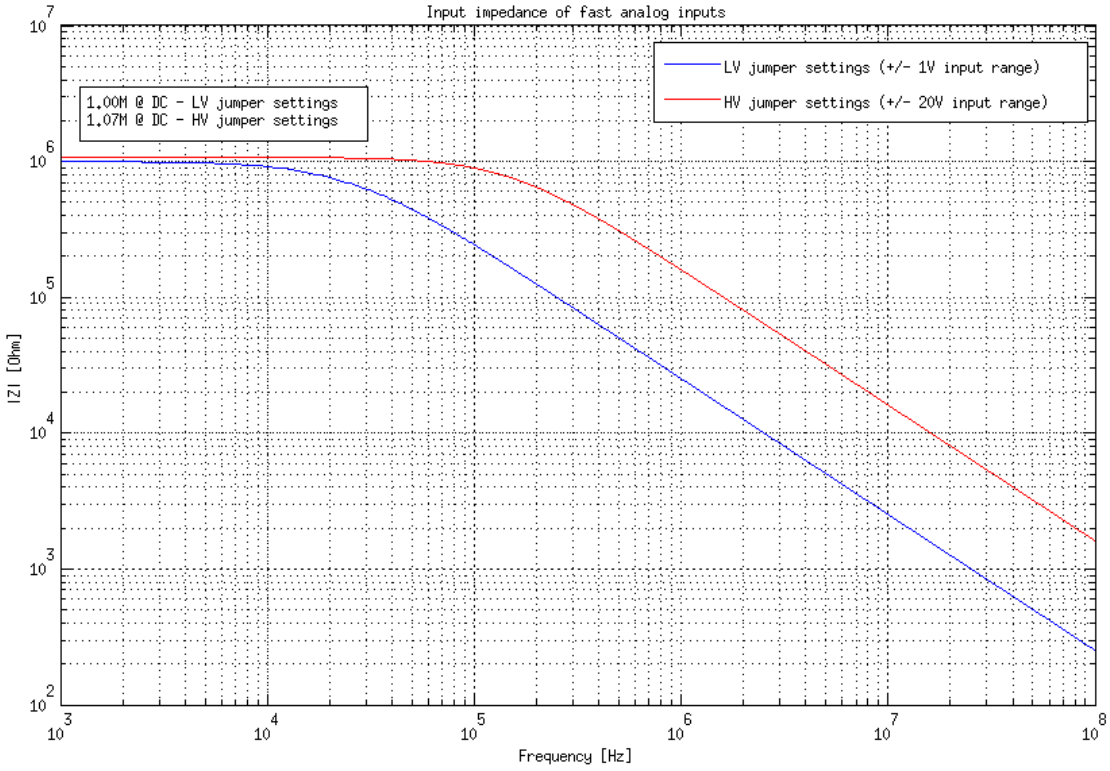

Figure 4.20: Input impedance of the RP's two RF ADCs. Taken from [64].

all receivers must be as identical as possible. A limited number of Mini Circuit amplifiers were available during the trials and the two chains in Figure 4.19 were chosen as a compromise.

The Mini Circuits LNAs available for the trials were four ZFL-500LN+ and two ZFL-500HN. All six of these Mini Circuits amplifiers were used for the first amplification stage of the six receivers in Figure 4.19. The second amplification stage for all six receivers is an MSA-0886 LNA purchased from www.banggood.com. The first two receivers included an additional 10 dB attenuator and a second Banggood (BG) LNA (referred to as BG2) to compensate for the lower gain of the ZFL-500HLN.

The remainder of this section will characterise the individual components used in the RF receive chains from Figure 4.19 and conclude with the characterisation of all six receivers used during the trials.

4.3.1 Filters

Passive lumped element filter techniques were used for the filters on receive. Other technologies such as cavity filters, waveguide filters and stub filters are impractical at HF frequencies due to their large size. Passive lumped element filters consist of capacitors and inductors attached in shunt or series. Two different PCBs were designed for use as a sixth order band-pass filter where each element consists of a capacitor and inductor. One PCB was designed to include through-hole capacitors and hand-wound inductors and another PCB was designed for surface mount components. The circuit diagram for this filter is shown in Figure 4.21. The PCB designed for through hole components is shown in Figure 4.22 and for SMD components in Figure 4.23.

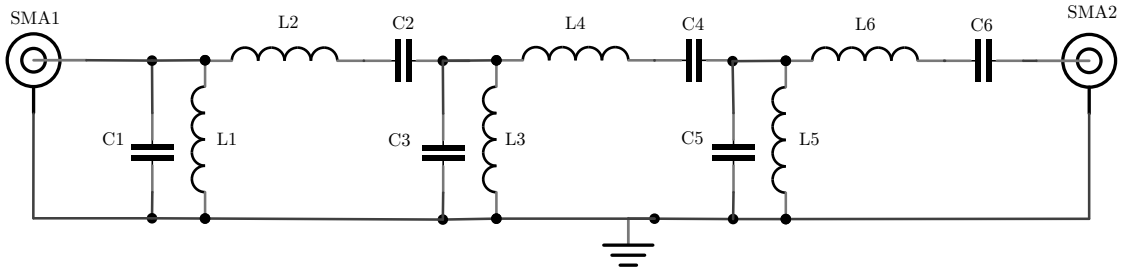

Figure 4.21: Circuit diagram of 6 element band-pass filter.

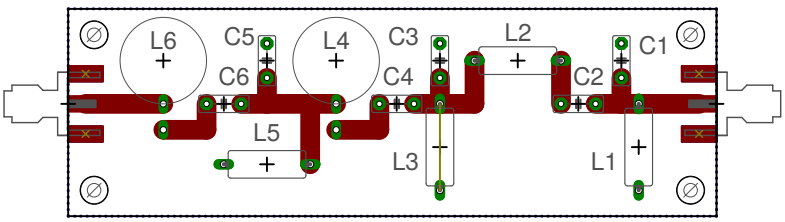

Figure 4.22: Sixth order band-pass filter PCB designed for through hole components based on circuit in Figure 4.21. PCB designed using Eagle Cad.

The band-pass filter PCB in Figures 4.22 and 4.23 can be configured as a band-pass, low-pass or high-pass filter by removing or shorting certain capacitors and inductors in Figure 4.21. The circuit diagram in Figure 4.21 can be used as is for a band-pass filter. To make a high-pass filter, the capacitors C1, C3, and C5 must be removed and inductors L2, L4 and L6 must be short circuited. To make a

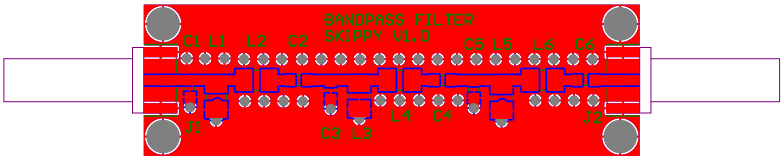

Figure 4.23: Sixth order band-pass filter PCB designed for SMD components based on circuit in Figure 4.21. PCB designed using Altium Designer.

low-pass filter, the capacitors C2, C4 and C6 must be short circuited and inductors L1, L3, and L5 must be removed.

The RF receive chains of Figure 4.19 consists of sixth order Bessel filters with a center frequency of 17.68 MHz and a bandwidth of 12.5 MHz (cutoff frequences 12.5 MHz and 25 MHz). A second filter added at the end of each receiver is recommended however was not implemented due to time and resource constraints. A Bessel filter design was chosen because of its maximally linear phase. Capacitor values are limited by the E12 standard capacitor values and inductors are limited by what is offered by Coilcraft. The component values calculated for the Bessel filter (ideal values) are tabulated along with the final values chosen in Table 4.1. The completed Bessel band-pass filter is pictured in Figure 4.24.

Table 4.1: Ideal and actual inductor and capacitor values for the 6 element 12.5 MHz to 25 MHz band-pass Bessel filter. Capacitor and inductor labels are for the circuit diagram in Figure 4.21

Capacitor	Ideal [pF]	Actual (E12) [pF]	Inductor	Ideal [nH]	Actual [nH]
C1	28	18	L1	2890	2700
C2	259	270	L2	313	307
C3	131	120	L3	617	538
C4	121	120	L4	669	538
C5	228	220	L5	355	380
C6	46.9	47	L6	1730	1800

The simulation of the actual component values and empirical results of the sixth order Bessel band-pass filter is shown in Figure 4.25. The empirical results agree with the simulation results with the deviation due to component errors. An insertion loss difference of 0.7 dB between the simulation results and empirical results is visible in Figure 4.26 and is a result of parasitic resistance and mismatch.

Figure 4.24: Picture of 6 Element band-pass filter with cutoff frequencies 12.5 MHz to 25 MHz.

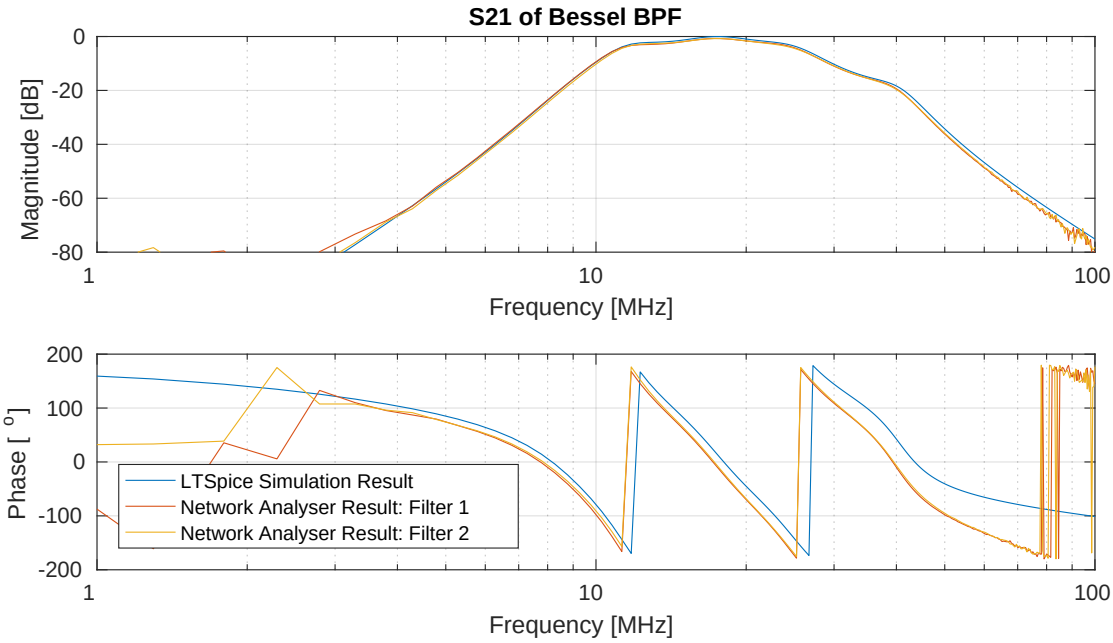

Figure 4.25: Empirical and simulated results of 6 Element Bessel band-pass filter built on SMD PCB. Both results are based on the actual filter components listed in Table 4.1.

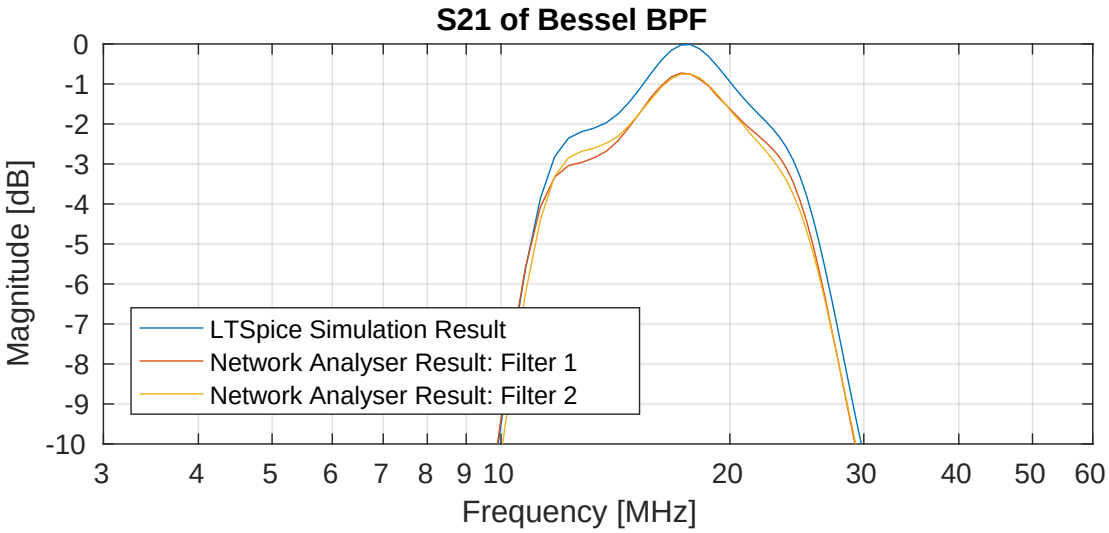

Figure 4.26: Close up of the magnitude plot in Figure 4.25. The difference in insertion loss between simulated and empirical results is approximately 0.7 dB.

4.3.2 RF Switch

The designed RF switch is shown in Figure 4.27 [65] which utilises the switching properties of a diode to redirect RF energy. The circuit uses cheap general purpose diodes (1N4148) which have sufficiently fast switching speeds at HF. Energy from V_{in} can be directed to either V_{out} or R_L by forward biasing the correct diode. From Figure 4.27, setting CTRL1 high will cause D1 to conduct resulting in an effective short circuit or an "on" state for D1. Setting CTRL1 low will cause D1 to be in reverse bias, resulting in an effective open circuit or "off" state for D1. The inductors were chosen to have a high impedance at RF to avoid drastically changing the output impedance and the series capacitor values were chosen to appear as a short circuit for the same reason. A picture of the completed RF switch is shown in Figure 4.28.

The designed circuit has been built and tested. Network analyser results are presented in Figure 4.29 and indicate that the switch has an insertion loss of 0.78 dB when turned on and 40 dB of suppression when turned off. The switch input was attached to a signal generator supplying a -5 dBm monochromatic signal at 16 MHz and an oscilloscope was attached to the RF output of the switch and the switch control waveform. These results are plotted in Figure 4.30 where the turn off and turn on times are measured by the red and green vertical lines respectively. Turn on time is 29.6 µs and turn off time is 8.7 µs.

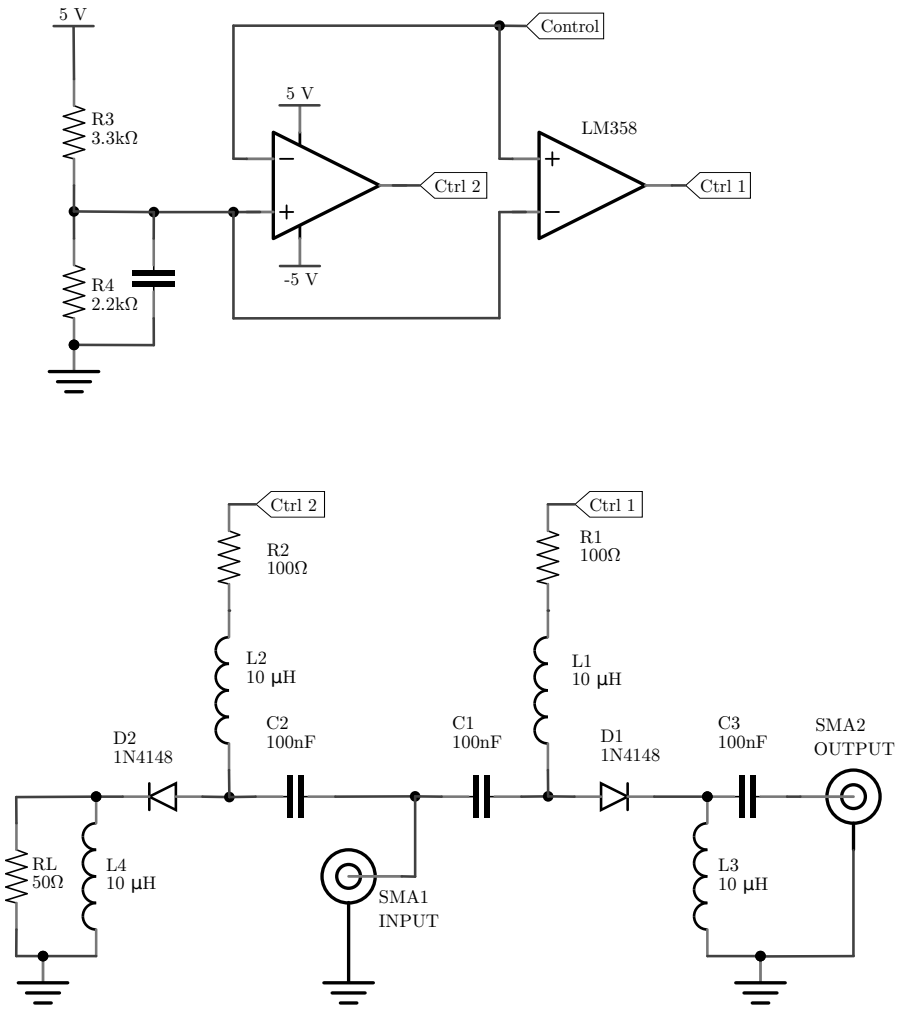

Figure 4.27: Circuit diagram of the RF switch. The opamp circuit at the top converts the single control line from the RP to two separate control lines in the RF switch.

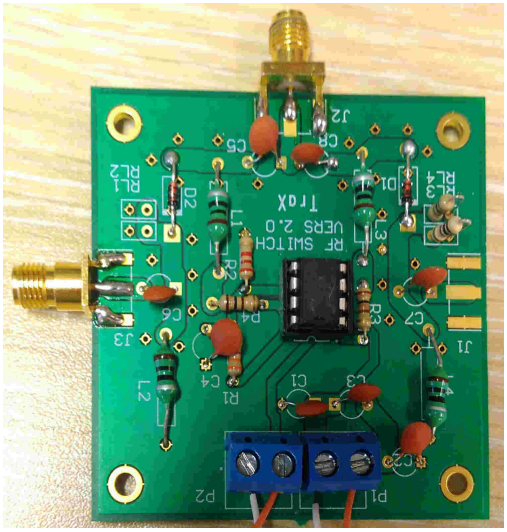

Figure 4.28: Picture of the RF switch. The top SMA port is the input and the outputs are on the left and right. The right SMA connector is detached and two 100 Ω resistors are attached in parallel instead.

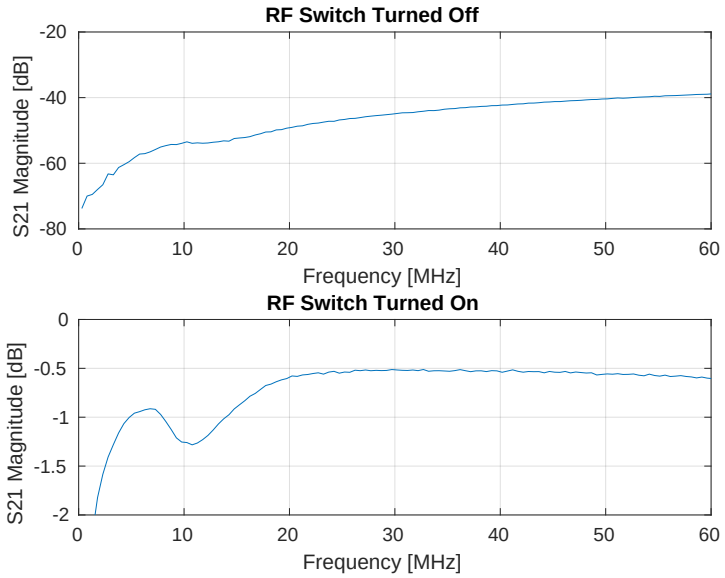

Figure 4.29: S21 of the switch when set to on and off states.

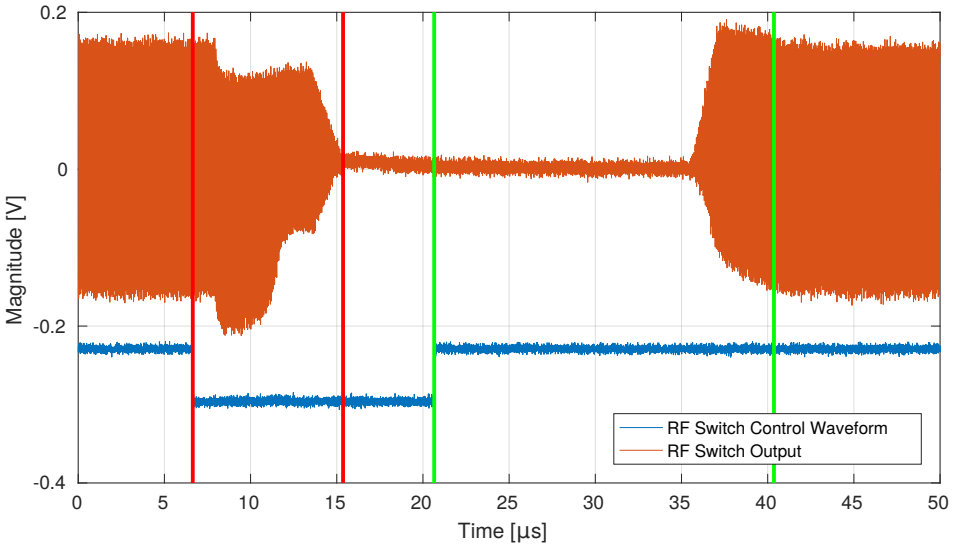

Figure 4.30: Time domain response of the RF switch. A -5 dBm monochromatic sinusoid at 16 MHz was attached to the input of the switch and the RF switch output is plotted in orange. The RF switch control waveform (blue) has been scaled down and shifted for illustration purposes. The red vertical lines represent the time length between turning the switch "off" and the RF output turning completely off. The green vertical lines represent the time length between turning the switch "on" and the RF output turning on. Off time is 8.7 µs and on time is 29.6 µs.

4.3.3 Mini Circuits ZFL-500HLN Low-Noise Amplifier

The first amplifier in the first two receive chains is the Mini Circuits ZFL-500HLN LNA pictured in Figure 4.31. This amplifier has a higher power handling capability than that of the ZFL-500LN+ and produces lower third order distortions, however it also has 5 dB less gain and the operating frequency starts at 10 MHz. The amplifier's characteristics are advertised as follows [66]:

- Frequency: 10 MHz to 500 MHz
- Noise Figure: 3.8 dB
- Gain: 19 dB
- 1dB compression: +16 dBm
- IIP3 point: +30 dBm
- DC power: 12-15 VDC

Figure 4.31: Picture of the ZFL-500HLN LNA. Taken from [66].

Two of the ZFL-500HLN low-noise amplifiers were readily available and no more were purchased. The unit price for the new model of these amplifiers (ZFL-500HLN+) excluding tax and shipping is USD 105.95.

4.3.4 Mini Circuits ZFL-500LN+ Low-Noise Amplifier

The first amplifier in the remaining four receive chains is the Mini Circuits ZFL-500LN+ LNA pictured in Figure 4.33. This amplifier has the lowest noise figure

of all the amplifiers offered by Mini Circuits that operate in the HF band. The amplifier's characteristics are advertised as follows [67]:

- Frequency: 0.1 MHz to 500 MHz
- Noise Figure: 2.9 dB
- Gain: 24 dB
- 1dB compression: +5 dBm
- IIP3 point: +14 dBm
- DC power: 12-15 VDC

The gain of the ZFL-500LN+ varies with supply voltage, as is evident in Figure 4.32. The amplifier is supplied with 12 V in the frontend resulting in a gain of 24 dB.

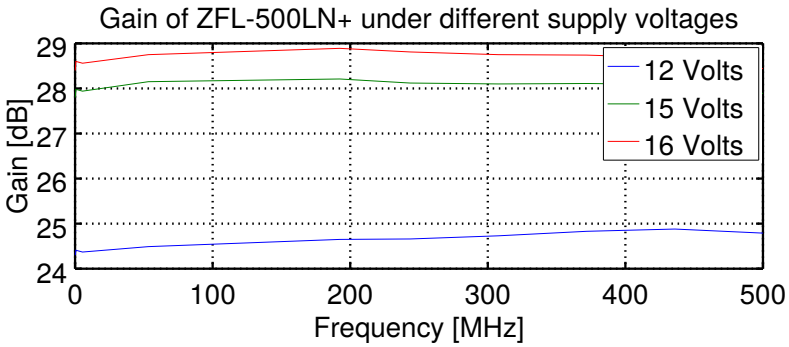

Figure 4.32: Gain of ZFL-500LN+ under different supply voltages. Taken from [67].

Four of the ZFL-500LN+ low-noise amplifiers were readily available and no more were purchased. The unit price of the ZFL-500LN+ is USD 87.95 excluding tax and shipping.

Figure 4.33: Picture of the ZFL-500LN+ LNA.

4.3.5 MSA-0886 Low-Noise Amplifier

The second amplifier in all the receive chains is the MSA-0886 LNA pictured in Figuire 4.34 which is advertised to operate between 1 MHz and 2000 MHz with a gain of 30 dB and a noise figure of 2 dB at 500 MHz. This amplifier was purchased from www.banggood.com and was not provided with a name. The amplifier is referred to as the MSA-0886 since this is the active component (transistor) on the circuit providing amplification.

The MSA-0886 amplifiers were purchased for ZAR 140.68 each from a website that does not specialise in RF electronics. The amplifier parameters were therefore determined experimentally. These parameters include the amplifier gain, 1dB compression, and IP3 point. The noise figure is assumed to be 5 dB which is 2 dB greater than what is advertised and it is shown in Section 4.3.7 that even a pessimistic noise figure is negligible compared to the externally captured noise power. The gain of the MSA-0886 is shown in Figure 4.35 and is equal to 26.6 dB at 16 MHz. The IIP3 point was derived by applying two tones into the amplifier at 16 MHz and 17 MHz and measuring the combined power of the fundamental tones and the third order tones adjacent to the fundamental tones. The results are plotten in Figure 4.36 where the IP3 point is crossed with two red lines. The IIP3 is 3.5 dBm and the OIP3 is 27.305 dBm. The 1dB compression point is determined by applying a single tone at 18.75 MHz to the input of the amplifier and increasing the power until the compression point is reached. The results of the 1dB compression point is shown in Figure 4.37 and is equal to +11.62 dBm. Parameters for the MSA-0886 are:

- Frequency: 1 MHz to 2000 MHz (advertised)
- Noise Figure: 2 dB at 500 MHz (advertised)
- Gain: 26.6 dB (Figure 4.35)
- 1dB compression: +11.62 dBm (Figure 4.37)
- IIP3 point: +3.5 dBm (Figure 4.36)
- DC power required: 12 VDC (advertised)

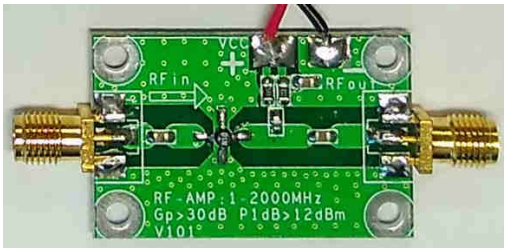

Figure 4.34: Picture of the MSA-0886 LNA from Bangood.

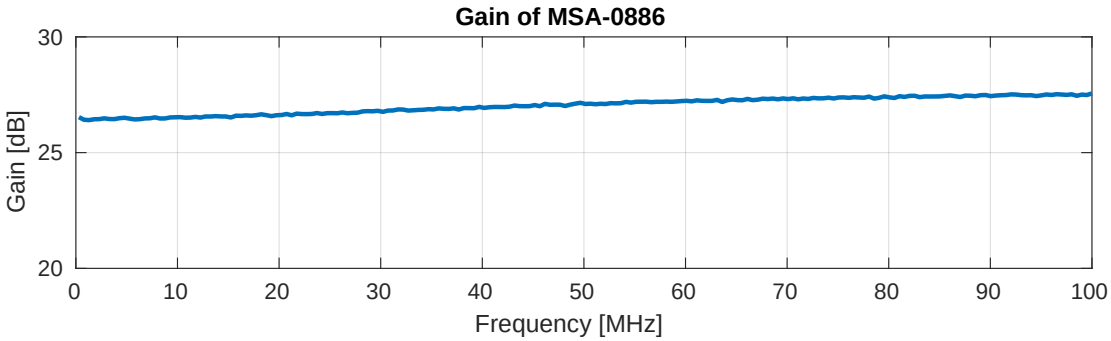

Figure 4.35: Gain of the amplifier plotted over frequency.

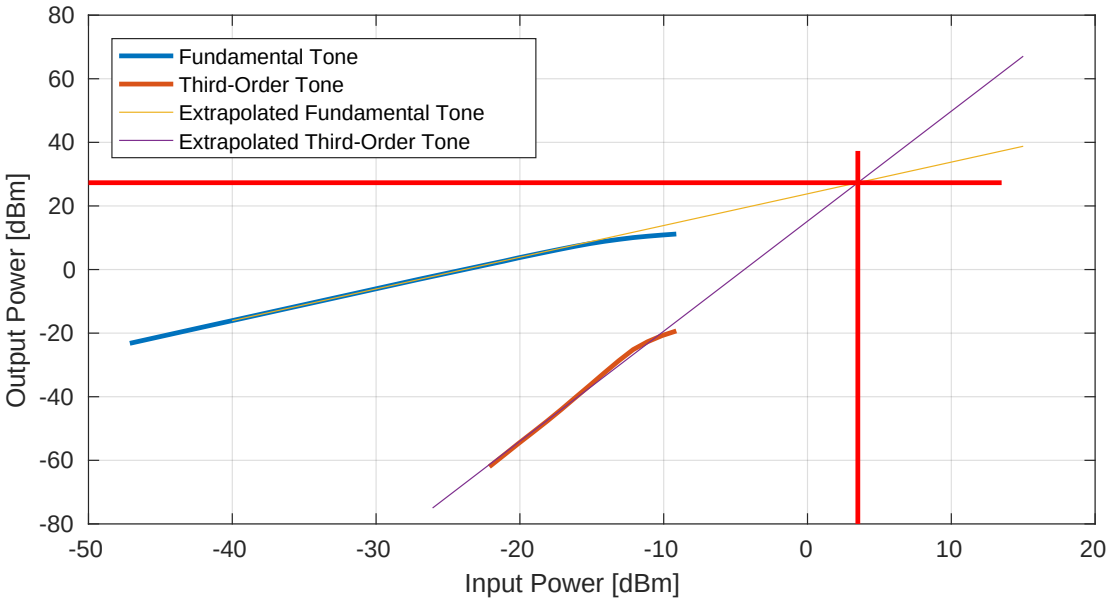

Figure 4.36: IP3 characterisation curve for the MSA-0886 low-noise amplifier. The IIP3 intersection is at 3.5 dBm.

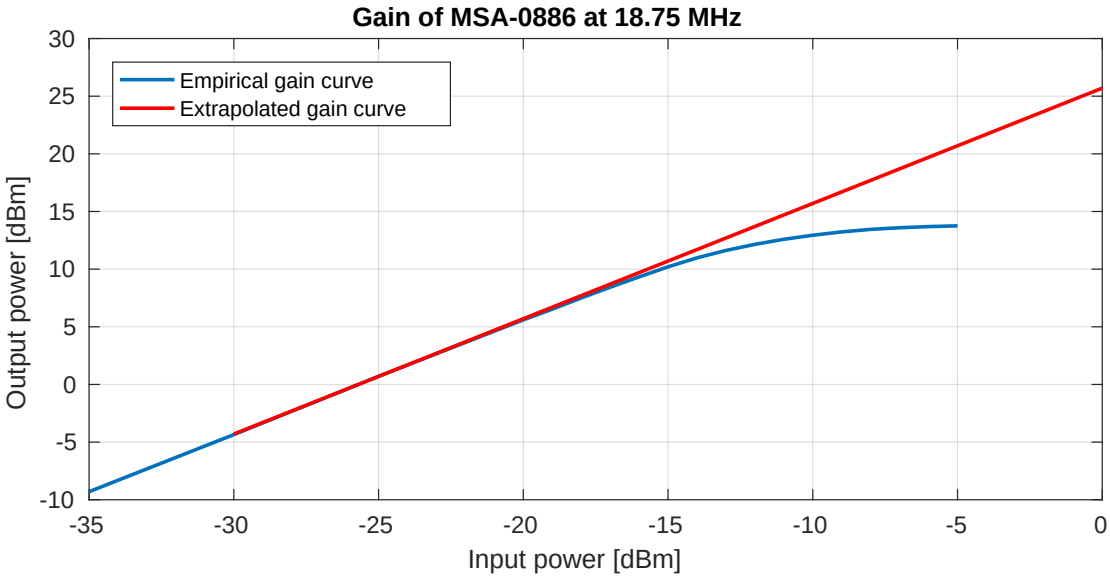

Figure 4.37: Empirical and expected output power versus input power.

4.3.6 BG2 Low-Noise Amplifier

The first two receivers (Figure 4.19(a)) require extra gain to compensate for the 5 dB less gain of the ZFL-500HLN compared to the ZFL-500LN+. This was achieved using the BG2 as the third amplifier in the chain of the first two receivers. The BG2 is pictured in Figure 4.38 and was named as such because it was the second amplifier purchased from www.banggood.com. The BG2 is advertised with an operating frequency of 5 MHz to 6000 MHz, a gain of 20 dB, a 1dB compression point of +21 dBm, and cost ZAR 120.60 each.

The same procedure used to characterise the MSA-0886 was applied to the BG2 and the results are plotted in Figures 4.39, 4.40, and 4.41. The gain is 15.75 dB at 16 MHz, the 1dB compression point is +16.15 dBm at 18.75 MHz and the IIP3 is +10.2 dBm.

- Frequency: 1 MHz to 6000 MHz (advertised)
- Noise Figure: not advertised
- Gain: 15.75 dB at 16 MHz (Figure 4.39)
- 1dB compression: +16.15 dBm (Figure 4.41)
- IIP3 point: +10.2 dBm (Figure 4.40)
- DC power required: 5 VDC (advertised)

Figure 4.38: Picture of the BG2 LNA from Bangood.

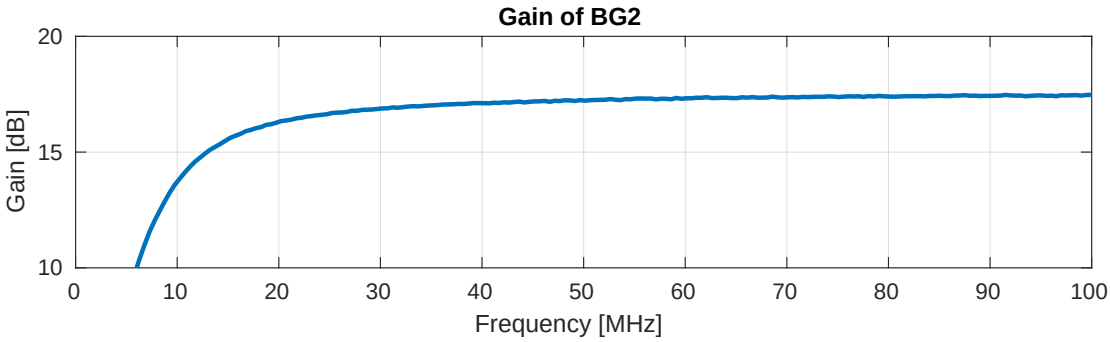

Figure 4.39: Gain of the BG2 amplifier plotted over frequency.

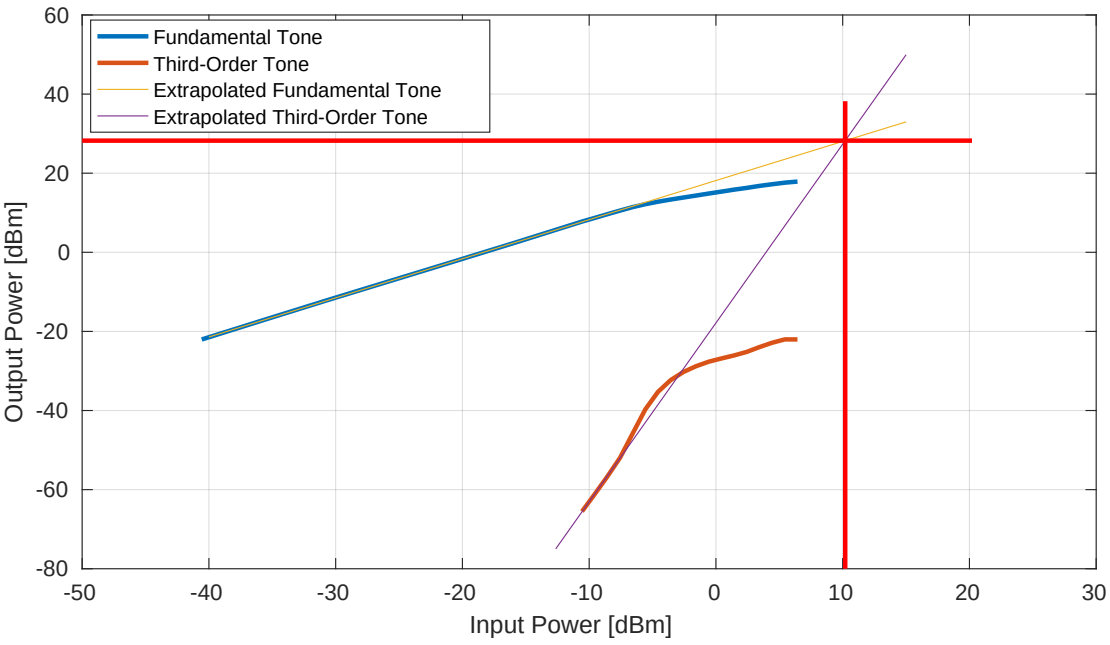

Figure 4.40: IP3 characterisation curve for the BG2 low-noise amplifier. The IIP3 intersection is at 10.2 dBm.

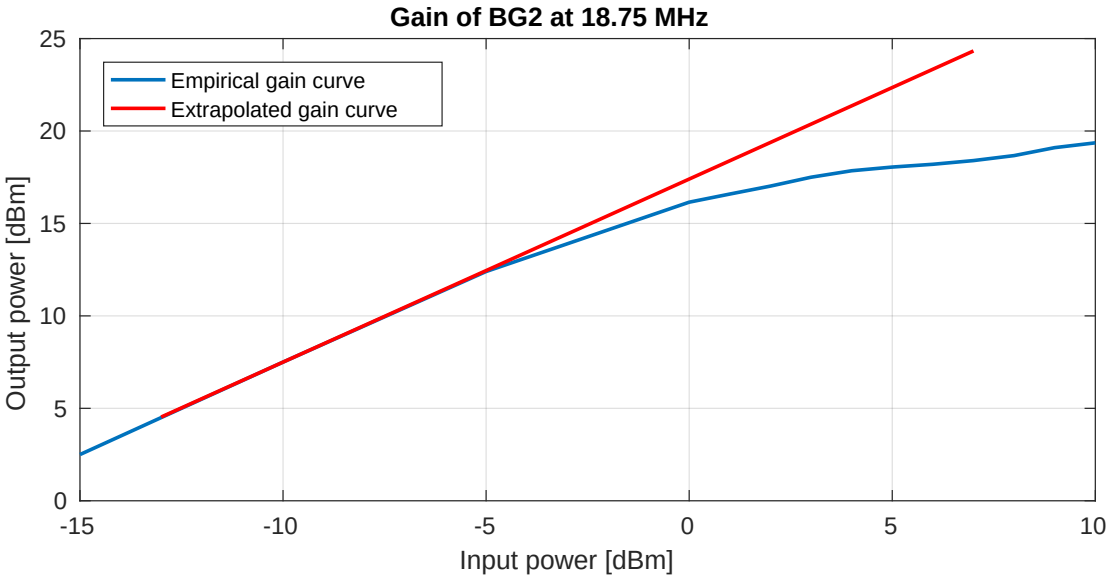

Figure 4.41: Empirical and expected output power versus input power of the BG2.

4.3.7 Receiver Considerations and Calculations

The aim of the RF receiver design is to improve the signal to noise ratio by utilizing the full dynamic range of the ADC of 10 dBm (2 Vpp) and in the process, adding as little thermal noise as possible. This can be achieved by using amplifiers with low noise figures and minimising any lossy RF components. As will become clear in this section, the noise figure of the receiver is negligible compared to the externally captured noise.

A receiver containing several devices with different gains and noise figures (NF) can be represented by a total equivalent gain G_e and by an equivalent noise temperature T_e referred to the input of the receiver. T_e is the temperature that a matched load attached to the input of the receiver would need to be to generate the same amount of noise as the entire receiver generates. The NF for lossy passive components is assumed to be equal to the components loss in dB which in the linear scale is the noise factor (F). For amplifier modules, datasheets often provide the internally induced noise as a NF in dB. The noise factor is related to the equivalent noise temperature by

$$F = 1 + \frac{T_e}{T_0}, \tag{4.3}$$

where T_0 is 290 K. The equivalent noise temperature of that component is therefore

$$T_k = 290(10^{NF_k/10} - 1). \tag{4.4}$$

The total gain of the receiver example in Figure 4.42 is

$$G_e = G_1 G_2 G_3,$$

and the total equivalent noise temperature of the receiver example in Figure 4.42 is

$$T_e = T_1 + \frac{T_2}{G_1} + \frac{T_3}{G_1 G_2}.$$

The equivalent noise power going into the receiver is the product of the equivalent

noise temperature with Boltzmann's constant and the noise bandwidth:

$$P_e = BT_e k. \tag{4.5}$$

This noise power does not exist at the input of the receiver but is a theoretical equivalent power at the input that would result in the actual noise power seen at the output of the receiver. This theoretical input power is a useful comparison with the external noise power captured by the antenna at the beginning of the RF chain. Predicted external noise temperature at the beginning of the receiver can be read directly off the right hand y-axis of Figure 3.2 or it can be calculated using (3.15) noting that the external noise power $P_n = BT_nK$ and $T_n = 290 \times 10^{F_a/10}$.

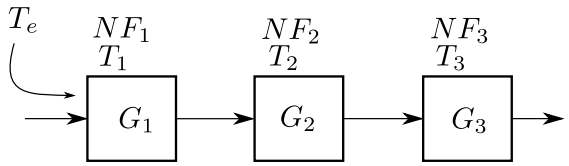

Figure 4.42: Example RF chain of three devices each with different gains and noise figures.

The receivers in Figure 4.19 both have an antenna attached to the receiver input and receiver output attached to a Red Pitaya input channel which has a built in 60 MHz anti-aliasing low-pass filter. The Bessel band-pass filter is attached before the LNAs and therefore limits the external noise between 12.5 MHz and 25 MHz. The internal anti-aliasing filter in the Red Pitaya limits the thermal noise bandwidth of the receiver to 60 MHz.

The external noise temperature at the beginning of the receiver will be the same for both receivers in Figure 4.19 and is approximated by selecting the noise temperature of the upper cutoff frequency (25 MHz) in Figure 3.2. The upper cutoff frequency of 25 MHz provides an optimistic figure for external noise temperature which is compared with the noise temperature of the receiver. The external noise temperature is $T_n \approx 2.9 \times 10^6$ K.

The receiver noise temperature is calculated assuming that the cheaper amplifiers purchased from BG (MSA-0886 and BG2 LNAs) have a noise figure of 5 dB. The actual NF of the amplifiers is irrelevant as will become clear. Noise power

due to receiver thermal noise is calculated using (4.5), taking the receiver gain into account, and setting $B = 60$ MHz. The receiver in Figure 4.19(a) has an equivalent thermal noise temperature of $T_{e1} = 1277$ K and total gain of 50.9 dB. Calculated thermal noise power available at the output of the first receiver (Figure 4.19(a)) is -38.8 dBm. The receiver in Figure 4.19(b) has an equivalent thermal noise temperature of $T_{e2} = 971.6$ K and total gain of 46.1 dB. Calculated thermal noise power seen at the second receiver's output (Figure 4.19(b)) is -44.8 dBm. The predicted external noise power observed at the beginning of the receivers is -63 dBm. The predicted external noise power observed at the end of the receivers is -12.1 dBm for the first receiver design and -16.9 dBm for the second receiver design. Noise power due to receiver thermal noise is three orders of magnitude less than the noise power due to external noise and is therefore reasonable to assume that receiver thermal noise is negligible.

4.3.8 Assembled Receivers

An assembled receiver node is present in Figure 4.43 where Figure 4.43(a) shows two receivers inside a single node and Figure 4.43(b) shows two of these receiver nodes synchronised together with an extended SATA cable. It should be noted that echoes from targets are highly suppressed by external noise which explains the need for long integration times. The consequence of such negligible echo power is that only the external noise power needs to be considered when determining the RF receiver gain. Originally the receivers were designed to have a gain of approximately 70 dB (by adding an extra MSA-0886 amplifier) so that the external noise power at the end of the receiver will reach close to +10 dBm and therefore utilizing the full dynamic range of the ADC. In practice however, the external noise was greater than was suggested in [56]. This is likely due to the high bandwidth of the receiver that captured multiple HF amateur radio operators such as the peaks in Figure 3.4. External noise power over the bandwidth of interest is approximately -45 dBm and varies greatly with time of day and HF radio activity.

Another design consideration was the number of RF switches required per receiver and their positions in the receiver chain. The purpose of the RF switch is to protect

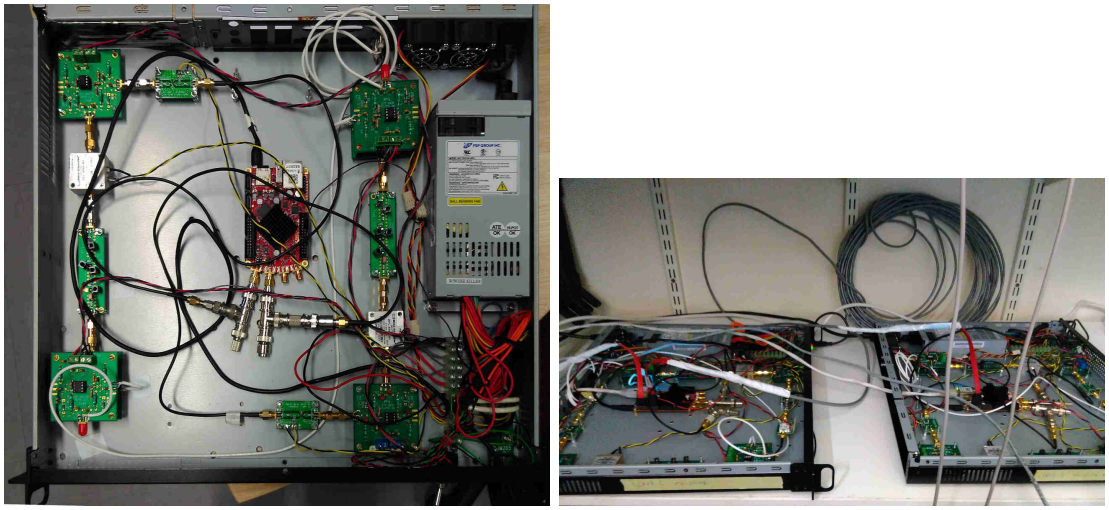

(a) Picture of a single receiver node containing two receivers.

(b) Picture of two receiver nodes synchronised using a SATA cable extended in length by Category 5 cable.

Figure 4.43: Receiver nodes.

the sensitive receivers while the transmitter is transmitting. The distance between the transmit and receive antennas during the trials were approximately 8 m apart which at 16 MHz results in a one-way FSPL of 14.6 dB at 16 MHz. FSPL assumes both antennas are in the far field which in this case they are not, and is therefore only used as an upper limit approximation. Taking antenna gains into account and assuming a transmit power of 600 W (57.8 dBm), the feed-through power captured by the receive antenna is 53.6 dBm which will damage the sensitive receiver. This power must be reduced to no more than -45 dBm to be comparable to external noise. A minimum of 98.6 dB of suppression is required. Each RF switch provides 40 dB of suppression and therefore three switches are required to provide 120 dB of suppression, well above the 98.6 dB required.

It was discovered during testing that the RF switches wouldn't provide the complete 40 dB of suppression when the input signal power was low, possibly due to the diode's themselves being non-linear components. With all three switches cascaded together, the first two switches would successfully attenuate the high power incoming signal however the third was less effective. Two of the RF switches is enough to attenuate the signal to a safe amount for the first LNA stage which was

either one of the two Mini Circuits amplifiers. A third switch is placed after the Mini Circuits amplifiers where it is more effective at suppressing the feed-through signal and therefore protecting the remainder of the receiver.

The magnitude and phase response of all six receivers after the trials were conducted are plotted in Figure 4.44. The red circles in Figure 4.44 indicate that channel one was not operating properly during the trials and it is therefore recommended to take care when processing channel one data. Channel one and channel two have a phase shift of 180° as a result of the inverting amplifier BG2 which has been taken into account in Figure 4.44.

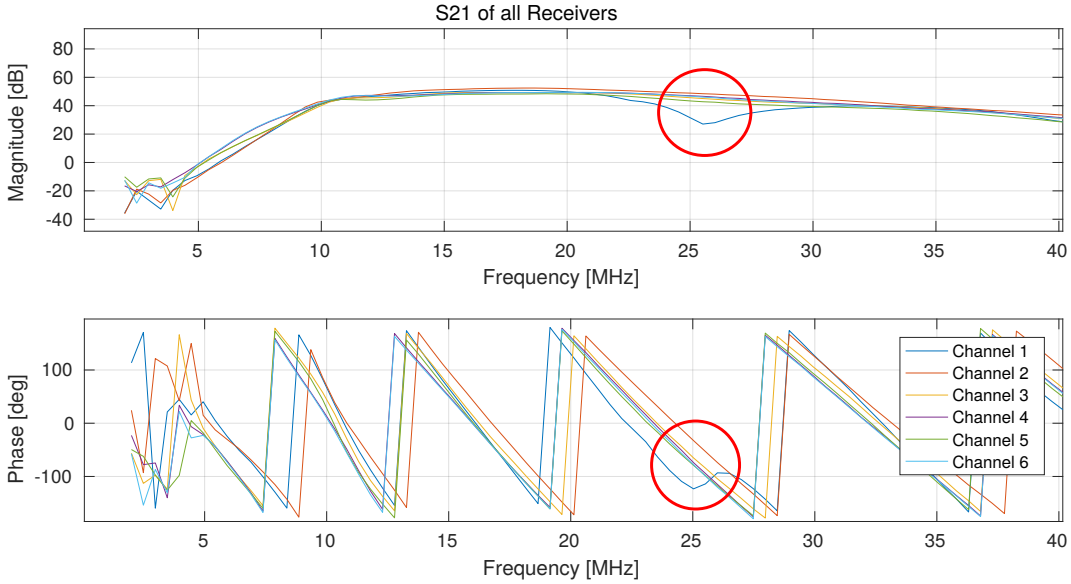

Figure 4.44: Magnitude and phase of all six receivers plotted over frequency. This was recorded after the trials were conducted. Channel 1 appears to be dysfunctional and it is recommended take care when processing channel one's data.

There is a significant phase error between all the channels as a result of component errors and cheap RF amplifiers. The phase errors can be corrected for post processing by multiplying each channel's IQ data with $e^{j2\pi\Delta\phi_{1n}}$ where $\Delta\phi_{1n}$ is the difference in phase response between channel n and channel 1 (taken from Figure 4.44) at the operating frequency.

4.4 Conical Transmit Antenna

The task of designing a broadband HF antenna was assigned to Patel [9]. The project description was to design an antenna suitable for an HFSWR demonstrator using phase interferometry. The antenna is limited to a monopole-type structure due to the large wavelength (10 m - 100 m) and a matching circuit is required for an electrically small antenna. This is well suited for a phase interferometry application where multiple antennas can be combined to form a larger antenna with more gain. A monopole design is also well suited for SW propagation which requires a near horizontal takeoff and vertical polarization. The operating frequency range of the antenna are those frequencies at which the antenna operates with appropriate reflection coefficient, gain and takeoff angle. These characteristics are [9],

- gain of at least 4.5 dBi
- reflection coefficient of less than -10 dB

These specifications were successfully achieved using a conical shaped antenna structure and with a matching circuit over the frequency range between 12.2 MHz and 23.8 MHz. Without a matching circuit, the antenna has a reflection coefficient below -5 dB over the frequency range between 13.6 MHz and 25.5 MHz. This antenna is well suited for transmit where it is important for the antenna to be well matched over the full bandwidth to make full use of the transmit power. On receive, many of these requirements can be relaxed due to the high external noise. Other aspects to consider include portability, compactness and weather resistance. Three more conical monopole antennas of a similar design have been constructed taking the recommendations from [9] into account.

4.4.1 Conical Antenna Simulation

The two designs considered in [9] were a monopole and a conical shaped monopole antenna. Conical antennas have a cone shape and is often modelled as a solid cone or cone sheet. In practice however the cone is approximated by vertical wires joined

by a center ring to give the cone shape. The conical antenna design is illustrated in Figure 4.45 and is often used because of its broadband characteristics, even without a matching circuit.

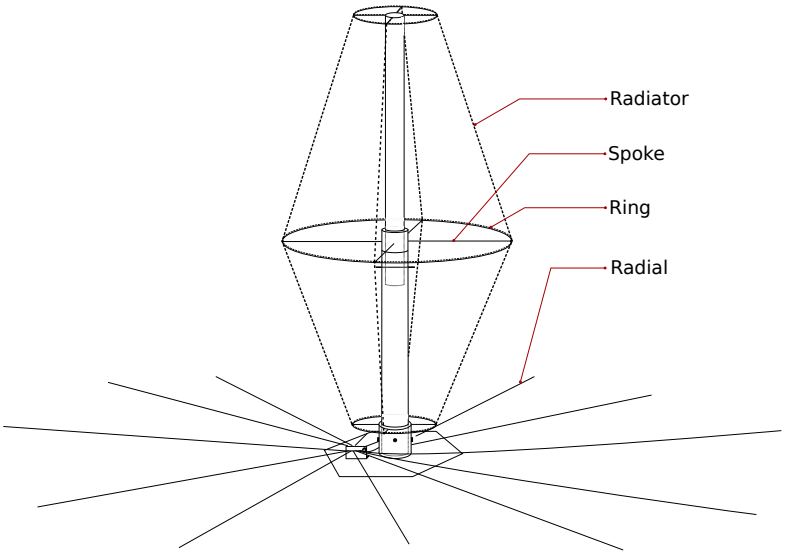

Figure 4.45: Drawing of the conical antenna design. Taken from [9].

Design considerations for the conical antenna include the height of the antenna, the number of radiators, and the diameter and height of the center ring. The design in [9] has four radiators, a center ring 1.6 m high and 1.5 m diameter, and the total height of the antenna is 3.45 m. Two smaller rings at the top and bottom of the antenna were also added, both with a diameter of 0.5 m with the bottom ring lifted 0.1 m from the ground.

The antenna is illustrated in Figure 4.45 and its reflection coefficient is plotted in Figure 4.46. The frequency shift between the simulated and empirical data is due to the spokes being thicker in the built antenna compared to the simulated antenna. The reduced bandwidth is due to the use of coaxial cable shield (tubular wire) as the conductors. Despite these deviations, the empirical reflection coefficient from Figure 4.46 has an appropriate bandwidth and reflection coefficient depth within the band of interest.

The beam pattern of the designed conical is similar to that of a monopole, and its associated gain is over 4.5 dB within its operating frequency. The gain decreases

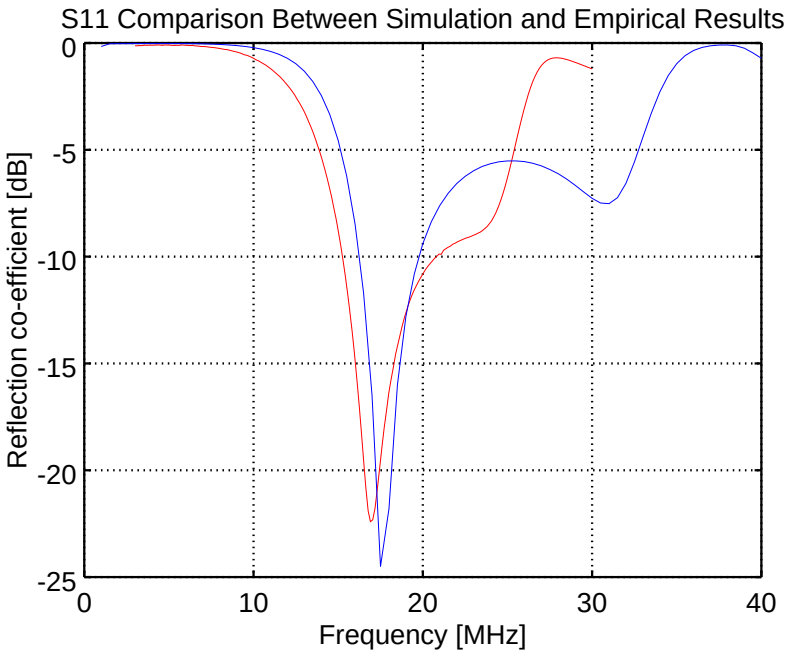

Figure 4.46: Reflection coefficient (S11) of the broadband conical antenna designed by [9] set up at a school field (red curve) plotted along with simulation results (blue curve).

as the frequency decreases.

4.4.2 Antenna Structure and Construction

The antenna structure was redesigned keeping the original shape of Figure 4.45 but with more portability and weather resistance. The core of the antenna consists of four parts (Figure 4.47): stand, bottom mast, top mast, and cap. The stand has the RF input, attachments for the ground plane, and spokes for the bottom ring. The bottom and top masts telescope vertically and give the antenna its height and structure. The cap at the top of the antenna holds the top ring and radiators.

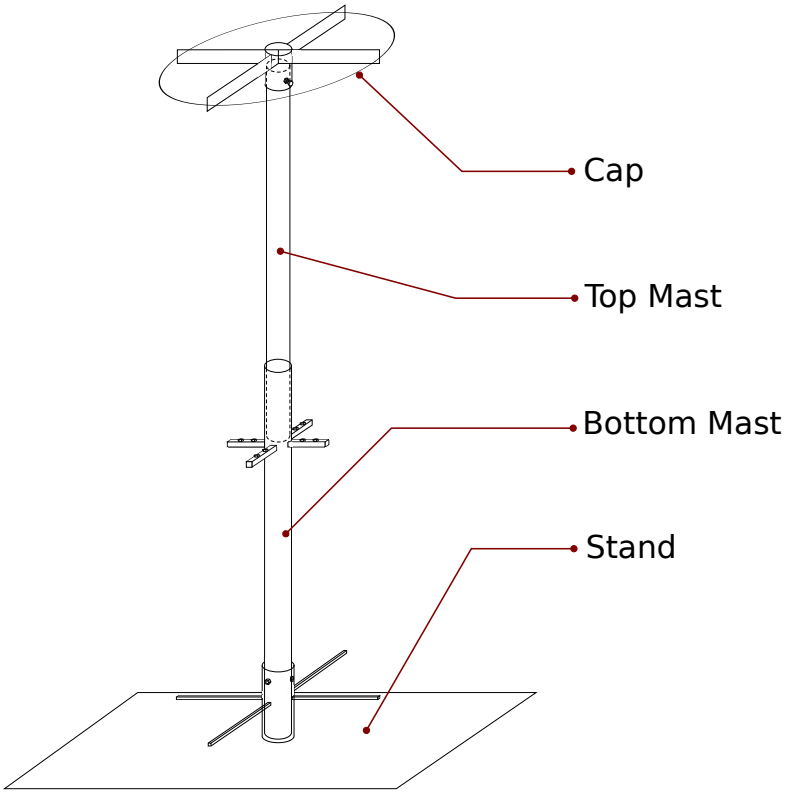

Figure 4.47: Illustration of the main supporting structure for the conical monopole antenna illustrated in Figure 4.45. The main supporting structure for this antenna consists of four parts.

A 1.5 m diameter ring is formed at the center by attaching 3 mm thick galvanised cable to the square rods using plastic end joints. This is illustrated in Figure 4.48. The mast is attached to ground at the stand and is therefore important that the radiating conductors are electrically isolated from the bottom and middle spokes.

It is also important that the conductors are electrically connected to all the rings according to the original design. The top ring is electrically connected to its radials which is electrically connected to the top mast.

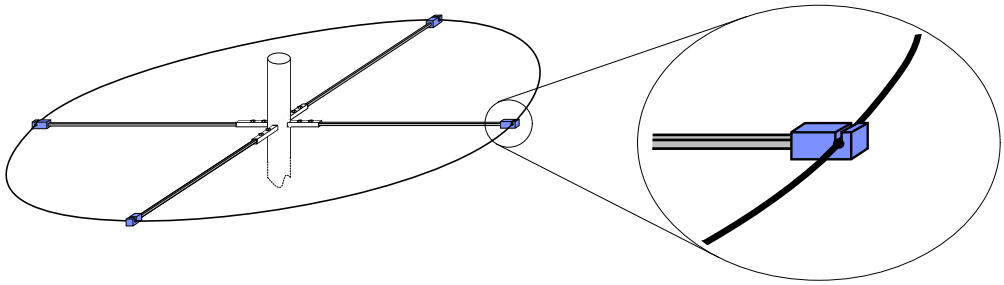

Figure 4.48: Illustration of the center ring, spokes, and lower mast. The spokes can be removed from the mast. Plastic end connectors ensure that the spokes are electrically isolated from the ring.

4.4.3 Fulfilling Recommendations

Recommendations were made by [9] to improve the design and durability of the antenna and to further clarify the simulation results. These recommendations include using more weather resistant materials for the antenna. The original antenna was built using mild steel which rusts easily, especially when placed near the ocean. The antennas used for this project were constructed mainly from galvanised steel and the exposed mild steel painted with NS4 to protect from rust.

4.5 Receive Antenna

The receive antenna is required to operate between 12.5 MHz and 25 MHz. The efficiency and reflection coefficient of the receive antenna may be relaxed due to the high external noise power in the HF band. The most important characteristic of the received signal is the signal to noise ratio and since the external noise is far greater than the receiver thermal noise, a low efficiency antenna not only attenuates the signal but also the noise and therefore the signal to noise ratio remains the same [1]. Ideally the antenna should have a null in its beam pattern pointing towards

the transmit antenna to improve isolation between transmit and receive, and a null pointing towards the ionosphere to prevent ionospheric bounce and galactic noise, whilst still having a beam pattern facing the surveillance area. The design must be easy to construct and setup. Three options include the conical, monopole and small loop antenna designs.

The conical antenna as described in section 4.4 is simple to set up and can operate over the full band of interest. On the contrary, its large size and components can require a set up time in excess of an hour, making it undesirable for portable configurations consisting of multiple antennas. The beam pattern of the conical design is omnidirectional and has a null pointing towards the ionosphere. This includes illumination towards the transmit antenna.

The small loop and monopole antennas are considered for the receive array due to their simplicity. They are both easy to construct, setup, and they are both compact antenna designs.

4.5.1 Small Loop Antenna

The small loop antenna (also known as magnetic loop antenna) [68, 69] is named as such since its circumference is typically less than a tenth of a wavelength, as opposed to a resonant loop antenna which has a circumference equal to a full wavelength.

The small loop antenna is known for its narrow bandwidth and two deep nulls pointing perpendicular to the loop core. Isolation between the transmit and receive antennas can be achieved with the small loop antenna by steering the null in the direction of the transmit antenna, which will most likely be perpendicular to the surveillance area where the beam pattern will be its strongest. The disadvantage of the small loop antenna is its high directivity towards the ionosphere which will result in greater cosmic and galactic radiation and will receive ionospheric clutter.

The small loop antenna is illustrated in Figure 4.49 and consists of a larger, capacitively tuned outer loop coupled to a smaller inner loop to which the transmission line is fed [69]. The circumference of the outer loop will have a perimeter less than

$\frac{3}{8}$ of a wavelength at the highest frequency of operation [69]. The circumference of the inner loop is substantially smaller than that of the outer loop and is positioned along the same plane for maximum magnetic coupling.

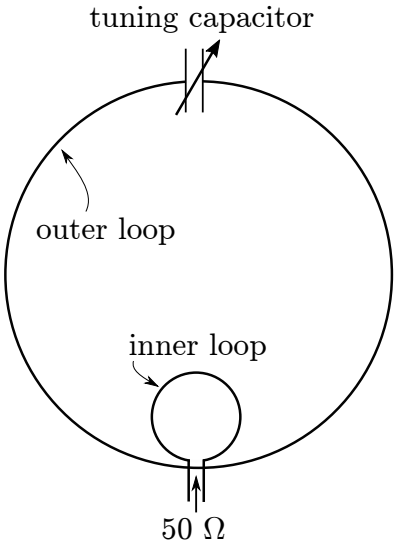

Figure 4.49: Loop antenna design [69].

Constructing the small loop antenna for testing was quick and easy using semi-rigid coaxial for the outer loop, 2 mm thick copper for the inner loop and a rotary capacitor for tuning. Setting up the antenna was also quick since there were no ground plane radials required. The built antenna is shown in Figure 4.50 and the results of the reflection coefficient is presented in Figure 4.51. The antenna operated at the frequencies of interest and had a very narrow bandwidth of less than a couple hundred kHz, finer than the network analyzer's sample spacing. The antenna's resonance was sensitive to slight changes to the tuning capacitor which, along with its low bandwidth, may be problematic in large arrays. A more permanent small loop antenna could be built out of copper pipe and in the shape of either a hexagon or square.

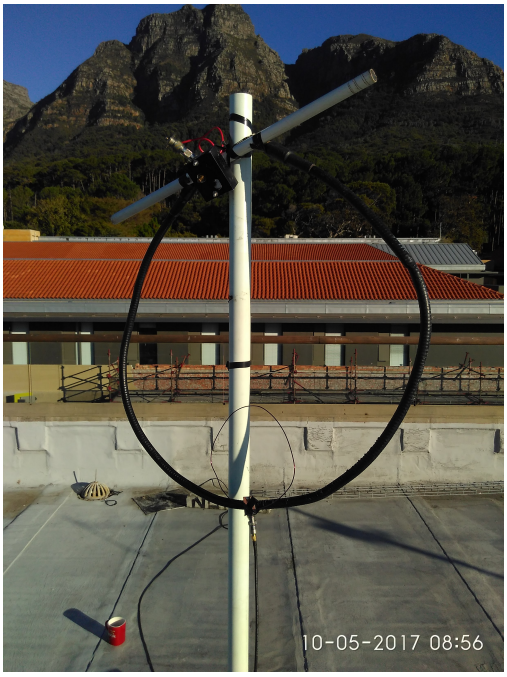

Figure 4.50: Picture of loop antenna tested.

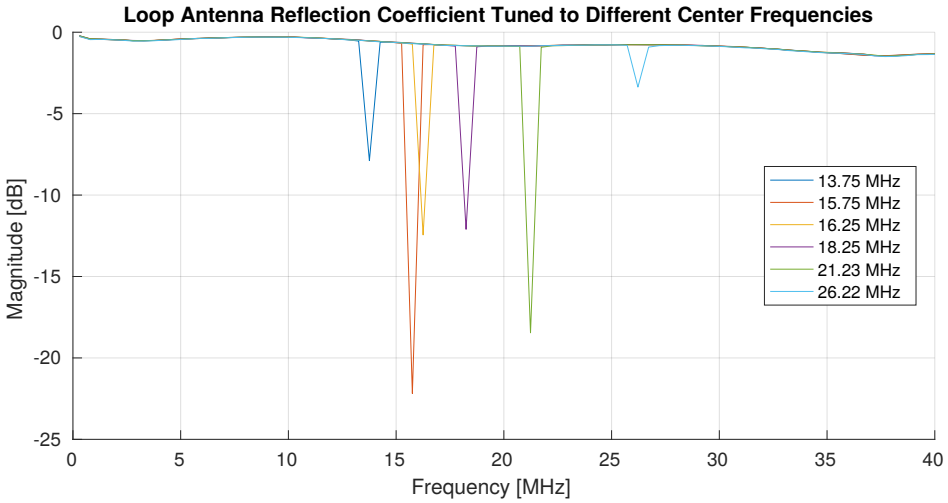

Figure 4.51: Results of small loop antenna in Figure 4.50.

4.5.2 Monopole Antenna

The ideal quarter wavelength monopole is situated vertically on an infinitely large horizontal perfectly conducting ground plane and is a quarter of the operating wavelength tall. The impedance of a monopole is capacitive at frequencies below resonance and inductive at frequencies above resonance. The radiation resistance is 37 Ω at resonance and increases with frequency [70].

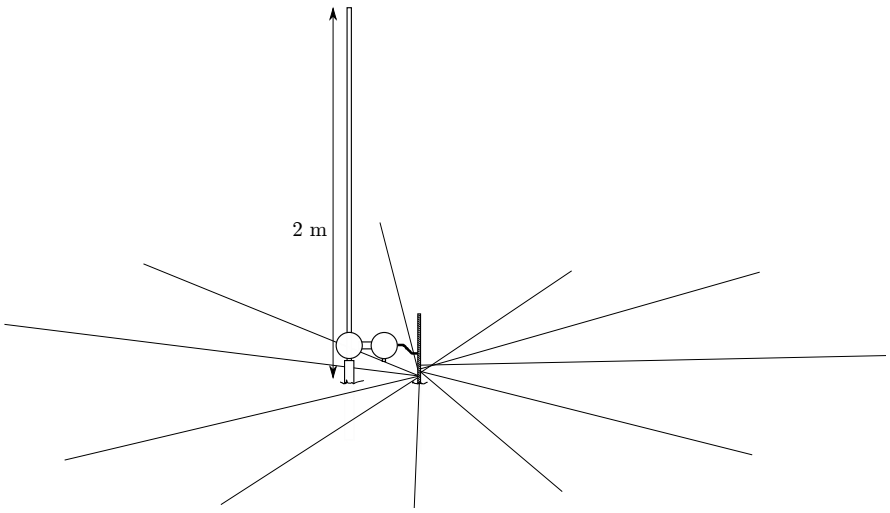

Figure 4.52: Illustration of monopole antenna ontop of radial ground plane.

The beam pattern of the monopole antenna has a null pointing vertically, which helps reduce ionospheric clutter however maximum directivity points towards the transmitter. The bandwidth of a monopole can be increased by increasing the diameter of the monopole [70]. The impedance of an ideal monopole of height H and thickness a has been solved by [70] and is reproduced below:

$$R_{monopole} = 15[(2 + 2\cos b)\mathrm{Cin}(b) - \cos b\mathrm{Cin}(2b) - 2\sin b\mathrm{Si}(b) + \sin b\mathrm{Si}(2b)], \quad (4.6)$$

$$X_{monopole} = -15\Bigg\{\sin 2\beta H\left[-\gamma + \ln\frac{H}{\beta a^2} + 2\mathrm{Ci}(2\beta H) - \mathrm{Ci}(4\beta H)\right] - \cos 2\beta H[2\mathrm{Si}(2\beta H) - \mathrm{Si}(4\beta H)] - 2\mathrm{Si}(2\beta H)\Bigg\}, \tag{4.7}$$

where Si, Ci, and Cin are sine and cosine trigonometric integrals, $b = 4\pi\frac{H}{\lambda_c}$, $\gamma = 0.5772$ is Euler's constant, and $\beta = \frac{2\pi}{\lambda_c}$. The impedance of a 2 m long (resonant at 37.5 MHz), 22 mm thick monopole antenna is plotted in Figure 4.53 where it can be seen that the antenna looks capacitive below resonance and inductive above resonance. Figure 4.53 also reveals that the radiation resistance of the antenna is 37 Ω at resonance and increases with frequency within the region of interest. A matching circuit was designed to allow the center frequency to be tunable whilst being as simple as possible. It was decided to use an antenna that is electrically small at the highest frequency so that the impedance of the antenna is always capacitive. The matching circuit consists merely of an inductor of which the inductance can be increased by inserting a ferromagnetic rod into the coil. This coil is attached in series with the antenna so that the coil's inductance cancels with the capacitive antenna. The monopole antenna is illustrated in Figure 4.52, pictured in Figure 4.54 and the matching circuit pictured in Figure 4.55. The reflection coefficient results of the monopole tuned at different center frequencies is shown in Figure 4.56.

The monopole was quick to construct and to mount. The total cost of materials per antenna amounted to ZAR 184.78 where the most expensive component was the copper pipe at ZAR 150 per 2 m. The radiating element itself is 22 mm diameter copper pipe which is attached to two PVC electrical junction boxes housing the matching circuit and a female BNC connector. The matching circuit coil is made from 2 mm enameled copper and consists of 9 turns and an inner diameter of 10 mm. The monopole took longer to set up than the loop antenna due to the ground radials, however setting up was still less time consuming than the conical antenna.

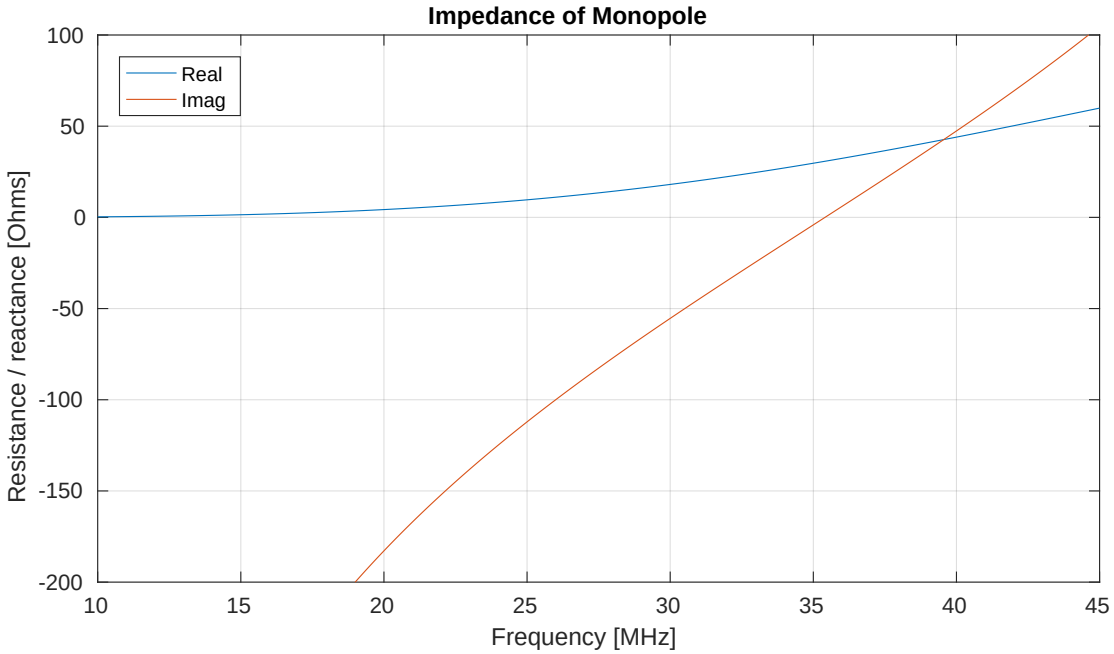

Figure 4.53: Calculated impedance of monopole antenna with length of 2 m and thickness of 22 mm.

Figure 4.54: Monopole antenna mounted on the Menzies building roof, UCT.

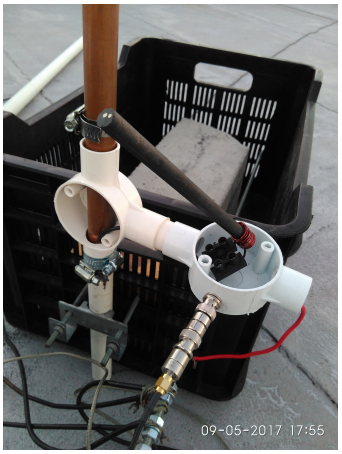

Figure 4.55: Tunable inductor attached in series with the monopole. The inductance is increased as the ferromagnetic rod is inserted into the coil, thus lowering the center frequency.

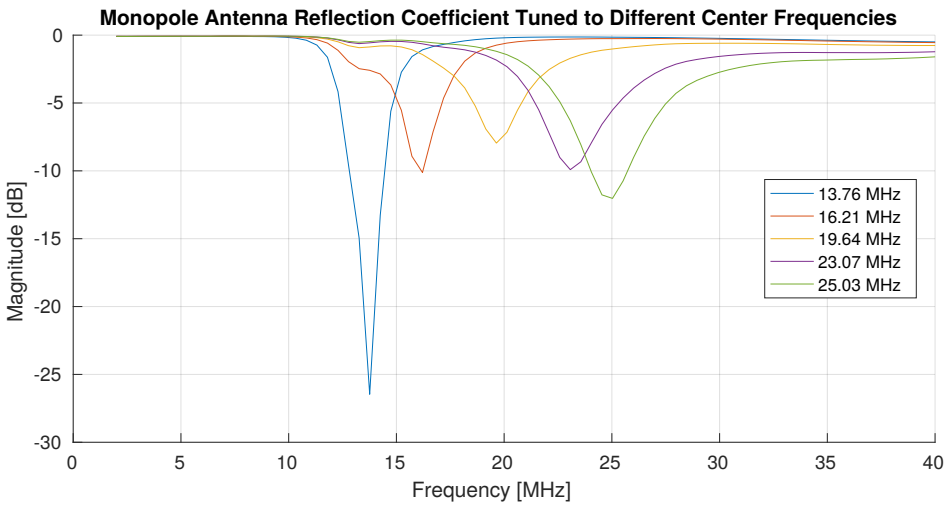

Figure 4.56: Empirical results of monopole antenna in Figure 4.54.

4.5.3 Choice Between Monopole and Small Loop Antenna

The small loop antenna beam pattern has a null that can be steered towards the transmit antenna which would improve isolation. It is also the easiest of the two antennas to setup and break down since no ground radials are required. The beam pattern of the small loop antenna points towards the ionosphere which increases ionospheric clutter. Although the center frequency of the small loop antenna is selectable, the narrow bandwidth makes it susceptible to failure. A slight mistuning of the antenna may cause the operating frequency of the antenna to be outside of the frequency of interest and since multiple receive antennas will be used, the chances of one of the antennas being mistuned is greater.

The monopole antenna beam pattern has a vertical null and lower gain pointing towards the ionosphere, reducing ionospheric clutter. The bandwidth of the monopole is much greater (in the order of a couple MHz) than that of the loop antenna which makes the monopole easier to tune to the desired frequency and less likely for a mistuned antenna to render the captured signal unusable. The ground radials required by the monopole makes it longer to setup and pack up. Being omnidirectional in azimuth means that the monopole has high gain pointing towards the transmit antenna.

The monopole was chosen for the receive antenna array because of its ease of construction and its broader bandwidth compared to the loop antenna. Six of these antennas were constructed and used in a six element linear antenna array. Beam forming is employed to introduce an azimuthal beam width on receive, which can be electronically steered and provide a means to discriminate between targets by their angle of arrival.

4.5.4 Beam Steering

A monopole antenna alone is not sufficient for target discrimination since the beam pattern is uniform in the horizontal plane. Targets can be detected using a monopole antenna however the only target characteristics that can be determined are range and velocity.

The beam width is improved by adding the signals received from multiple antennas using a scheme known as beam steering. A simple linear phase array is implemented by placing two antennas a half wavelength apart from each other as illustrated in Figure 4.57. An echo from a distant target will approach the receive array as a plane wave at angle θ and will therefore induce a voltage at each antenna with a different phase depending on the direction of the plane wave.

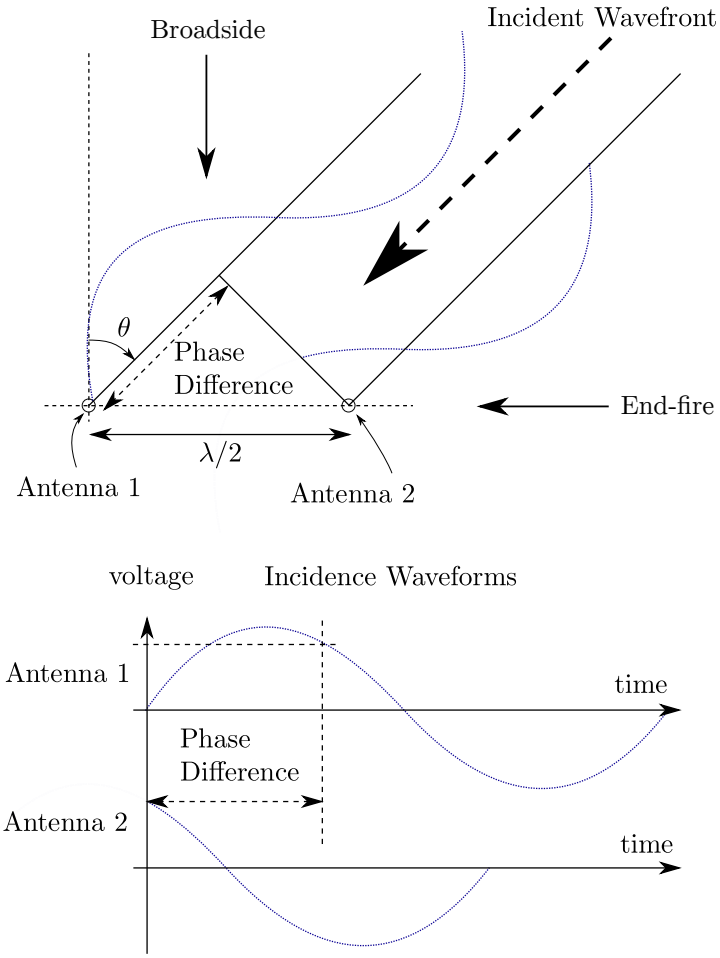

Figure 4.57: Phase difference between two antennas spaced a quarter wavelength apart. Plane wave is travelling towards antennas at angle θ from broadside.

If the voltage waveforms from the two antennas are added (such as in Figure 4.58), their magnitudes will add constructively when they are in phase (incident waveform is perpendicular to the two antennas, also known as broadside) and will add destructively when they are out of phase (incident waveform comes from the

side of the array, also known and end-fire). The beam pattern of two monopole antennas pointing at broadside is shown in Figure 4.60(a). Since the phase of the signal at both antennas are in phase when the plane wave approaches at boresight (90° of Figure 4.60(a)), the gain of the antenna is maximum at that angle. A null exists at 0° and 180° of Figure 4.60(a) since the phase of the signal at each antenna will be exactly 180° out of phase and will therefore cancel each other out. The beam width can be reduced by using multiple antennas which also increases the receive aperture. The beam can then be steered by implementing a phase shift (ϕ) to each individual antenna's waveform as illustrated in Figure 4.59,

$$\phi_n = 2\pi n \frac{d}{\lambda} sin(\theta) \quad \text{[rad]} \tag{4.8}$$

where n refers to the n'th antenna starting at $n = 0$, ϕ_n is the phase shift applied to the n'th antenna, d is the distance between the antennas, and θ is the direction at which the beam is to be steered.

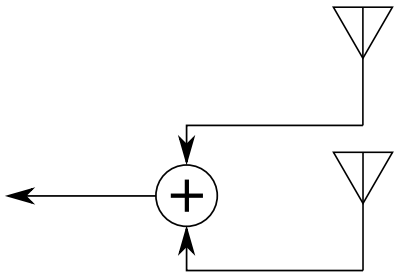

Figure 4.58: Voltage signal from two antennas added to form a single directional antenna.

The resulting beam pattern of an array of isotropic antennas is known as the array factor (AF) and is derived as [71],

$$AF(\alpha, \theta) = \frac{\sin\left(\frac{N\pi d}{\lambda}(-\sin\alpha + \sin\theta)\right)}{N\sin\left(\frac{\pi d}{\lambda}(-\sin\alpha + \sin\theta)\right)}, \tag{4.9}$$

where θ is the beam steering angle from broadside and α is the azimuth plotting axis. The AF can be computed over azimuth for different look angles (θ) using (4.8) and (4.9) and the half power beam width measured from the results.

The result of beam steering two antennas at 0° and 15° are shown in Figure 4.60.

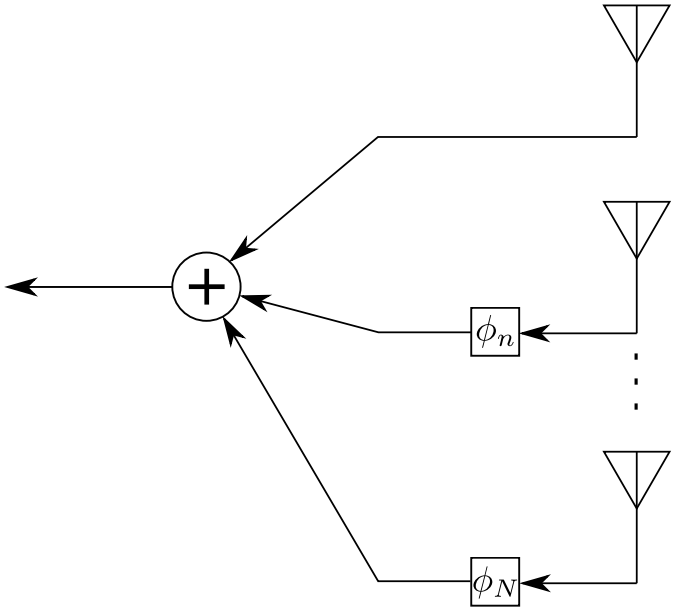

Figure 4.59: Multiple antennas forming a linear array with phase shifts ϕ_n and added resulting in a single directional antenna.

It is apparent that the beam width is large and that undesirable effects occur when the beam is steered only slightly. The beam width is reduced by increasing the size of the array, as is shown in Figure 4.61. The beam patterns in Figure 4.61 are simulations of the HF radar setup during the trials, which consists of 6 antennas spaced 8.08 m apart. A list of AF plots of 6 elements spaced at 8.08 m apart at different operating frequencies and steer directions are plotted in Appendix B.

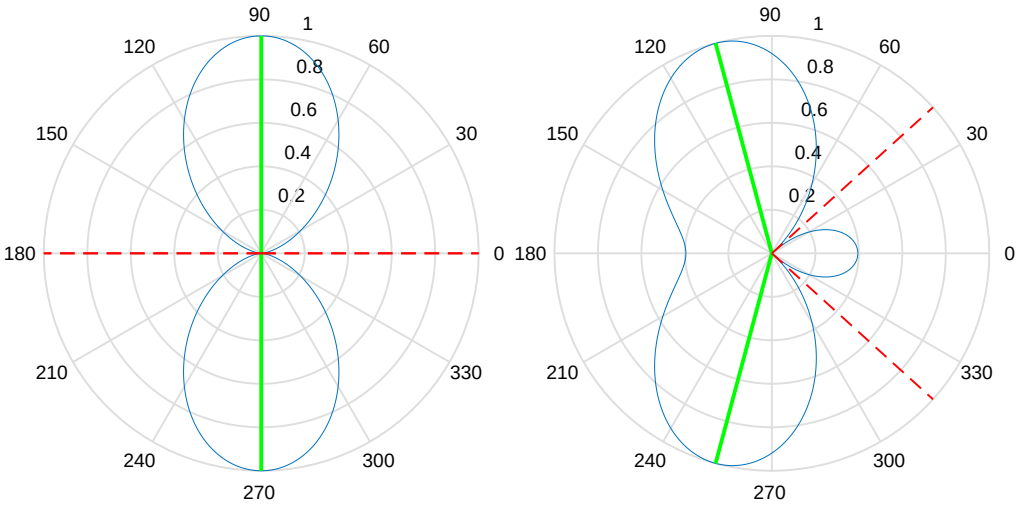

(a) Aiming towards boresight (b) Aiming 15 degrees from boresight

Figure 4.60: Beam pattern of 2 element linear array of half wavelength spacing. Green lines point in the direction of the beam and the red lines point in the null directions. The antenna array in the above figures are positioned horizontally.

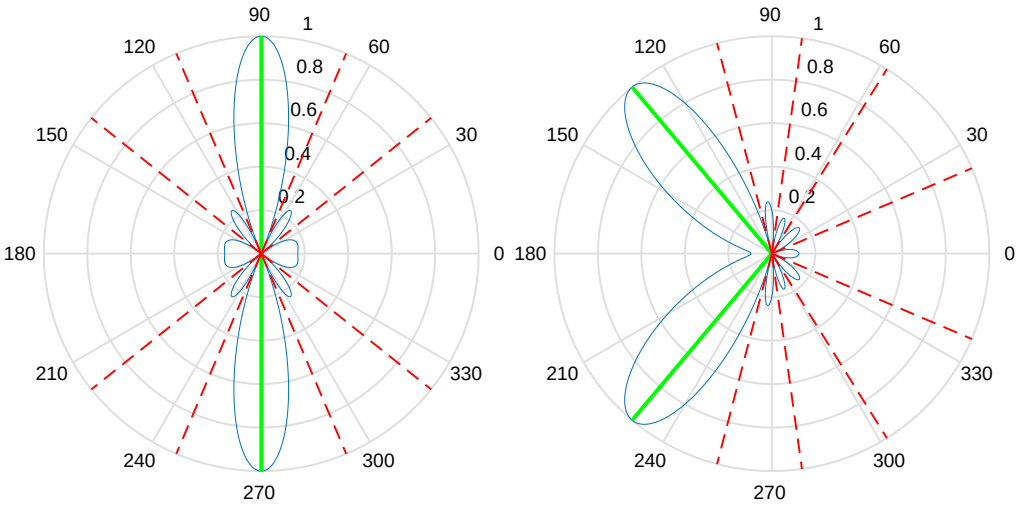

(a) Beam steered towards boresight. (b) Beam steered 40° from boresight.

Figure 4.61: Beam pattern of 6 element linear array with operating frequency of 16 MHz and element spacing of 8 m. Green lines point in the direction of the beam and the red lines point in the null directions. The antennas are positioned horizontally.

Chapter 5

Results

The assembled HF radar is represented in Figure 5.1 in its entirety. The radar consists of four nodes, one node for transmit (master) and three nodes for receive (slaves). Two receive elements were attached to a receive node, resulting in a 6 element receive array. Trials were conducted at UCT's rugby field on Upper Campus and at the Institute for Maritime Technologies (IMT) in Simon's Town. At both locations the complete radar was set up with one transmitter and six receiver elements.

The receive antennas were attached to the RF receivers using identical 10 m long Radio Guide RG58 coaxial cables. The transmit antenna was attached to the transmit node using two LMR400 coaxial cables attached together with a total length of 23 m. Each antenna utilised of 10 ground radials extending between 8 m and 12 m. The three synchronisation cables are labelled by the two devices in order of node name that the cable is attached to, more specifically Ma-Sl1, Sl1-Sl2, Sl2-Sl3. The lengths of the synchronisation cables are 25.00 m, 16.80 m, and 18.08 m respectively. The PRI for all experiments was kept at 500 µs and the pulse length, unless otherwise stated, was kept at 20 µs.

The conical antenna used for transmit on the rugby field is visible in Figure 5.2 along with the six receive monopole antennas. The transmitter equipment in Figure 5.2 is present in the green canopy and the receivers are lying on the grass

near the receive antennas. Measurements were taken on the rugby field on the 19th of August 2017 and the recordings are summarised in Table 5.1. The receive antennas were all spaced 8.08 m apart from each other and the transmit antenna was placed 9.6 m away from channel 1. The overall length of the setup was 50 m.

Recordings were taken at IMT on Tuesday the 22nd (summarised in Table 5.2) and Thursday the 24th (summarised in Tables 5.3 and 5.4) of August 2017. Four of the six receive monopole antennas are visible in Figure 5.3. The receivers were kept inside the tents in Figure 5.3 to protect them from the rain and the transmitter equipment was kept in-doors. A monopole antenna was used for transmit on the Tuesday and was replaced with a conical antenna on the Thursday. The receive antennas were all spaced 8.08 m apart and the transmit antenna was spaced 8.64 m away from channel 1.

It was discovered at the end of Tuesday at IMT that channel one on receive had the RF switches disconnected from supply. Channel one on the Tuesday set of results listed in Table 5.2 contains no useful recordings. The issue with channel one was rectified on Thursday and therefore all channels were correctly recording in Tables 5.3 and 5.4. This was a separate issue to that circled in Figure 4.44.

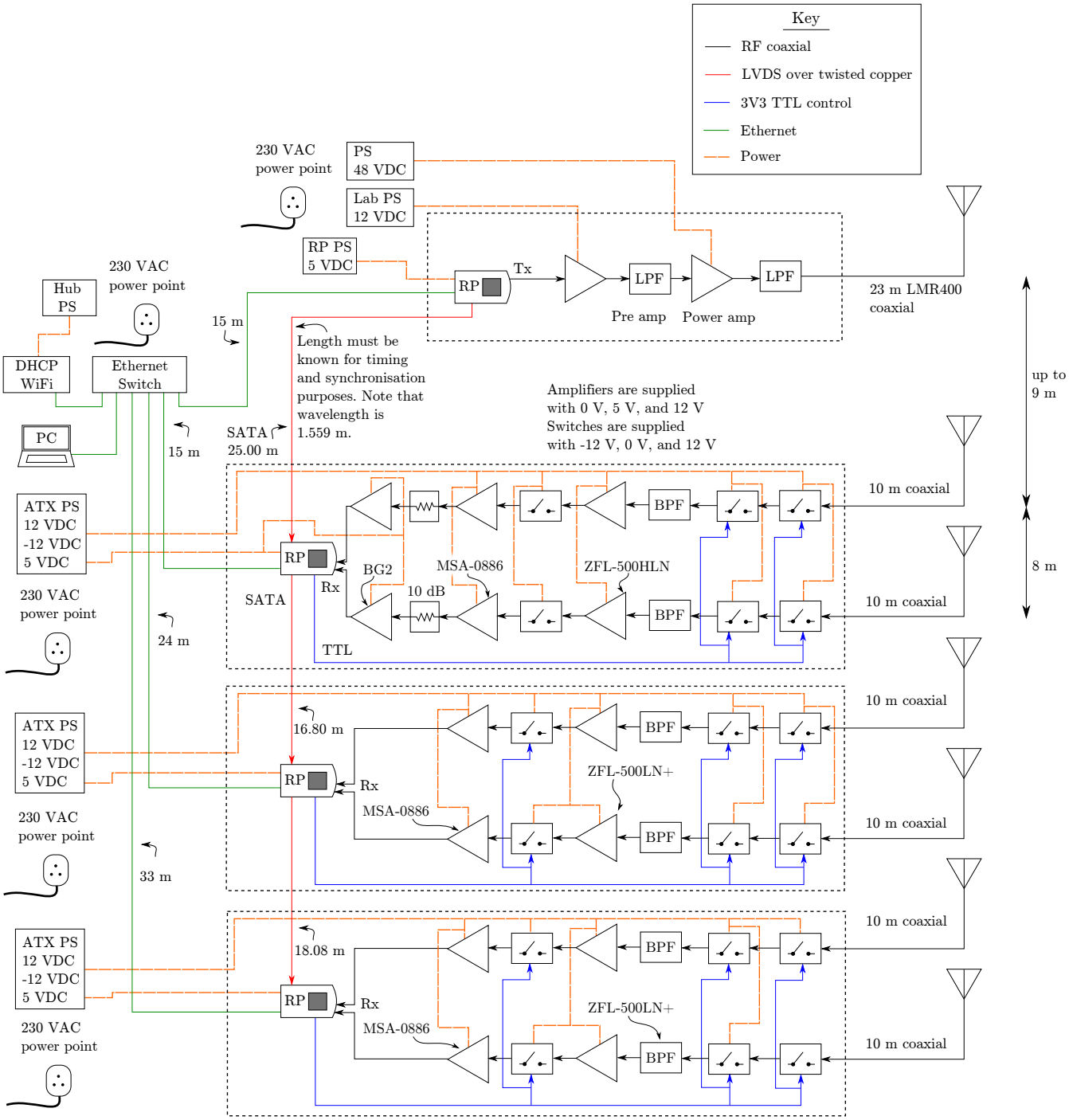

Figure 5.1: Complete system block diagram of the demonstrator setup used for the trials.

Figure 5.2: Picture of the HF radar set up on the rugby field at UCT Upper Campus. The green canopy contains the transmit equipment and three black boxes (not easily seen in the picture) contains the receive equipment. The conical antenna on the right connects to the transmit equipment and the six monopoles are attached to the receive equipment.

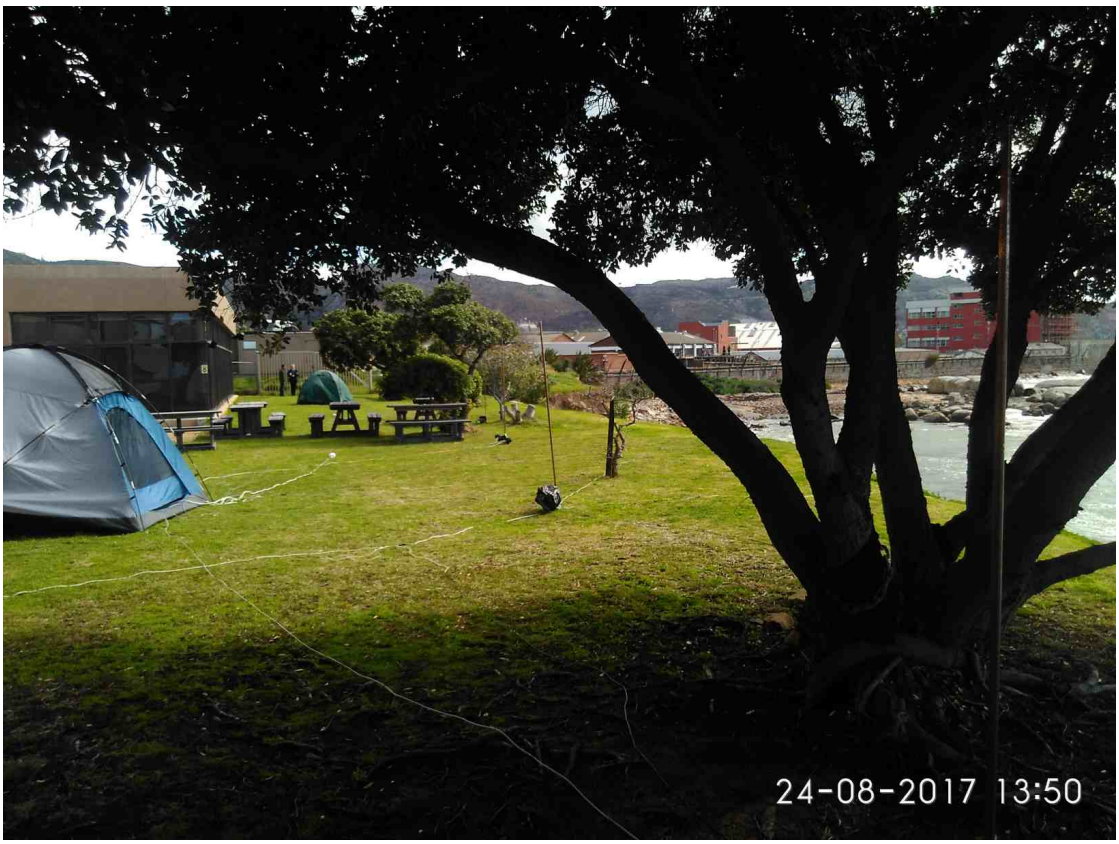

Figure 5.3: Picture of the HF radar set up at the IMT facilities in Simon's Town. The tents house the receiver equipment to protect them from the rain and the transmit conical antenna is not visible in the picture (behind a tree).

Table 5.1: List of recordings taken at the UCT Rugby Field on the 19th of August 2017. The transmit power was not properly recorded during these trials however the transmit power was set close to the rated power of the transmit amplifier of 600 W. The PRI for all experiments was 500 µs.

Experiment name	Operating Frequency [MHz]	Bandwidth [kHz]	Integration [samples]	Pulse Length [µs]
INT-5000-NBUFF-10-BW-2e6	16	2000	5000	20
NBUFF-10-INT-2000-FULLBW	18.75	12400	2000	20
NBUFF-2-BW-FULLBW-INT-1000	18.75	12400	1000	20
NBUFF-20-INT-1000-BW-2	16	2000	1000	20
NBUFFS2-INT-5000-BW-0.15	16	150	5000	20
NBUFFS2-INT-5000-BW-1	16	1000	5000	20
NOINT-20NBUFF-FULLBW	18.75	12400	1	20
NOISE-INT-100	16	2000	100	20
NOISE-INT-100-NBUFF-10-NIGHT	16	2000	100	20
NOISE-INT-10000	16	2000	10000	20
TURNED-TRANSMITTER-ON-TOO-LATE	16	2000	5000	20

Table 5.2: List of recordings taken at the IMT facility on Tuesday the 22nd of August 2017. The naming convention used in this table is, from left to right, center frequency [MHz], bandwidth [kHz], number of buffers, number of integrations, attenuation before transmit [dB], and pulse length [μs]. The transmit power is approximately 600 W if 10 dB of attenuation before the transmitter is used. The PRI for all the experiments was 500 μs.

Experiment Name	Operating Frequency [MHz]	Bandwidth [kHz]	Integration [samples]	Pulse Length [μs]
looking-for-mountains	16	150	5000	20
looking-for-mountains-with-fixed-switches	16	150	5000	20
noise-int-200	16	2000	200	20
sea-fc-16-b-100-n-10-int-100-att-10	16	100	100	20
sea-fc-16-b-1000-n-10-int-1000-att-10-chirp-30	16	1000	1000	30
sea-fc-16-b-1000-n-10-int-500-att-10-chirp-30	16	1000	500	30
sea-fc-16-b-12000-n-10-int-100-att-10-chirp-20	16	12000	100	20
sea-fc-16-b-150-n-30-int-200-att-10	16	150	200	20
sea-fc-16-b-2000-n-10-int-100-att-10	16	2000	100	20
sea-fc-16-b-2000-n-30-int-200-att-10	16	2000	200	20

Table 5.3: List of recordings taken at the IMT facility on Thursday the 24th of August 2017. The naming convention used in this table is, from left to right, center frequency [Hz], bandwidth [Hz], number of integrations, number of buffers, PRI [s], and pulse length [s]. The transmit power was set close to the rated power of the transmit amplifier of 600 W and the PRI was 500 µs for all experiments.

Experiment Name	Operating Frequency [MHz]	Bandwidth [kHz]	Integration [samples]
fc-14M-B-0.15M-int-100-nbuffs-40-pri-0.0005u-chirp_duration-2e-05u	14	150	100
fc-14M-B-0.1M-int-100-nbuffs-40-pri-0.0005u-chirp_duration-2e-05u	14	100	100
fc-14M-B-2M-int-100-nbuffs-40-pri-0.0005u-chirp_duration-2e-05u	14	2000	100
fc-16M-B-0.15M-int-100-nbuffs-40-pri-0.0005u-chirp_duration-2e-05u	16	150	100
fc-16M-B-0.1M-int-100-nbuffs-40-pri-0.0005u-chirp_duration-2e-05u	16	100	100
fc-16M-B-0.5M-int-100-nbuffs-40-pri-0.0005u-chirp_duration-2e-05u	16	500	100
fc-16M-B-1M-int-100-nbuffs-40-pri-0.0005u-chirp_duration-2e-05u	16	1000	100
fc-16M-B-2M-int-100-nbuffs-40-pri-0.0005u-chirp_duration-2e-05u	16	2000	100
fc-16M-B-2M-int-1000-nbuffs-10-pri-0.0005u-chirp_duration-2e-05u	16	2000	1000
fc-16M-B-2M-int-200-nbuffs-10-pri-0.0005u-chirp_duration-2e-05u	16	2000	200
fc-16M-B-2M-int-2000-nbuffs-10-pri-0.0005u-chirp_duration-2e-05u	16	2000	2000
fc-16M-B-2M-int-300-nbuffs-10-pri-0.0005u-chirp_duration-2e-05u	16	2000	300
fc-16M-B-2M-int-400-nbuffs-10-pri-0.0005u-chirp_duration-2e-05u	16	2000	400
fc-16M-B-2M-int-4000-nbuffs-10-pri-0.0005u-chirp_duration-2e-05u	16	2000	4000
fc-16M-B-2M-int-500-nbuffs-1-pri-0.0005u-chirp_duration-2e-05u	16	2000	500
fc-16M-B-2M-int-500-nbuffs-10-pri-0.0005u-chirp_duration-2e-05u	16	2000	500
fc-16M-B-3M-int-100-nbuffs-40-pri-0.0005u-chirp_duration-2e-05u	16	3000	100
fc-16M-B-4M-int-100-nbuffs-40-pri-0.0005u-chirp_duration-2e-05u	16	4000	100
fc-16M-B-5M-int-100-nbuffs-40-pri-0.0005u-chirp_duration-2e-05u	16	5000	100

Table 5.4: List of recordings taken at the IMT facility on Thursday the 24th of August 2017 continued. The naming convention used in this table is, from left to right, center frequency [Hz], bandwidth [Hz], number of integrations, number of buffers, PRI [s], and pulse length [s]. The transmit power was set close to the rated power of the transmit amplifier of 600 W and the PRI was 500 µs for all experiments.

Experiment Name	Operating Frequency [MHz]	Bandwidth [kHz]	Integration [samples]
fc-18.75M-B-10M-int-100-nbuffs-40-pri-0.0005u-chirp_duration-2e-05u	18.75	10000	100
fc-18M-B-0.15M-int-100-nbuffs-40-pri-0.0005u-chirp_duration-2e-05u	18	150	100
fc-18M-B-0.5M-int-100-nbuffs-40-pri-0.0005u-chirp_duration-2e-05u	18	500	100
fc-18M-B-2M-int-100-nbuffs-40-pri-0.0005u-chirp_duration-2e-05u	18	2000	100
fc-18M-B-2M-int-1000-nbuffs-20-pri-0.0005u-chirp_duration-2e-05u	18	2000	1000
fc-20M-B-0.15M-int-100-nbuffs-40-pri-0.0005u-chirp_duration-2e-05u	20	150	100
fc-20M-B-2M-int-100-nbuffs-40-pri-0.0005u-chirp_duration-2e-05u	20	2000	100
fc-22M-B-0.15M-int-100-nbuffs-40-pri-0.0005u-chirp_duration-2e-05u	22	150	100
fc-22M-B-2M-int-100-nbuffs-40-pri-0.0005u-chirp_duration-2e-05u	22	2000	100
fc-24M-B-0.15M-int-100-nbuffs-40-pri-0.0005u-chirp_duration-2e-05u	24	150	100
fc-24M-B-2M-int-100-nbuffs-40-pri-0.0005u-chirp_duration-2e-05u	24	2000	100
test10	16	2000	500

5.1 Stationary Target Detection from One Channel

Figure 5.4 shows the first range line provided by the RP of Channel 6 from experiment "sea-fc-16-b-1000-n-10-int-500-att-10-chirp-30". This experiment took place at the IMT facility on the 22nd of August 2017 and operated at a center frequency of 16 MHz, a bandwidth of 1 MHz, and a transmit power close to 600 W. A range line provided by the RP consists of multiple range lines integrated during the experiment and in the case of Figure 5.4, 500 range lines were integrated. The two peaks on the left and right hand sides of Figure 5.4 are ringing effects from the RF switches changing state. The lack of noise at the beginning of the top plot in Figure 5.4 is due to the RF switch being turned off during that time. The top plot in Figure 5.4 contains the raw samples from the ADC after integration, taking note that these samples are recorded from the second nyquist zone. The middle and bottom plots are in-phase and quadrature components of the top plot. A highly attenuated chirp is visible on the far left hand side of the middle and bottom plots in Figure 5.4 which is the direct feed through signal leaking through the switches.

The results plotted in Figure 5.5 were taken from the IMT facility with a center frequency of 16 MHz, bandwidth of 150 kHz corresponding to a range resolution of 1 km, and transmit power close to 600 W. The plotted results are from only one of the six receivers after pulse compression and integration. The four labels in Figure 5.5 indicate potential targets which are circled in Figure 5.6. The four possible targets include the Silver Mine nature reserve 8 km away, Hottentots-Holland Mountain Catchment Area at 36 km away, Kogelberg Nature Reserve at 42 km away, and Hottentot-Holland Nature Reserve at 50 km away.

The results shown in Figure 5.7 are from experiment "sea-fc-16-b-1000-n-10-int-1000-att-10-chirp-30" which was recorded at the IMT facility with a center frequency of 16 MHz, bandwidth of 1 MHz, pulse length of 30 μs and transmit power close to 600 W. The plots in Figure 5.7 was taken from a single element's recordings after pulse compression and the same data is used for all three graphs. The number of pulses integrated is varied from 1000 pulses to 10000 pulses to 100000

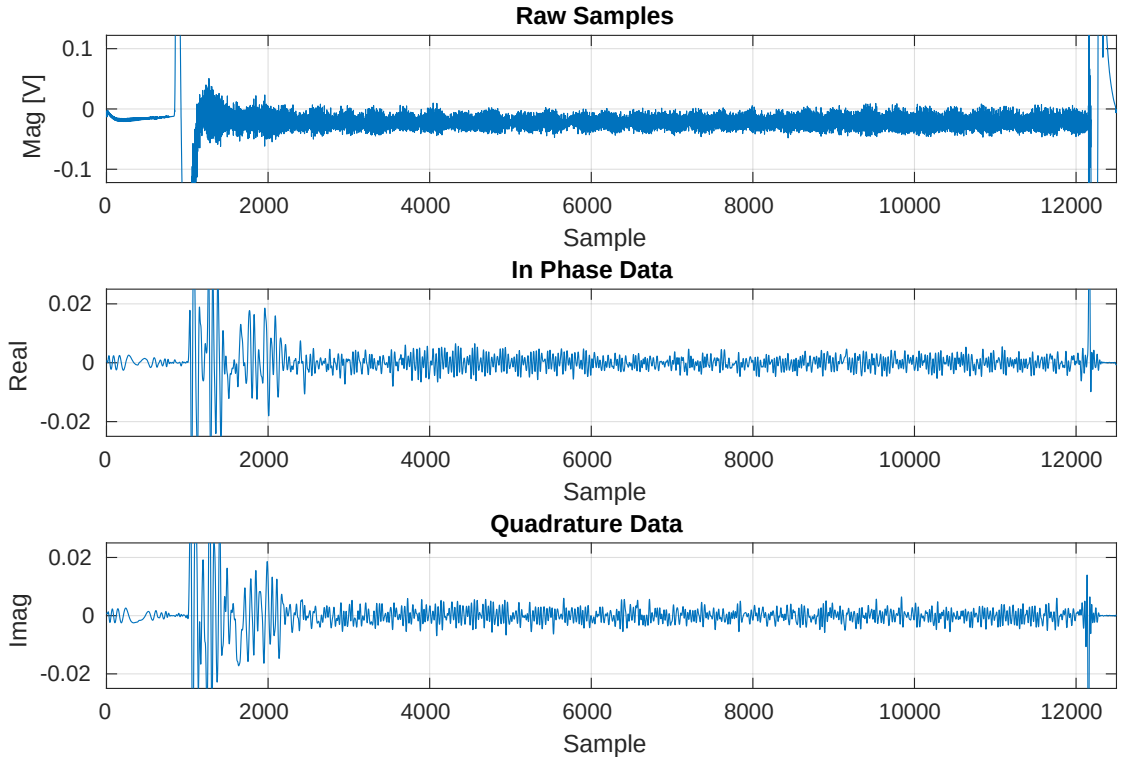

Figure 5.4: First range line produced by Red Pitaya for experiment "sea-fc-16-b-1000-n-10-int-500-att-10-chirp-30" from channel 6 only. The top plot is the raw samples after integrating 500 pulses. Middle and bottom plots are In Phase and Quadrature respectively of the top plot. All three plots contain the same 500 pulses integrated.

pulses and the results scaled by the number of integrations. It is clear that targets are emerging out of the noise as the number of integrations increases. The center frequency is 16 MHz and the bandwidth 1 MHz, which corresponds to a range resolution of 150 m. The finer resolution in Figure 5.7 is apparent when compared to the coarser 1 km range resolution in Figure 5.5.

Since all six receivers are made to be as identical as possible, the data received on all six channels should appear almost identical. Experiment "fc-16M-B-2M-int-4000-nbuffs-10-pri-0.0005u-chirp_duration-2e-05u" was conducted at Simon's Town on the Thursday when the first channel was fixed and the envelope of all six channels are plotted in Figure 5.8 after pulse compression and integration. Dominant targets appear to be at the same range for each channel in Figure 5.8.

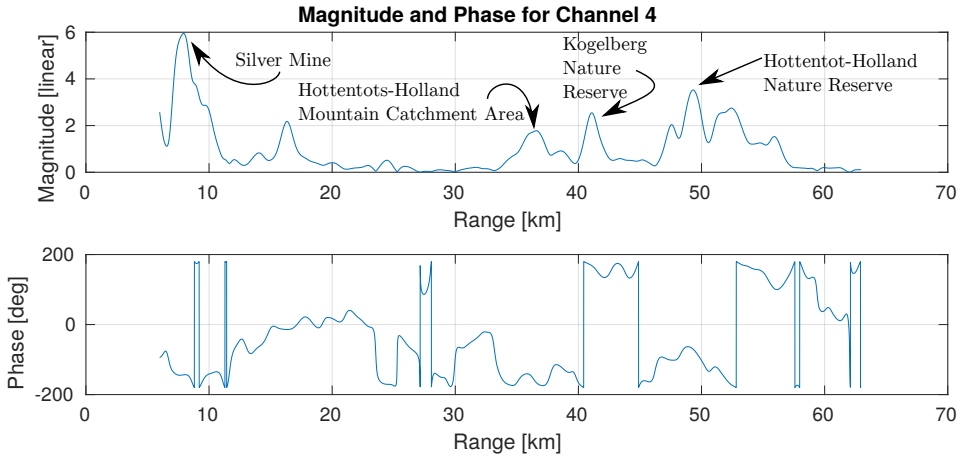

Figure 5.5: Magnitude and phase from experiment "fc-16M-B-0.15M-int-100-nbuffs-40-pri-0.0005u-chirp_duration-2e-05u" with potential targets labelled.

Figure 5.6: Image captured from Google maps with four different areas marked as potential targets seen in Figure 5.5. Two black arrows point in the direction of broadside and end fire.

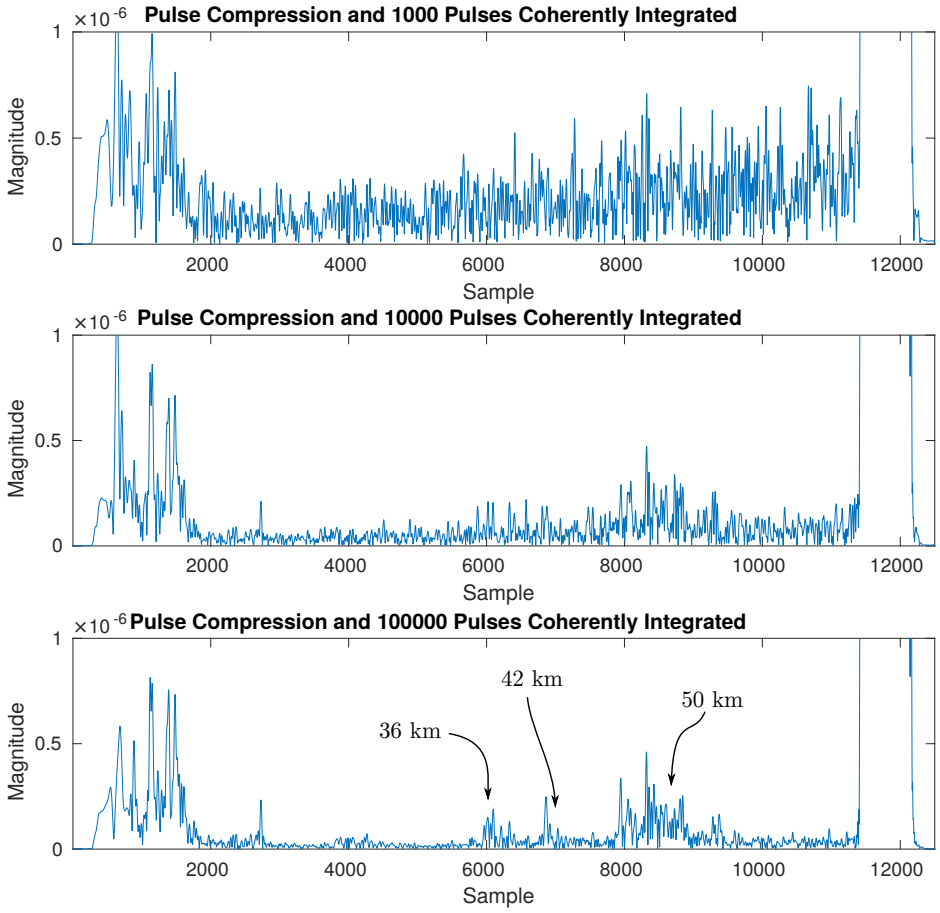

Figure 5.7: Absolute values after pulse compression and integration for experiment "sea-fc-16-b-1000-n-10-int-1000-att-10-chirp-30". This data is from channel 6 and 1000 pulses were integrated during the experiment. The top plot shows a single range line. The middle plot coherently integrated 10 recorded range lines together, resulting in a total integration of 10000 range lines. The bottom plot integrated 100 range lines resulting in a total integration of 100000. The integrated magnitude is divided by the total number of integrations to form the average.

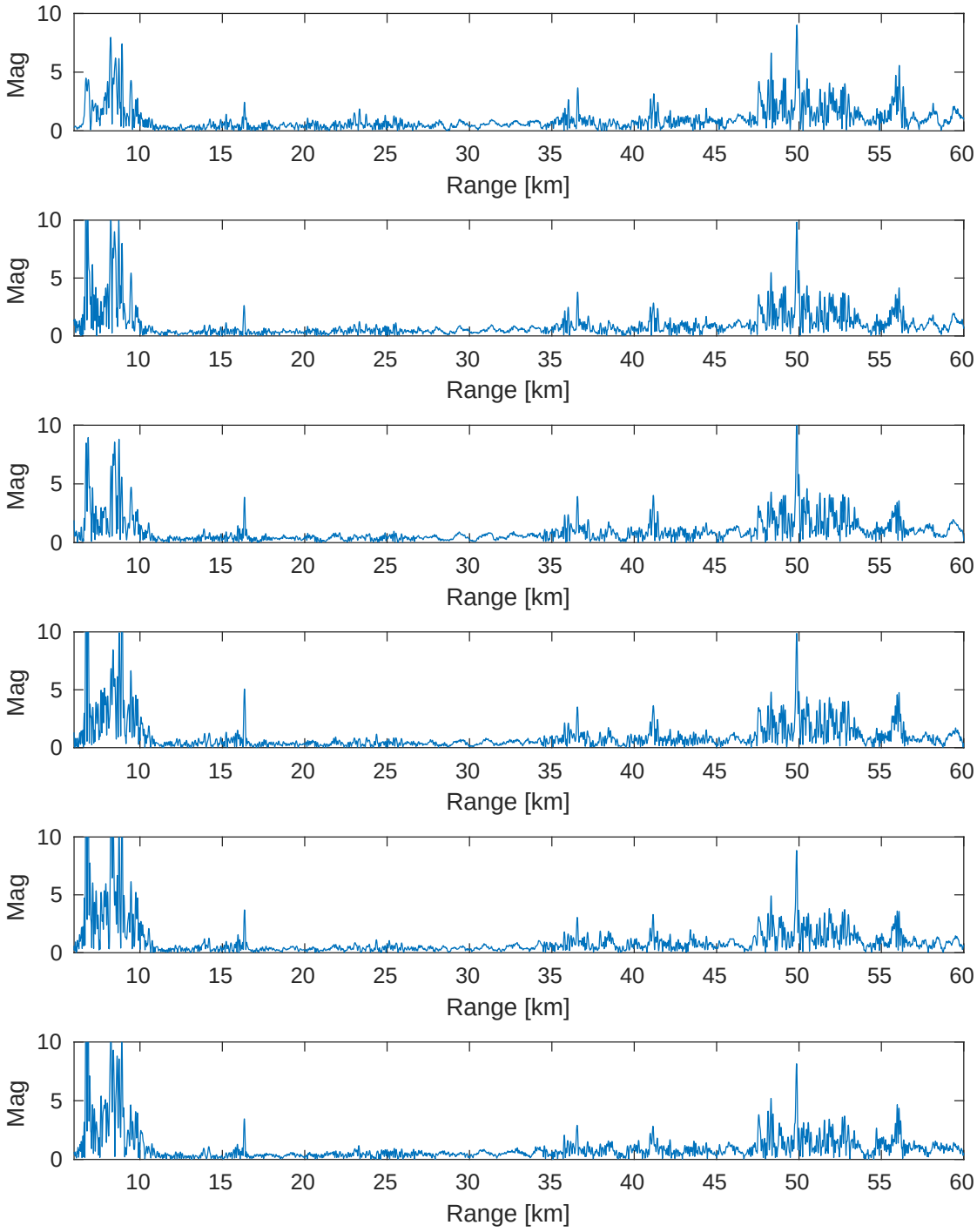

Figure 5.8: All six channels after pulse compression and integrating all the range lines (a total of 1668000 pulses over a recording time of 834 seconds). Data taken from "fc-16M-B-2M-int-4000-nbuffs-10-pri-0.0005u-chirp_duration-2e-05u". The magnitude is divided by the total number of integrations.

5.2 Beam Steering and Detection of Stationary Targets

The beam steering method described in Section 4.5.4 was implemented on the data from IMT Thursday. Phase correction described in Section 4.3.8 was applied to all the channels at the appropriate frequency before implementing beam steering. The range resolution (ΔR) is a function of the bandwidth,

$$\Delta R = \frac{c}{2B}. \tag{5.1}$$

The azimuth resolution (θ_{3dB}) is equal to the 3 dB beam width with examples of different operating frequencies and steer directions shown in Appendix B. The beamwidth at broadside with a center frequency of 16 MHz is 27.3° and decreases with frequency.

Range compensation is applied by multiplying each range cell by $R^{1.6}$ as opposed to R^4 to bring targets at near and far ranges to similar power levels for ease of visualisation. A more accurate means of range compensation is to twice subtract the GRWAVE results in Figure 3.6 from the results. A threshold is applied at 5 dB below the peak power value in the region of interest and the resultant detections are overlayed on a map as a red X. Possible targets from the IMT facility are shown in Figure 5.6 and include the mountains in Silver Mine about nine kilometres ahead of broadside, and the Hottentots-Holland Nature Reserve and Kogelberg Nature Reserve mountain ranges 40 km to 50 km away in the eastern end fire direction. The Silver Mine mountains appear to be visible in most of the IMT datasets with the exception of the high bandwidth data where beam forming using the two methods described deteriorate at high fractional bandwidth. A transmit power of approximately 600 W was used for all the experiments in this section.

Figure 5.9 is the result after beam steering on experiment "fc-16M-B-0.15M-int-100-nbuffs-40-pri-0.0005u-chirp_duration-2e-05u". The radar operated at 16 MHz with a bandwidth of 150 kHz and therefore has a range resolution of 1 km. The wavelength at 16 MHz is 18.75 m which satisfies the requirement $d < \frac{\lambda_c}{2}$ to avoid

grating lobes. The result of threshold detection is shown in Figure 5.10 which is overlayed on a map in Figure 5.11.

Both of the possible targets listed earlier are shown as detections in Figure 5.11, including the mountain in Silver Mine, Hottentots-Holland Nature Reserve, and the Kogelberg Nature Reserve mountain ranges. The detections at the Kogelerg and Hottentots-Holland nature reserves spread out over azimuth due to the far range (between 40 km and 50 km) and the large beam width when operating near the end fire region (see Figures B.2(a) and B.2(b)). The Silver Mine detection in Figure 5.11 has very little spread over azimuth due to the short range and because the target angle is close to broadside and therefore the half power beamwidth is at its finest (see Figure B.2(f)).

Figures 5.12 to 5.14 are the processed results of experiment "fc-16M-B-0.5M-int-100-nbuffs-40-pri-0.0005u-chirp_duration-2e-05u". The bandwidth is 500 kHz for this experiment corresponding to a finer range resolution of 300 m. This finer range resolution is apparent in Figure 5.13 when compared to Figure 5.10. Both Silver Mine and the nature reserves are detected in Figure 5.14.

Figures 5.15 to 5.17 are the processed results of experiment "fc-20M-B-0.15M-int-100-nbuffs-40-pri-0.0005u-chirp_duration-2e-05u" which operated at 20 MHz with a bandwidth of 150 kHz. Both the Silver Mine and nature reserve targets are detected in Figure 5.17 however there is also a large false alarm in the ocean to the east of the Figure. This false alarm can be explained from Figures B.4(a) and B.4(b) which reveals strong back lobes. When the beam is steered between 150° and 180° (that is, between 0° and 30° northward from the western side of the array axis), the array will receive echoes from targets between 0° and 30° which is the direction of the nature reserves. The wavelength at 20 MHz is 15 m which does not satisfy the requirement $d < \frac{\lambda_c}{2}$ and therefore grating lobes appear. This also explains the ambiguity observed at look angles close to the end fire directions.

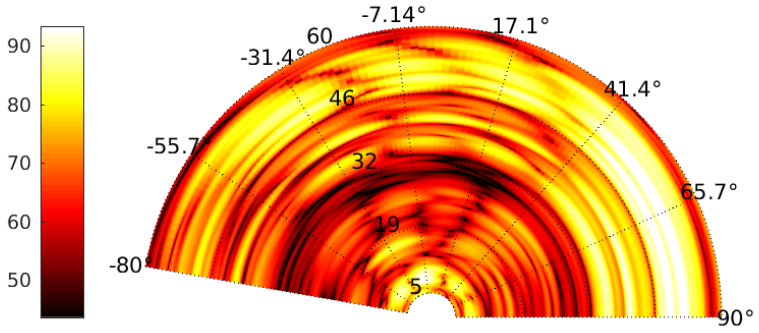

Figure 5.9: Beam steering using the method described in Section 4.5.4 for experiment "fc-16M-B-0.15M-int-100-nbuffs-40-pri-0.0005u-chirp_duration-2e-05u". Range is from 5 km to 60 km and azimuth between -80° and 90°.

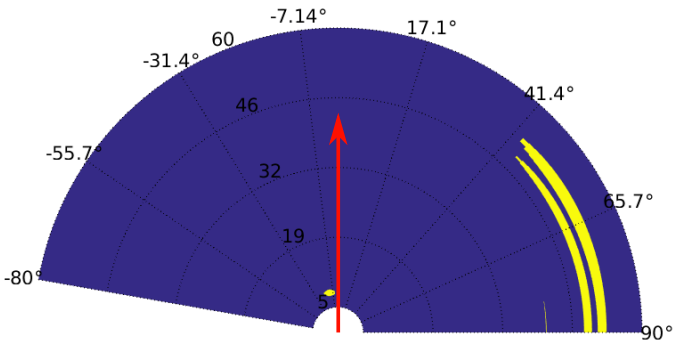

Figure 5.10: Threshold detection applied to the data in Figure 5.9. The red arrow points in the direction of broadside.

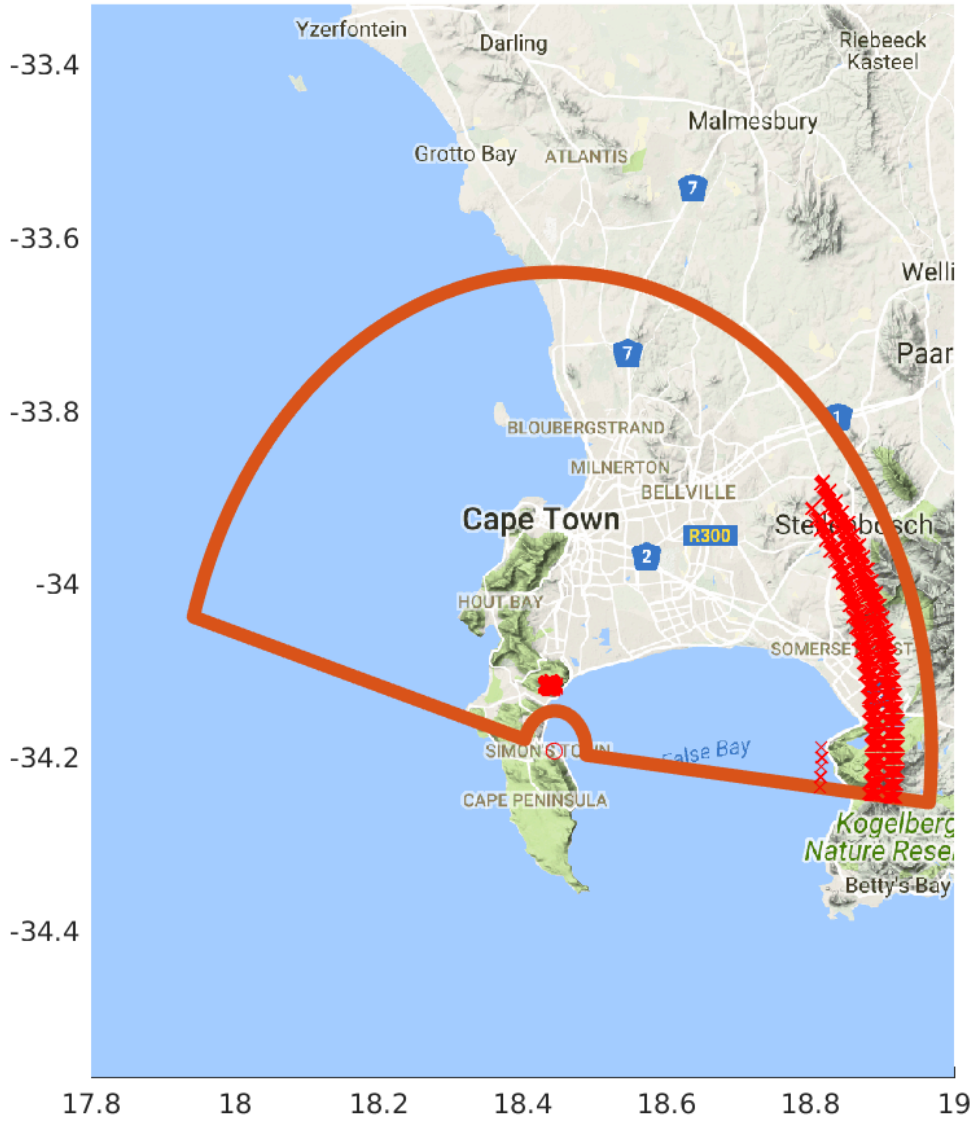

Figure 5.11: Threshold detection from Figure 5.10 overlayed with a terrain view image of Google Maps.

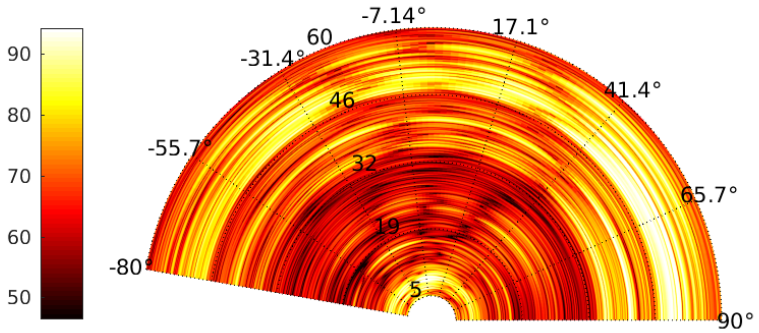

Figure 5.12: Beam steering using the method described in Section 4.5.4 for experiment "fc-16M-B-0.5M-int-100-nbuffs-40-pri-0.0005u-chirp_duration-2e-05u". Range is from 5 km to 60 km and azimuth between -80° and 90°.

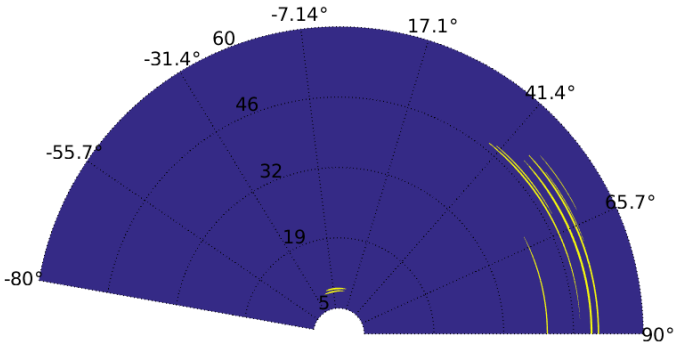

Figure 5.13: Threshold detection applied to the data in Figure 5.12.

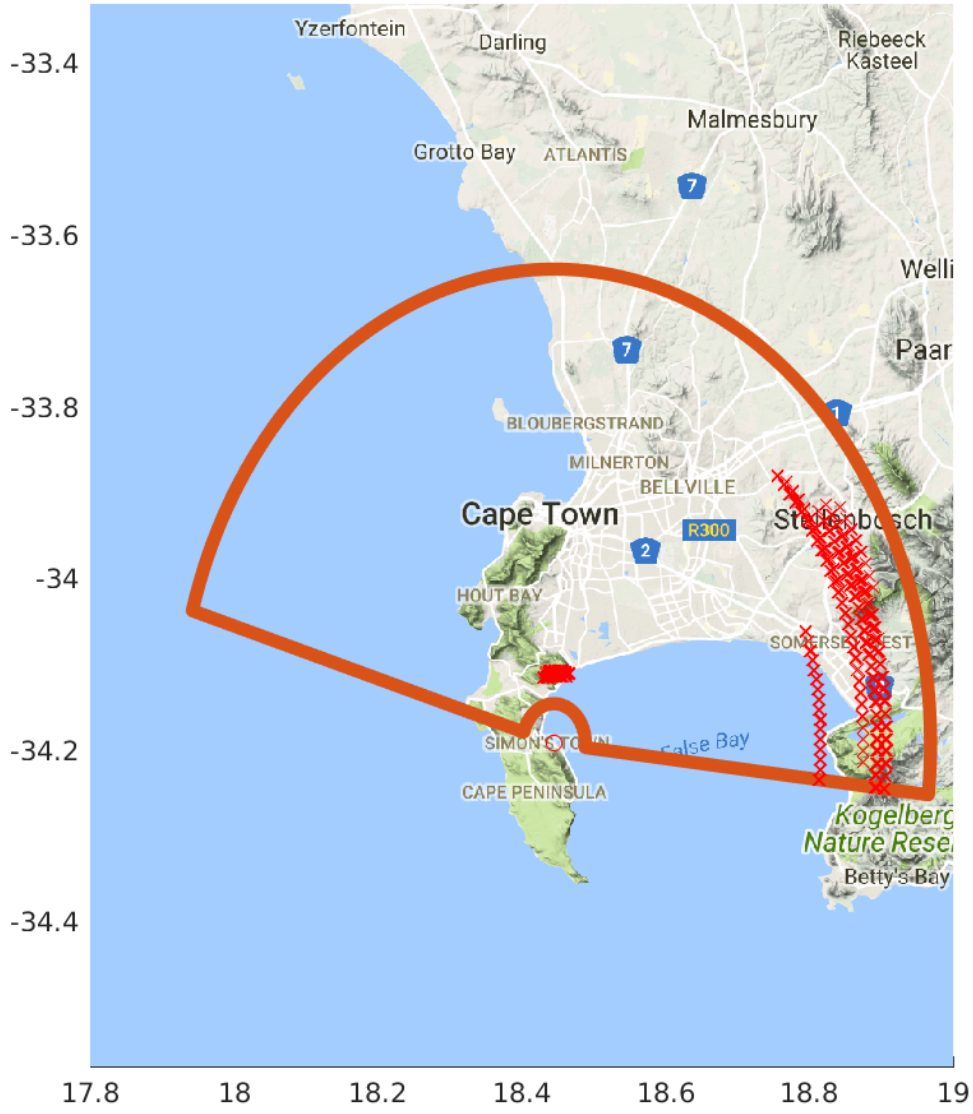

Figure 5.14: Threshold detection from Figure 5.13 overlayed with a terrain view image of Google Maps.

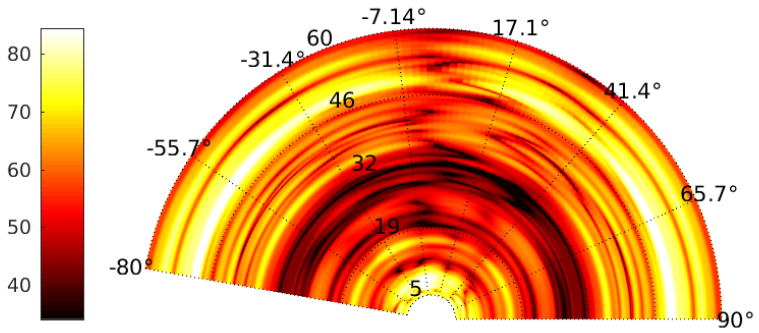

Figure 5.15: Beam steering using the method described in Section 4.5.4 for experiment "fc-20M-B-0.15M-int-100-nbuffs-40-pri-0.0005u-chirp_duration-2e-05u". Range is from 5 km to 60 km and azimuth between -80° and 90°.

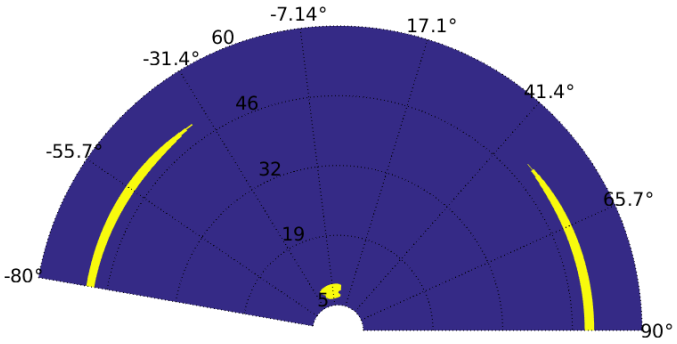

Figure 5.16: Threshold detection applied to the data in Figure 5.15.

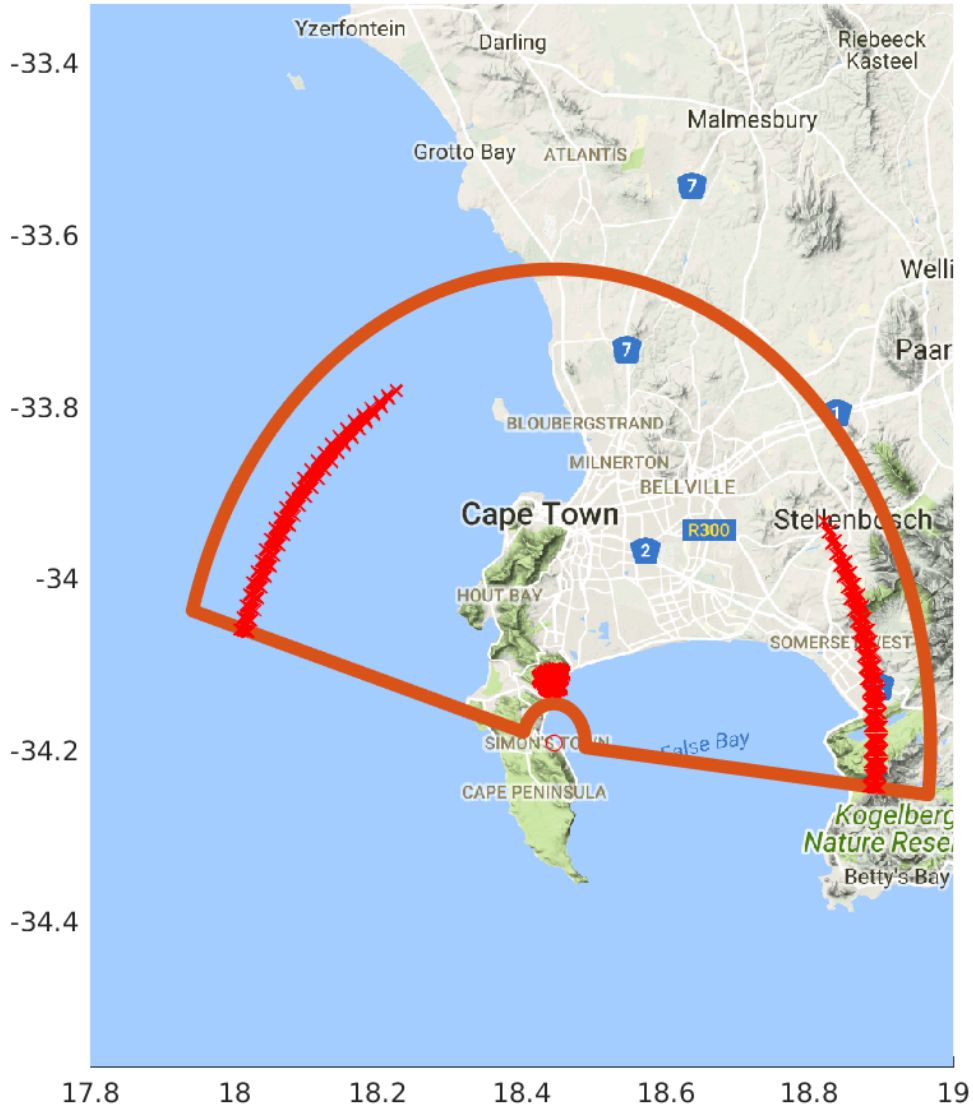

Figure 5.17: Threshold detection from Figure 5.16 overlayed with a terrain view image of Google Maps.

5.3 Bragg Scatter

The Bragg scatter phenomenon described in Section 2.2.1 was tested by changing the operating frequency between 14, 16, 18, 20, 22, and 24 MHz, using the data captured from a single element, setting the bandwidth to 2 MHz, and keeping all other operating parameters constant. These results are listed in Tables 5.3 and 5.4. The results are plotted in Figure 5.18 where the expected Bragg scatter Doppler frequencies are labelled along with the actual Doppler shifts measured. The discrepancies may be due to the fact that the range cell is the shape of an annulus and therefore encompasses land, deep sea waves, and shallow sea waves where the sea gravity wave phase velocity calculated using (2.1) no longer applies.

Figures 5.19 and 5.20 are range Doppler maps of the trials conducted at IMT on the Thursday. The Bragg scatter effect is evident in both figures as a pair of horizontal lines on opposite ends of the Doppler axis. The stationary targets discussed are also evident as the zero velocity bright spots at 8 km and between 40 and 50 km.

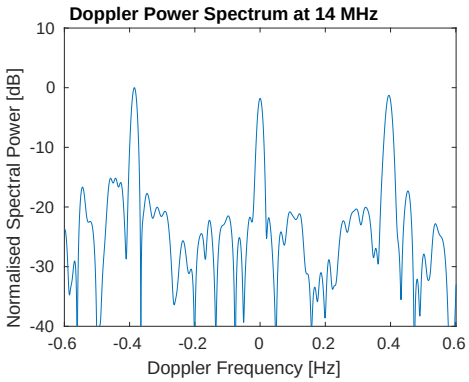

(a) Expected Bragg scatter Doppler frequency is 0.3816 Hz and actual frequency is 0.39 Hz.

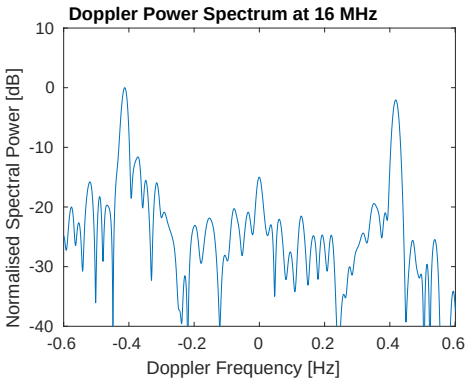

(b) Expected Bragg scatter Doppler frequency is 0.4079 Hz and actual frequency is 0.415 Hz.

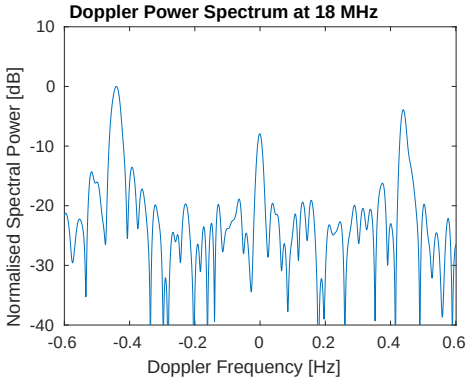

(c) Expected Bragg scatter Doppler frequency is 0.4327 Hz and actual frequency is 0.44 Hz.

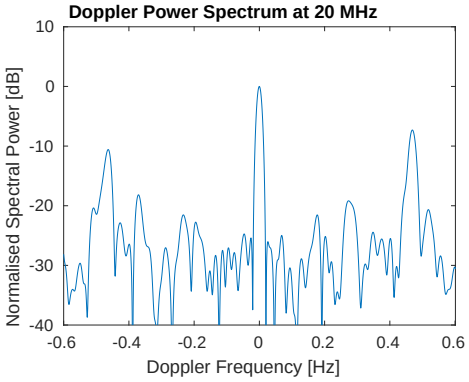

(d) Expected Bragg scatter Doppler frequency is 0.4561 Hz and actual frequency is 0.466 Hz.

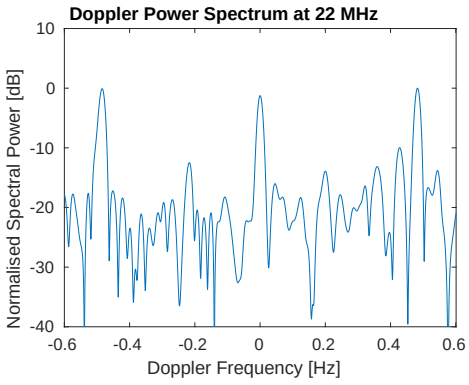

(e) Expected Bragg scatter Doppler frequency is 0.4784 Hz and actual frequency is 0.483 Hz.

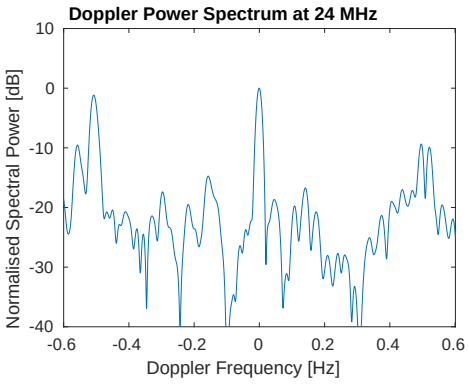

(f) Expected Bragg scatter Doppler frequency is 0.4996 Hz and actual frequency is 0.5 Hz.

Figure 5.18: Doppler frequency spectrum showing the Bragg scatter peaks for different center frequencies.

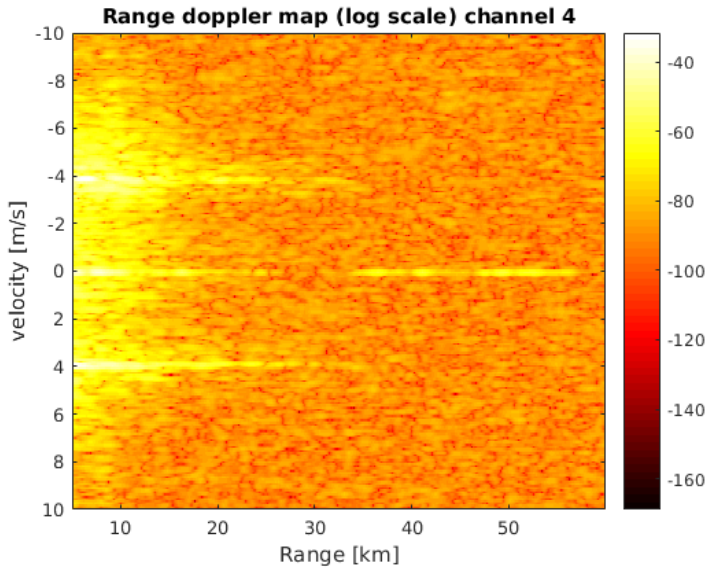

Figure 5.19: Range Doppler plot of experiment "fc-16M-B-0.15M-int-100-nbuffs-40-pri-0.0005u-chirp_duration-2e-05u". Center frequency of 16 MHz and bandwidth of 150 kHz.

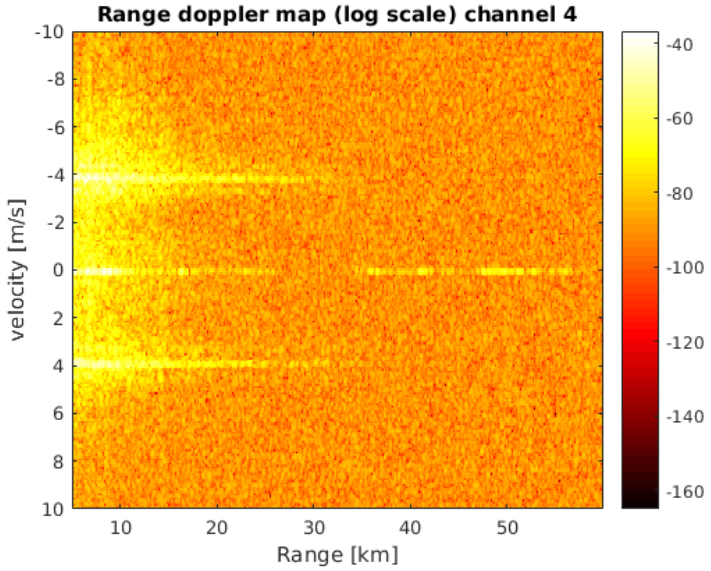

Figure 5.20: Range Doppler plot of experiment "fc-16M-B-0.5M-int-100-nbuffs-40-pri-0.0005u-chirp_duration-2e-05u". Center frequency of 16 MHz and bandwidth of 500 kHz.

Chapter 6

Conclusions and Recommendations

The aim of this project was to get a better understanding of HF radar and to determine the feasibility of constructing a low-cost HFSWR demonstrator. A complete HFSWR demonstrator now exists at UCT and a broad understanding of HFSWR concepts and techniques has been acquired. The HFSWR demonstrator can be easily set up along the coast and operated to detect large stationary targets at over the horizon ranges and detect ocean features. The project has fulfilled the objective of demonstrating feasibility. This chapter serves to outline the conclusions drawn from different aspects of the project along with many recommendations and suggested future projects.

6.1 Further Research

This section will provide recommendations for further research into existing systems and techniques. The most notable technique is that of HFSWR direction finding. Furthermore, research and simulations into ocean wave models and target RCS models are recommended as to provide an improved understanding of the sensing environment. Finally research and simulations in FMICW radar are recommended as this is a common pulsing scheme used in HF radar and may provide

improved SNR compared to the currently implemented pulse echo approach.

6.1.1 Ocean Current Mapping Using DF

This report has concentrated on beam forming for azimuth discrimination. Direction finding is introduced in Section 2.4.1 and has been used by CODAR for many years [1, 39] due to its small real estate requirements. The latest CODAR radar contains three colocated antennas as opposed to the tens or hundreds of metres required by beam steering arrays. Despite its wide use by oceanographers, there are doubts about its ability to map more complex ocean currents. It is also suggested by WERA [43] that the DF setup cannot reliably resolve second-order Bragg scatter.

The exact same hardware completed in this project can be used to test DF too by using the square topology Barrick first used before his cross loop antenna design [1]. The square array is also utilised by WERA [45]. The setup that would be used for DF is illustrated in Figure 6.1. The master node would be identical to that used in the trials shown in Chapter 5 and the two slaves in Figure 6.1 would consist of the second receiver design in Figure 4.19(b) since four of these receivers are already available.

A basic overview of the DF signal processing technique is given in Section 2.4.1 however this method must be investigated further. CODAR have implemented a DF algorithm that incorporates multiple signal classification (MUSIC) [72]. These methods should be investigated, developed and tested on the data retrieved from the proposed trial in Figure 6.1.

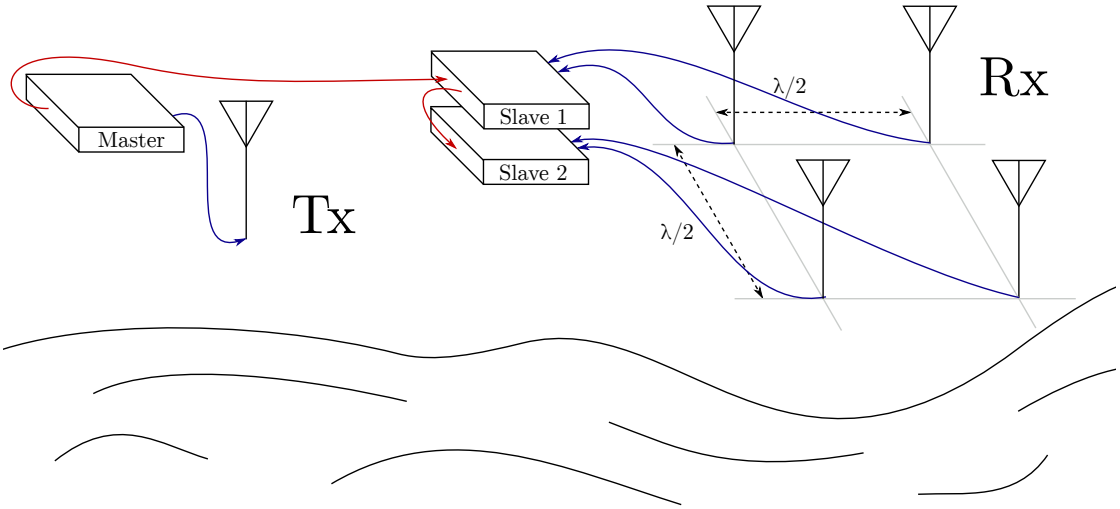

Figure 6.1: Illustration of the radar setup for Direction Finding.

6.1.2 Ocean Wave Characterisation

Ocean current mapping and other ocean wave characterisation is discussed in Section 2.2 and must be investigated further. Ocean wave characteristics are determined using the first-order and second-order Bragg scatter from the Doppler power spectrum [10, 25, 28]. The data listed in Chapter 5 has not been analysed to calculate ocean wave features however the Bragg scatter effect has been demonstrated and further work must be done to determine other ocean features. It is recommended to investigate ocean wave models such as the Neumann-Pierson spectrum, Phillipsi spectrum, Pierson-Moskowitz spectrum, and JONSWAP and to use these models to simulate radar backscatter. This will help get a better understanding of how the different ocean wave characteristics affect the second-order power Doppler spectrum and determine the effects of clutter and target detection.

The RCS of the ocean for a fully developed sea is well known [31]. This can be used to further clarify the radar performance by comparing the expected SNR results from a fully developed sea to what is measured.

Equation (3.14) is used to calculate the SNR or detection range given the target RCS and radar parameters. This equation assumes zero sea clutter which is not

the case for HF maritime radar. Adding a target in simulated ocean clutter will help test sea clutter suppression techniques [49] and to determine how far clutter reduces the SNR.

How the rough ocean waves affects path loss is discussed in [14]. A Matlab approach to generating synthetic ocean clutter along with noise and signal generation is provided by [27].

6.1.3 RCS Simulations of Maritime Targets

RCS approximations were provided in Section 2.3.2 which prove useful for radar range calculations. A more thorough review of target RCS at HF is necessary if one wishes to utilise the radar for monitoring the EEZ. A thorough review on simulating targets in the Rayleigh and Mie regions has been completed in [29, 32] and RCS modelling for HFSWR along with empirical data and interesting phenomena has been compiled by Sevgi [34]. It is recommended to evaluate the empirical results and model the RCS of targets local to South Africa as a reference for future trials.

6.1.4 FMICW

FMICW is a pulsing scheme that incorporates both pulsed radar and FMCW. A continuous wave scheme such as FMCW is impractical to implement in HF radar due to the high coupling between the transmit and receive antennas. As a compromise, the FMCW waveform may be gated on and off so that the radar is either transmitting or receiving but not both at the same time. The advantage of such a scheme is that potentially higher duty cycles can be achieved without compromising blind range resulting in higher average transmit power. It is recommended to investigate the FMICW pulsing scheme [73] and to do a comparison of existing FMICW schemes such as that implemented by the SWR-503 [74] for target detection, and that implemented by CODAR [75] for ocean current mapping.

6.2 System Improvements

The HF demonstrator described in this report is the first iteration of such a system at UCT. As such, there are many areas in which the system can be improved. Two areas in which the system can be improved significantly with minor effort are proposed. These include modifications to the current RF switch and improving the setup cabling. More long term considerations for improving the system are also listed. The radar can be made more flexible by increasing the bandwidth of the receiver and the SNR still preserved by making the bandwidth selectable. Finally, improvements on the FPGA are also listed which help incorporate other recommendations listed in this chapter. Recommendations on the antennas are provided in Section 6.3.

6.2.1 Short Term Improvements

Improve Current RF Switch Speeds

The RF switch described in Section 4.3.2 has long turn on and turn off times due to the slew rate of the operational amplifier (opamp). These can be fixed simply by replacing the dual LM358 opamps currently employed with opamps that have a higher slew rate. Besides the opamp, the other limiting factor affecting the turn on and turn off times are the LC lines between the Ctrl lines and ground in Figure 4.27. The time constant of this LC circuit is 0.2 µs, which is well below the 8.7 µs and 29.6 µs turn on and turn off times currently experienced.

Reduce Cabling Setup Time

It was quickly discovered during the trials that a distributed setup containing multiple nodes separated metres apart is cumbersome and difficult to maintain. Antenna elements were approximately 8 m apart and each node was placed approximately 16 m apart from each other. The RG58 cables used on receive are 10 m long and the synchronisation cables were about 20 m long. The variety of cables required between the nodes (including power cables) and their limited length

made setting up challenging. It is recommended to either make each element its own node, reducing the dependence on coaxial cables, or to keep all the receive nodes together and to use long coaxial cables to the receive antennas. With the latter option, two suboptions are available. Either all the coaxial cables must be kept the same length and therefore all the coaxial cables are the length of the furthest antenna from the receivers, or the coaxial cable to each antenna can vary by the antenna's distance from the receiver and the signal propagation delay error between each element be corrected prior to post processing.

6.2.2 RF Frontend Operating Frequency Extension

The choice on the operating frequency design was based on two limitations. The first limitation was the conical antenna design which operates between 13.6 MHz and 25.5 MHz. The second limitation was the sampling frequency of the RP after decimation which is 25 MHz. The RP has a built in 60 MHz anti-aliasing low-pass filter which means a signal between 12.5 MHz and 25 MHz may be sensed by the RP in the second Nyquist zone. The RP itself can measure a signal in the first Nyquist zone of less than 12.5 MHz however the conical antenna is not well matched below 13.6 MHz.

It is recommended to design an antenna that is well matched at frequencies closer to 3 MHz. This recommendation is further detailed in Section 6.3. Assuming that an antenna with a lower operating frequency is available, it is recommended to alter the RF receiver to accept lower frequencies too. The first receiver design in Figure 4.19(a) contains the BG2 which has a lower cutoff frequency of approximately 12 MHz and is therefore recommended to not use the first receiver design in Figure 4.19(a).

The RF switch has high insertion loss at lower frequencies (see Figure 4.29) however external noise is also higher at lower frequencies and so the higher insertion loss may not be an issue. The band-pass filter used in the demonstrator was designed to only pass through signals in the second Nyquist zone and must therefore be redesigned to pass through both Nyquist zones. Alternatively, multiple band-pass filters may be designed with different cutoff frequencies and a mechanical relay

circuit can be constructed that allows the operator to change between the different band-pass filters. For example one filter can be designed with a pass band between 3 MHz and 12.5 MHz, and the other between 12.5 MHz and 25 MHz. The pass band can be broken up into as many divisions as the designer wishes, noting that a smaller bandwidth reduces the range resolution however also reduces the amount of external noise. With regards to the LNA, it is important to note that external noise is greater at lower frequences and must be taken into account when selecting the gain to ensure there is no saturation on the ADC.

6.2.3 FPGA Work

The digital implementation on the RP as described in Section 4.1 worked as expected. A few of the issues identified will be discussed along with other improvements to make the RP compatible with future radar changes.

Extending the PRI

The integrator implemented in the FPGA involves a First In First Out (FIFO) buffer where every sample in the range line is stored. This FIFO buffer needed to be the same size as a single range line and was limited to 500 µs (or 75 km in range) due to the limited resources available on the FPGA. This limited the PRI to 500 µs which is less than the usual 1 ms to 2 ms of other HFSWRs. The available 75 km of range recorded can not be increased unless the current FPGA implementation is made more compact so that more of the FPGA resources can be allocated to the range line FIFO buffer. Another option is to not start recording immediately at the beginning of the PRI but to have a recording delay at the beginning of the PRI and to have another delay between the end of the recording and before the PRI is over.

Implement FMICW Radar

The digital implementation on the RP works in a pulsing scheme however FMCW can technically be achieved by reducing the PRI to the pulse length. The maximum pulse length however is limited to 30 µs due to the transmit buffer size in the

firmware. The transmit buffer size will likely need to be increased to a complete range line worth of samples, which is not feasable. Alternatively, the FMCW waveform can be synthesized by the FPGA directly based on given parameters. These parameters include start and stop frequency and sweep repitition interval. For the case of FMICW radar, extra parameters required include gating period and transmit time (or duty cycle).

Preprocess Beam Steering

Each receive node has an SDR attached to two elements which performs data preprocessing before storing the data. Beam steering can be implemented on each pair of elements to either point straight ahead or at a particular angle of interest. By doing this, the total amount of captured data is reduced to a half. This technique was done by the SWR-503 [74].

In post processing, each receive node would be considered an individual antenna with a new beam pattern. The resultant beam pattern of the entire array will be the beam pattern of the antenna pair with the Array Factor.

6.3 Antennas

The different antennas considered in this project are shown in Section 4.4. The conical antenna has a deep broad reflection coefficient making it ideal for transmit, however the antenna takes time to set up and is not matched below 13.6 MHz. It is apparent that one can not solve one problem without exacerbating another. An antenna with a lower operating frequency will be bigger and therefore will be more difficult to set up. A smaller antenna with a lower operating frequency will have a poor beam pattern (possibly causing more ionospheric clutter) and may also have a poor bandwidth. A couple different options for transmit and receive antennas are discussed.

6.3.1 Transmit

Some different HFSWRs started off using a vertically polarised log periodic monopole antenna on transmit [49, 76]. These antennas have the advantage of being broadband, well matched and have a directional beam pattern. The drawback of such an antenna is the amount of space required and the time it takes to set up, hence why it was not considered in this report. It may be considered for more permanent installations. The WERA transmit antenna illustrated in Figure 2.11 may be a better option than the log periodic monopole antenna.

6.3.2 Receive

The 2 m long monopole antennas proved to be successful on receive. These antennas were cheap and easy to make and their setup time is low. If the RF receiver is to be modified for frequencies lower than 12.5 MHz, it is recommended to construct longer monopole antennas of 2.5 m tall or higher. This is to ensure that less ionospheric clutter is absorbed and to ensure higher efficiencies at lower frequencies.

The matching circuit for the monopole consisted of a tunable inductor using a ferrite rod to cancel out with the capacitance of the electrically small monopole. This proved useful since the matching circuit was easy to make and the center frequency was adjustable between 12.5 MHz and 25 MHz. The ferrite material is from an unknown source however and it is unsure how similar the properties are between each ferrite rod. It is recommended to redesign the matching circuit to consist of multiple air core inductors selectable by mechanical relay switches and controllable by the RP. This will make tuning the antennas far quicker and easier since it can be done remotely using a computer, and will ensure that every identical antenna has an identical matching circuit. The matching circuits may have a more complex design than a simple series inductor.

Little effort was spent on the electrically small loop antenna in Section 4.4 since the drawback of very narrow bandwidth was immediately spotted. It is worth investigating the small loop antenna further since some of the drawbacks can be

mitigated, such as the unstable resonance. The loop antenna may also prove useful for DF if recommended trials in Section 6.1.1 are successful.

6.3.3 Truly Monostatic Operation

Preliminary work on an RF switch with higher power handling capabilities and faster switching speeds has been completed by [77] with the purpose of using each antenna for both transmit and receive and to implement FMICW (discussed in Section 6.1.4). Using each antenna for transmit provides the flexibility of beam steering on transmit which improves the overall transmit gain and can reduce clutter from unwanted directions. There is also the added benefit of having truly identical equipment for every antenna which makes scaling up the radar easier. The complete RF and digital electronics can be kept local to each antenna. It is recommended to pursue using each element for both transmit and receive (truly monostatic) with either the simple monopole antennas or conical antennas as the elements, as opposed to using a separate transmit antenna. Further details are provided in Section 6.1.4.

Appendix A

Class E Amplifier

This appendix serves to present the work done on developing a Class E amplifier. It was originally proposed to develop an amplifier in the hopes to prevent the lead times to retrieve the amplifier in Section 4.2. Although developing the class E amplifier proved successful, the amplifier had a narrow operating frequency and changing the operating frequency also meant adjusting the class E amplifier. The achieved output power was in the order of tens of watts which is not enough for the current pulsed radar setup.

The drawbacks listed are by no means unsolveable. The poor bandwidth is due to the required phase of the load network (as will be explained) and can be solved by using a more broadband topology. The output power can also be improved by using better transistors however the power limitation may not be a problem in the future if a truly monostatic mode of operation is achieved (each element is used for both transmit and receive).

An overview of a class E amplifier is shown in Figure A.1 which consists of a voltage controlled switch and a passive load network. The advantage of a class E amplifier is its low parts count and its high efficiency. A class E amplifier doesn't have a gain but rather provides a constant output power which limits the applications of the class E amplifier, however this topology will work for amplifying a frequency modulated signal. The output power is controlled by changing the DC supply

voltage (designated V_{DC}).

The load network in Figure A.1 must be designed so that the impedance looking into the network is inductive at the operating frequency with a phase of 49° required for idealized class E operation (further details of an idealized class E amplifier along with solutions can be found in [78]) and must act as a low-pass filter to suppress the switching harmonics. This is typically achieved for a resistive load using a series inductor and capacitor [79]. The amplifier for the demonstrator must be broadband and therefore the impedance looking into the load network must have a phase of 49° over the full frequency range, ideally from 3 MHz to 30 MHz.

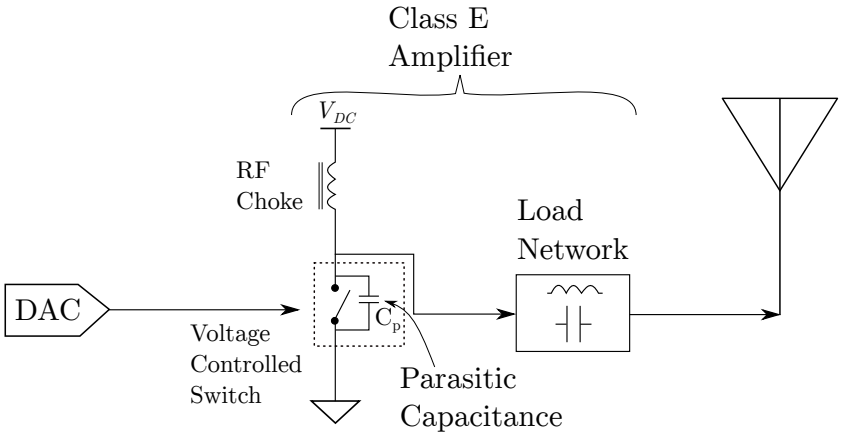

Figure A.1: Generalised class E amplifier diagram.

Details regarding the operation of class E amplifiers are provided in [79, 80] and the design equations are reproduced below:

- Output power: $P_o = \frac{V_{DC}^2}{R_{DC}}$
- Equivalent DC resistance: $R_{DC} = 1.73R$
- Shunt susceptance: $B = \omega C = \frac{1}{5.4466R}$
- Load angle: $\psi = 49.052°$
- Load-network impedance: $Z = R + jX = R + j1.152R$

- Peak switch voltage: $V_{smax} = 3.56V_{DC}$
- Peak switch current: $i_{smax} = 2.84I_{DC}$

The load network in Figure A.1 is expanded in Figure A.3. Capacitor C_T transforms the load resistance down and C_P is the parasitic capacitance present across the switch. The remainder of the load network has a low pass topology and provides two tunable variables (C_{V1} and C_{V2}).

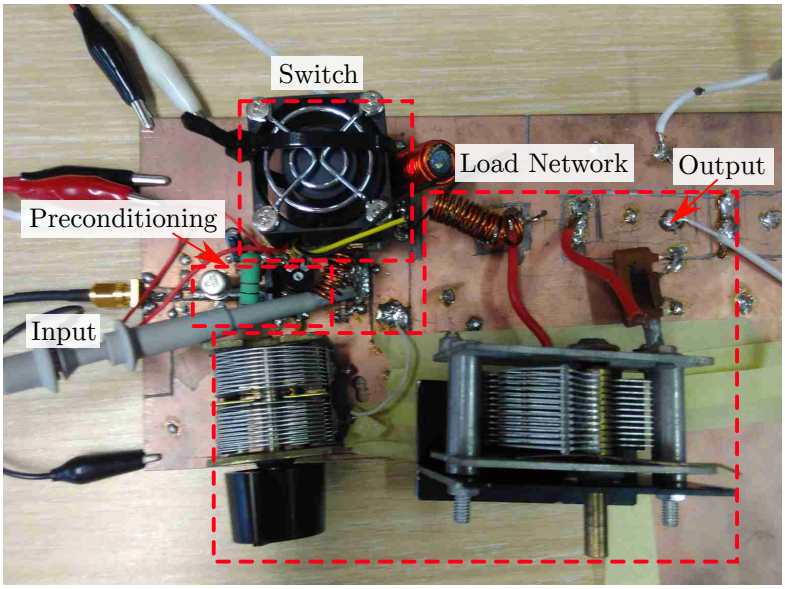

Figure A.2: Picture of the HF class E amplifier during development.

The complete amplifier circuit is shown in Figure A.4 which conprises of a class A stage amplifier, class B stage amplifier, DC offset, and an N-type MOSFET switch. The MOSFET switch consists of two IRF610 in parallel which has a combined gate capacitance of 280 pF. Driving the gate of the MOSFET requires a source with a close to zero output impedance since the capacitive Gate impedance decreases with frequency. The MOSFET is therefore driven by a class B push-pull amplifier which has a low output impedance. The class B stage has no biasing since it is not designed to be linear. No crossover distortion is expected at the class B stage since it is driven by a square wave generated by the class A stage. The class A stage is used to convert the incoming 2 V_{pp} frequency modulated signal from the

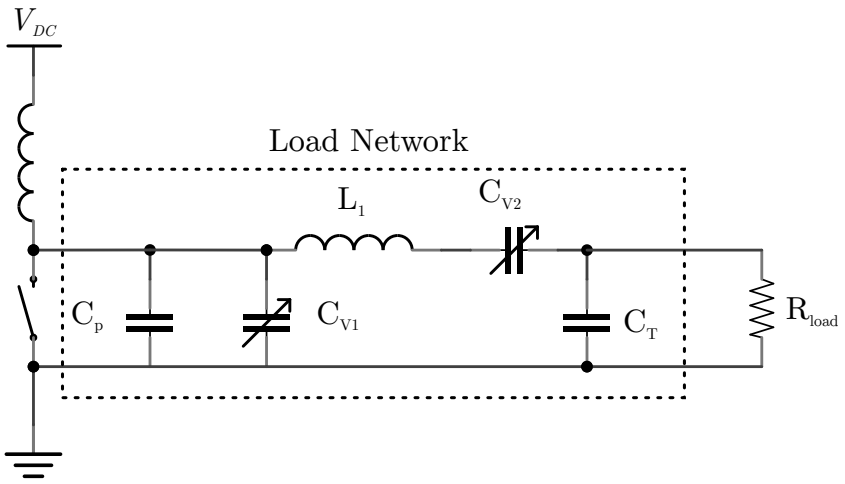

Figure A.3: Load network diagram of currently implemented class E amplifier pictured in Figure A.2.

Red Pitaya into a 12 V_{pp} square wave signal which can drive the MOSFET fully into saturation.

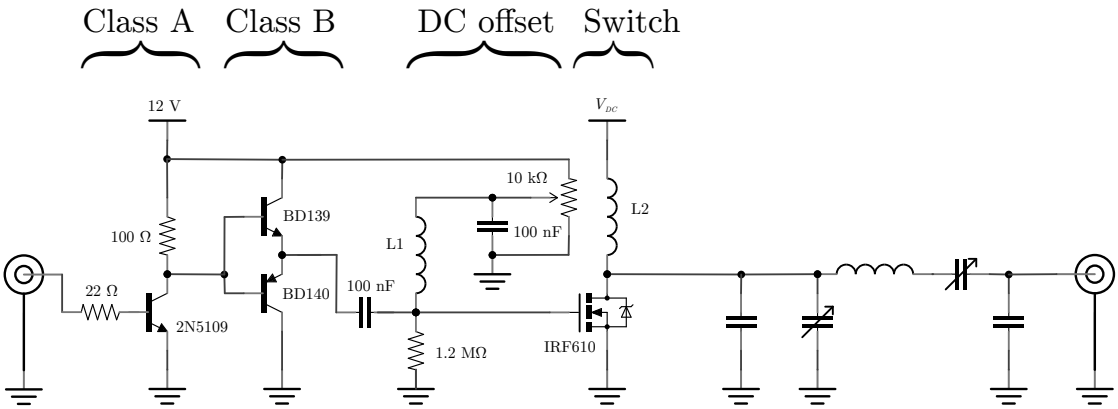

Figure A.4: Complete amplifier circuit consisting of class A and class B amplifiers, DC offset circuit, and the class E amplifier consisting of a switching circuit and load network. Note that two IRF610 transistors are attached in parallel to increase the total drain current.

A proposed broadband load network circuit by [81] is shown in Fig. A.5 which promises to provide a 35 % fractional bandwidth. The software package Microwave Office can be used to design the load network for the class E amplifier. Microwave Office allows the user to set component values as variables and to set optimization

goals. An optimiser then determines the best possible combination of component values to meet these goals. If the optimizer is not able to meet the optimization goals sufficiently, the broadband network can be extended by including more series inductors and shunt capacitors.

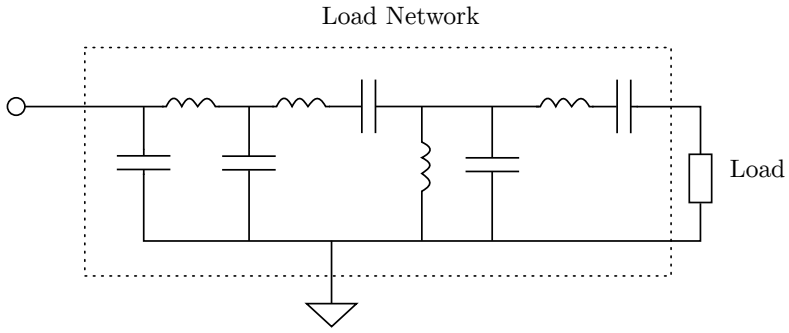

Figure A.5: Broadband load network suggested by [81].

A class E amplifier designed to operate at 20 MHz for a 50 Ω load was constructed and tested. Tests were conducted using a signal generator, MSO9104A oscilloscope, and a 40 dB 100 W coaxial attenuator. The DC power supply was set to 12 V for the class A and B stages and 31 V (maximum voltage supplied by the bench power supply) for the class E stage. The signal generator was set to 16 MHz and 2 V_{pp}. One of the oscilloscope's standard probes was attached to the drains of the transistors. The output of the amplifier was attached to the oscilloscope via 50 Ω coaxial cable and the 40 dB attenuator and the oscilloscope port was set to 50 Ω input impedance. Figure A.6 is the voltage waveform of the drain of the MOSFET transistors. Figure A.7 is the output voltage of the amplifier after 40 dB of attenuation and Figure A.8 is the output signal plotted in the frequency domain. The output power of the tested class E amplifier is 44.62 dBm (28.97 W) and the second harmonic at 32 MHz in Figure A.8 is 23.8 dB below the fundamental which is 4.647 dBm.

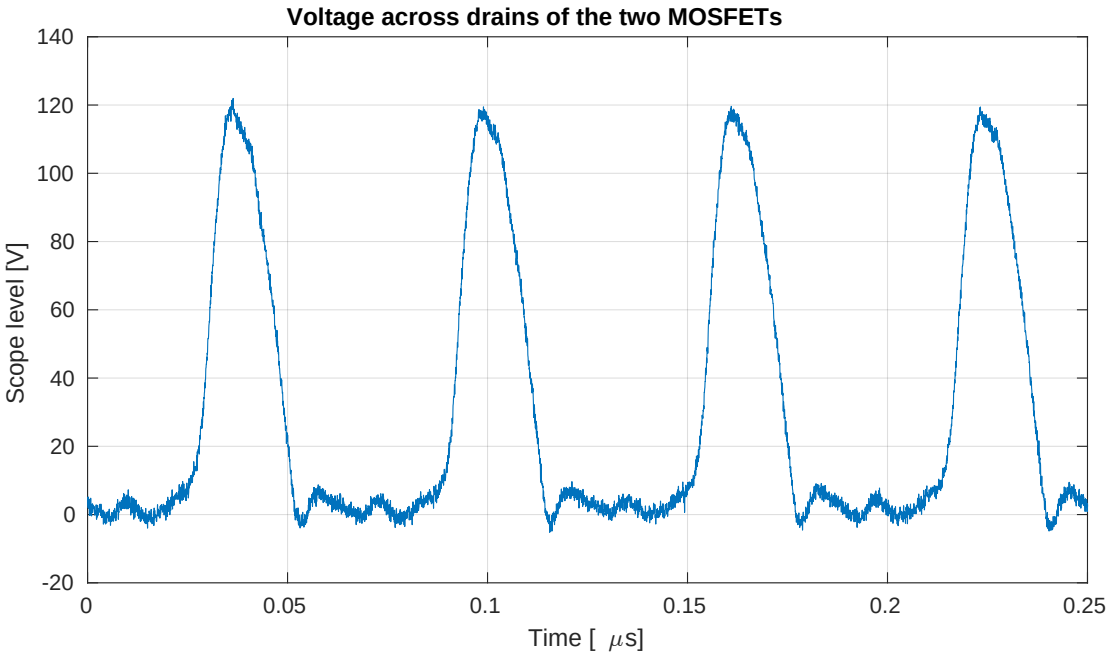

Figure A.6: Voltage waveform as seen from the drain of the N-channel MOSFET in Figure A.4.

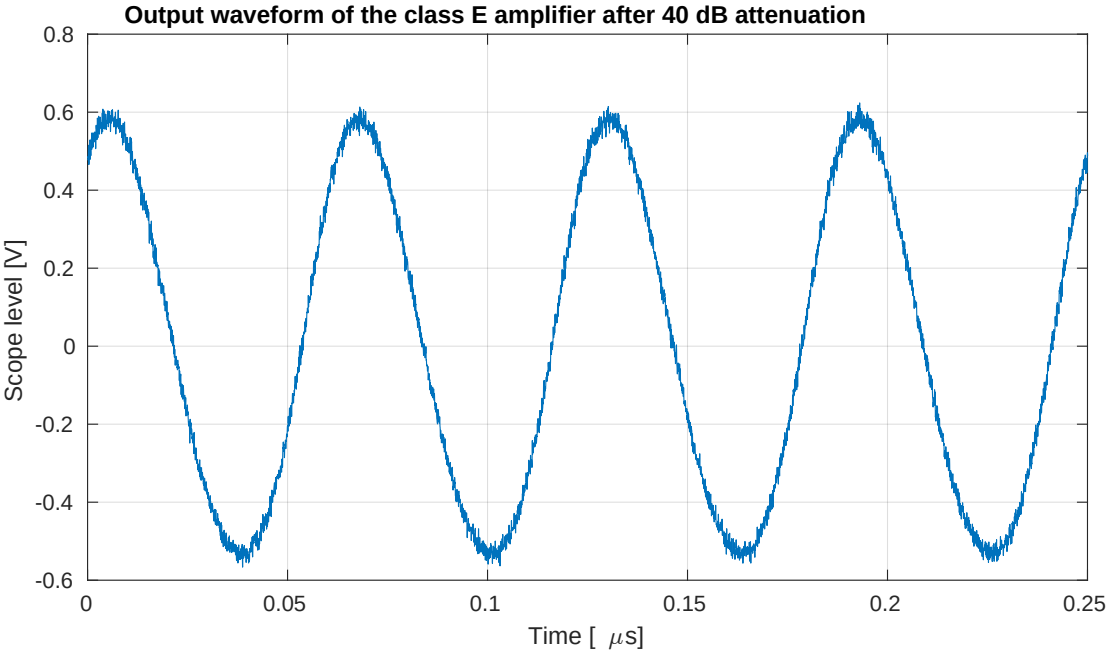

Figure A.7: Output voltage waveform of the class E amplifier across a 50 Ω load after being attenuated by 40 dB.

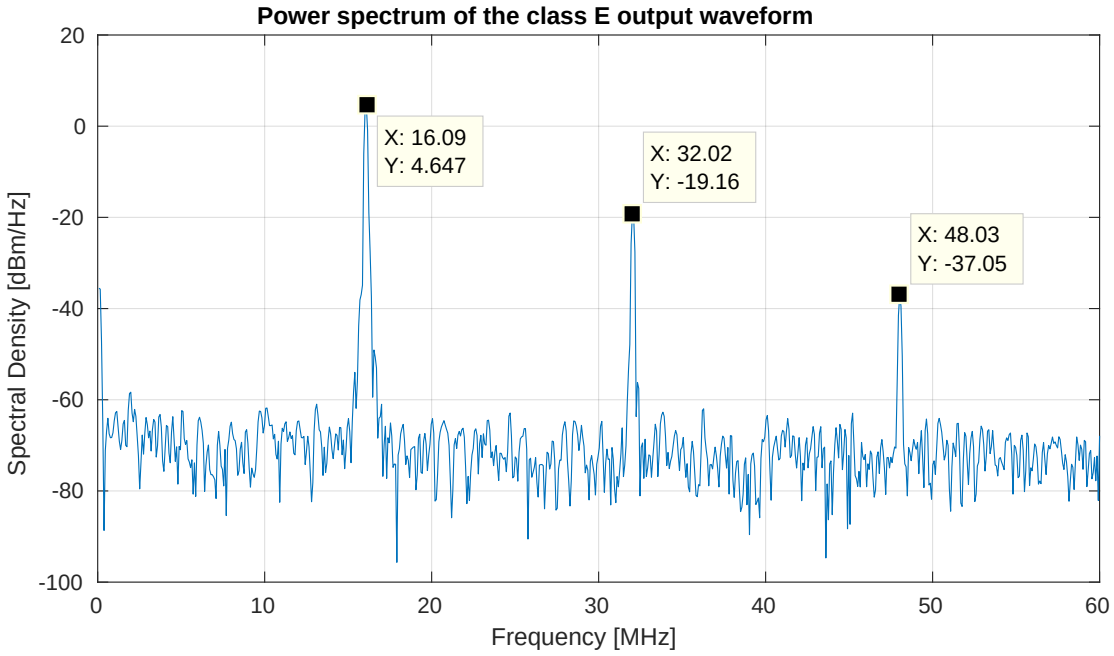

Figure A.8: Power spectral density of the class E amplifier absorbed by the 50 Ω load after being attenuated by 40 dB.

Appendix B

Beam Steer Reference Figures

The receive array used during the trials consisted of six elements spaced at approximately 8 m apart. This appendix serves as a reference of the expected overhead array factor (AF) for the receiver array at different steer angles and operating frequencies. The AF assumes isotropic antennas for the elements however the actual elements consist of monopole antennas which have a uniform horizontal beam pattern.

The AF was calculated using (4.8) and (4.9) [71]. The array sits along the horizontal axis and the steer angle is measured from this axis. The beam steer direction is indicated with green lines and nulls are indicated with red lines. The 3 dB beamwidths are measured from the plots.

A linear array with element spacing d must satisfy the requirement

$$d < \frac{\lambda}{2} \tag{B.1}$$

to avoid grating lobes at look angles close to the end fire direction. The wavelengths at different operating frequencies are listed in Table B.1 where it can be seen that (B.1) isn't met at frequencies above 18 MHz. The requirement can be met at these frequencies by simply reducing the element spacing d or the operator may choose to only use the look angles where grating lobes are suppressed (close to broadside).

Table B.1: Different operating frequencies and their equivalnet wavelength and half wavelength.

f_c [MHz]	λ_c [m]	$\frac{\lambda_c}{2}$ [m]
14	21.43	10.71
16	18.75	9.38
18	16.67	8.33
20	15.00	7.50
22	13.64	6.82
24	12.50	6.25

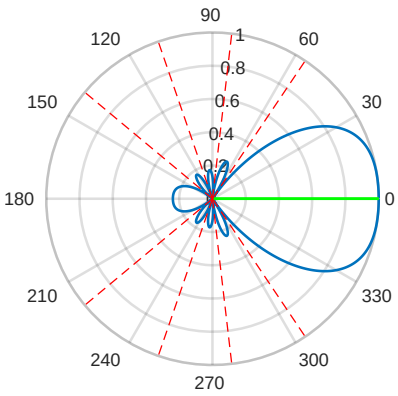

(a) Beam steered 0° from array axis. Beam width = 86.132°.

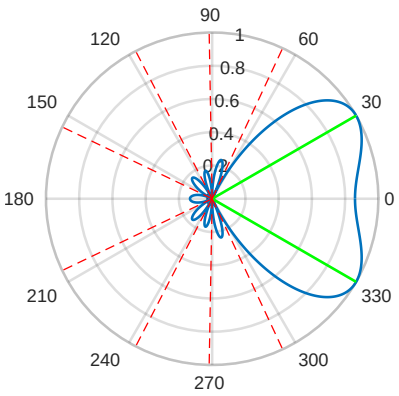

(b) Beam steered 30° from array axis. Beam width = 106.748°.

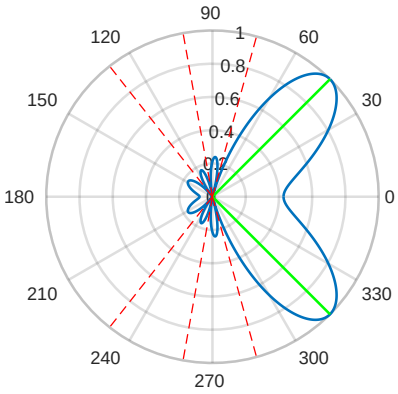

(c) Beam steered 45° from array axis. Beam width = 51.61°.

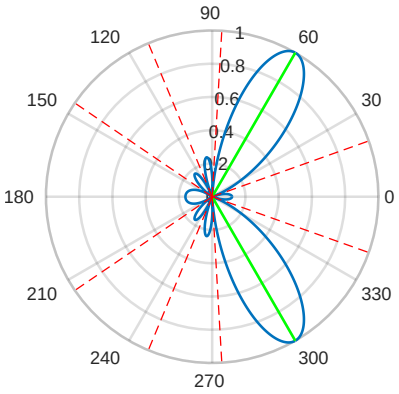

(d) Beam steered 60° from array axis. Beam width = 36.973°.

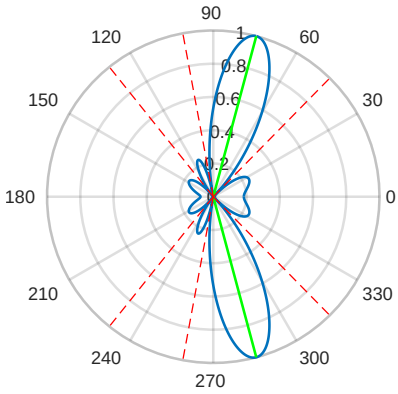

(e) Beam steered 75° from array axis. Beam width = 32.496°.

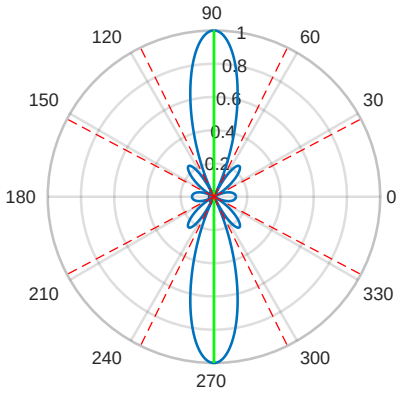

(f) Beam steered 90° from array axis. Beam width = 31.262°.

Figure B.1: Beam steer of 6 element array at 8.08 m element spacing with an operating frequency of 14 MHz.

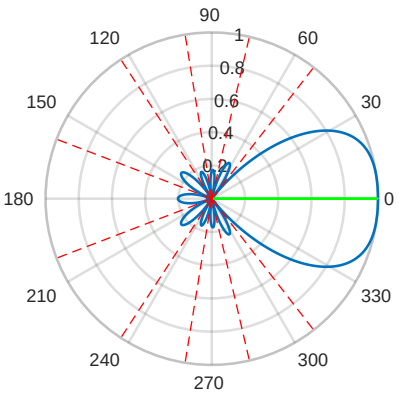

(a) Beam steered 0° from array axis. Beam width = 80.32°.

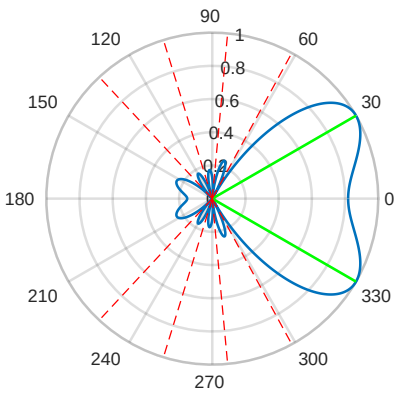

(b) Beam steered 30° from array axis. Beam width = 101.86°.

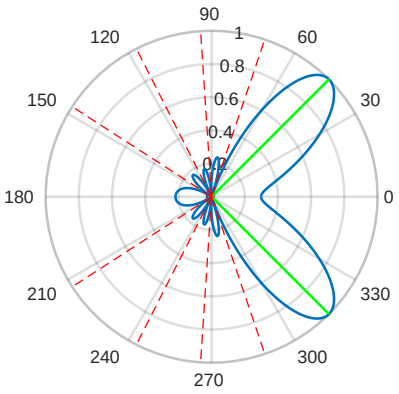

(c) Beam steered 45° from array axis. Beam width = 42.416°.

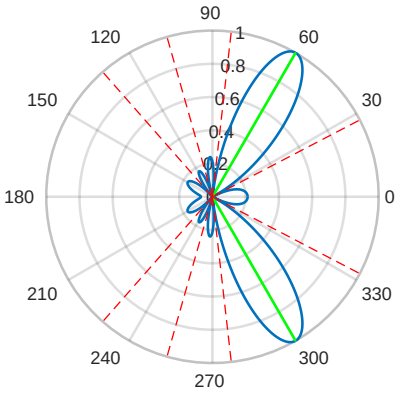

(d) Beam steered 60° from array axis. Beam width = 32.049°.

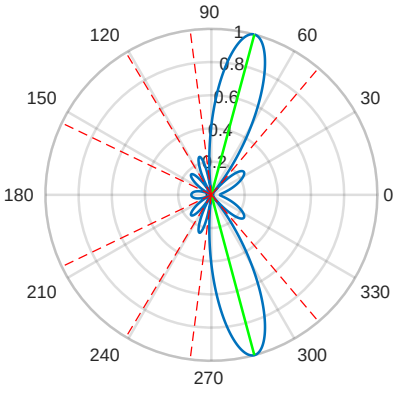

(e) Beam steered 75° from array axis. Beam width = 28.32°.

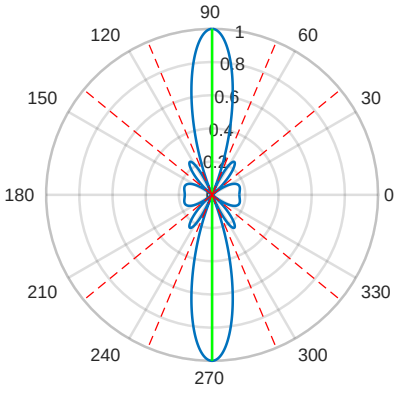

(f) Beam steered 90° from array axis. Beam width = 27.272°.

Figure B.2: Beam steer of 6 element array at 8.08 m element spacing with an operating frequency of 16 MHz.

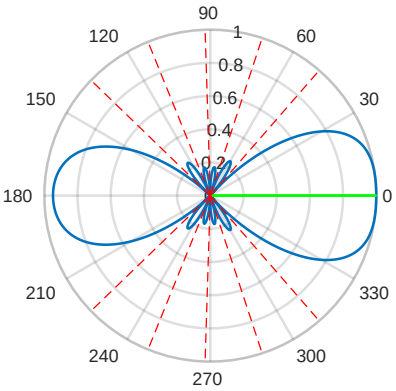

(a) Beam steered 0° from array axis. Beam width = 75.546°.

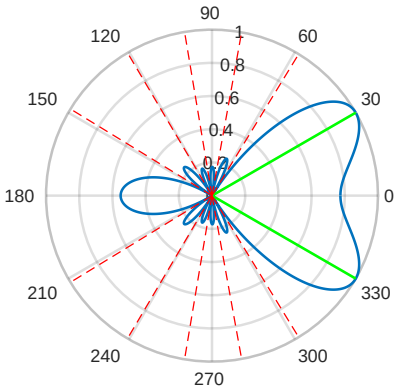

(b) Beam steered 30° from array axis. Beam width = 97.938°.

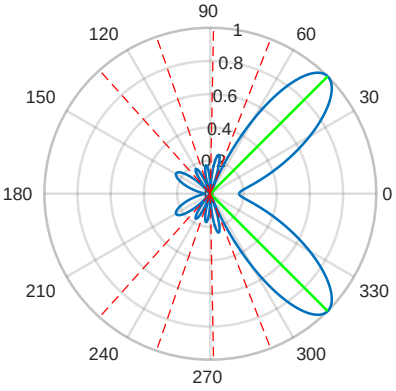

(c) Beam steered 45° from array axis. Beam width = 36.606°.

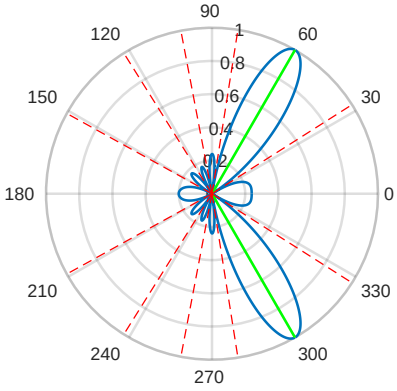

(d) Beam steered 60° from array axis. Beam width = 28.315°.

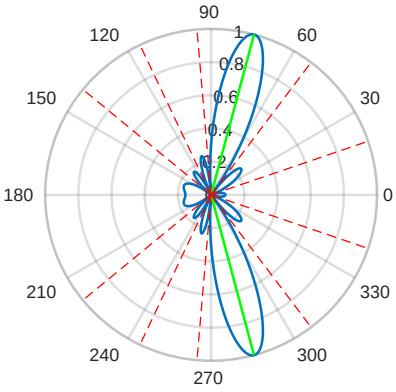

(e) Beam steered 75° from array axis. Beam width = 25.106°.

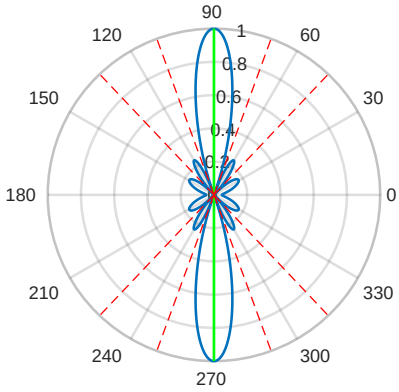

(f) Beam steered 90° from array axis. Beam width = 24.194°.

Figure B.3: Beam steer of 6 element array at 8.08 m element spacing with an operating frequency of 18 MHz.

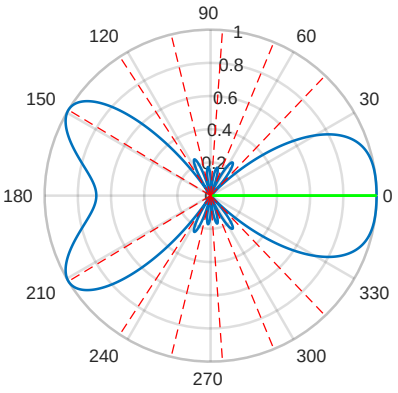

(a) Beam steered 0° from array axis. Beam width = 71.536°.

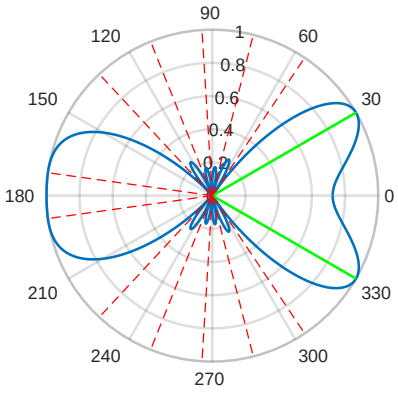

(b) Beam steered 30° from array axis. Beam width = 94.716°.

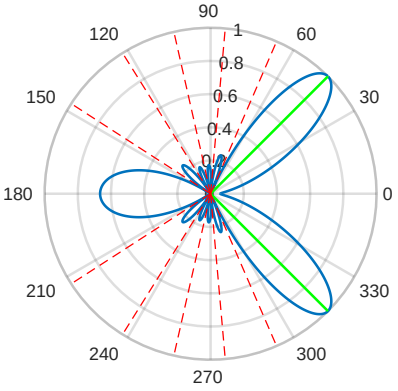

(c) Beam steered 45° from array axis. Beam width = 32.368°.

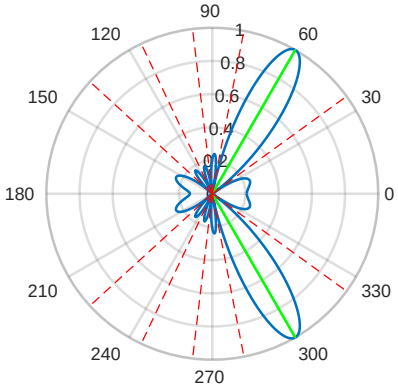

(d) Beam steered 60° from array axis. Beam width = 25.377°.

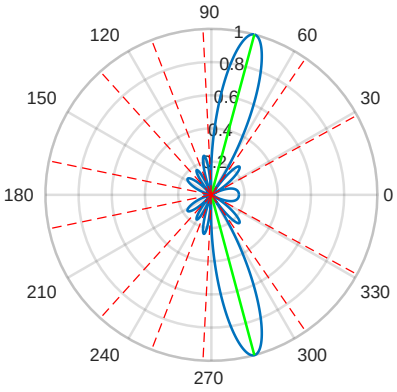

(e) Beam steered 75° from array axis. Beam width = 22.553°.

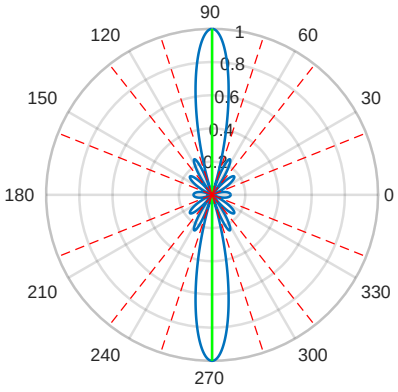

(f) Beam steered 90° from array axis. Beam width = 21.742°.

Figure B.4: Beam steer of 6 element array at 8.08 m element spacing with an operating frequency of 20 MHz.

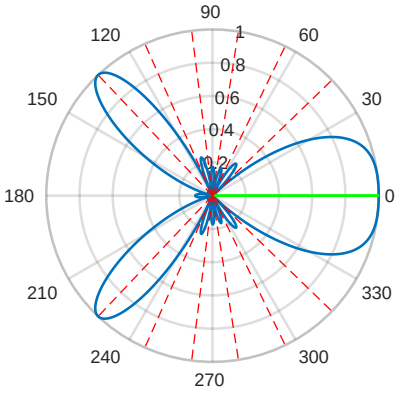

(a) Beam steered 0° from array axis. Beam width = 68.102°.

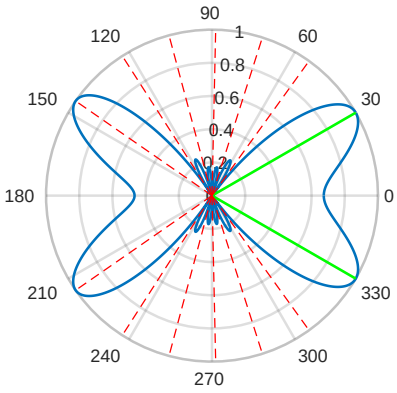

(b) Beam steered 30° from array axis. Beam width = 92.014°.

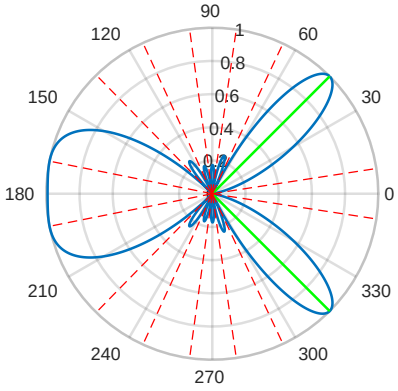

(c) Beam steered 45° from array axis. Beam width = 29.082°.

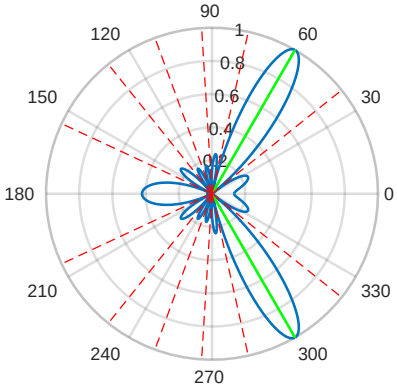

(d) Beam steered 60° from array axis. Beam width = 23°.

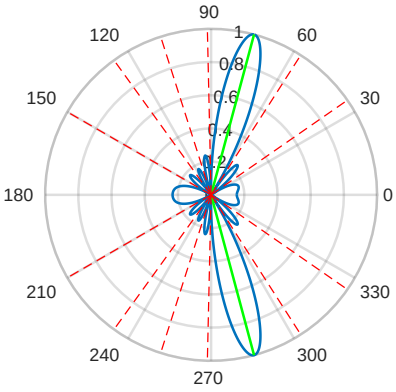

(e) Beam steered 75° from array axis. Beam width = 20.473°.

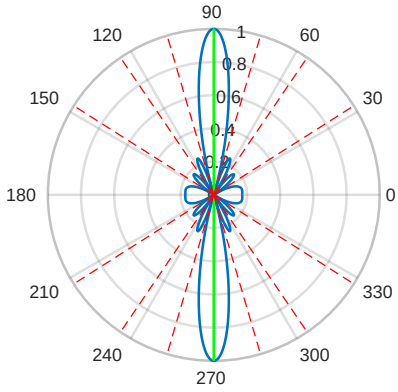

(f) Beam steered 90° from array axis. Beam width = 19.746°.

Figure B.5: Beam steer of 6 element array at 8.08 m element spacing with an operating frequency of 22 MHz.

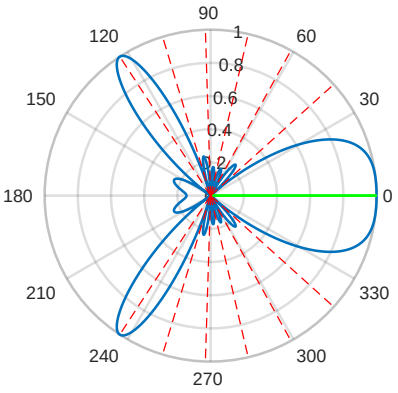

(a) Beam steered 0° from array axis. Beam width = 65.12°.

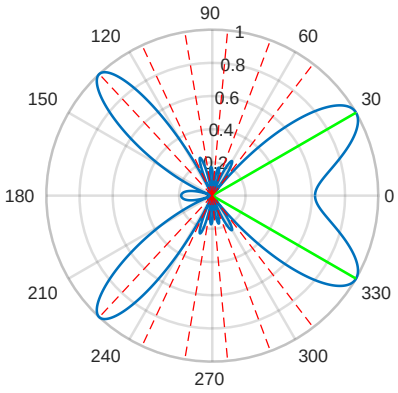

(b) Beam steered 30° from array axis. Beam width = 89.716°.

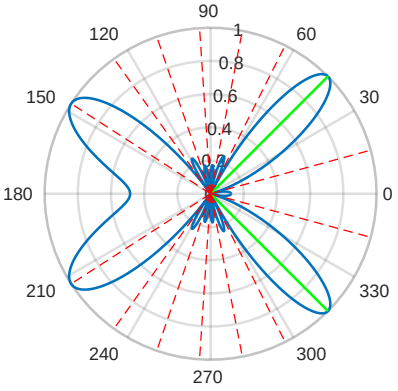

(c) Beam steered 45° from array axis. Beam width = 26.437°.

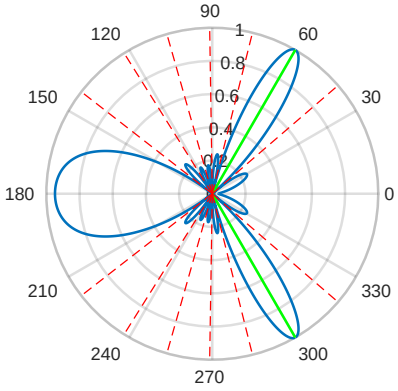

(d) Beam steered 60° from array axis. Beam width = 21.035°.

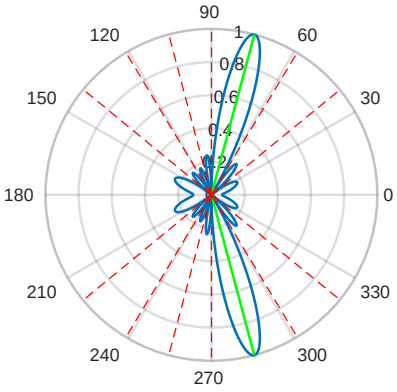

(e) Beam steered 75° from array axis. Beam width = 18.748°.

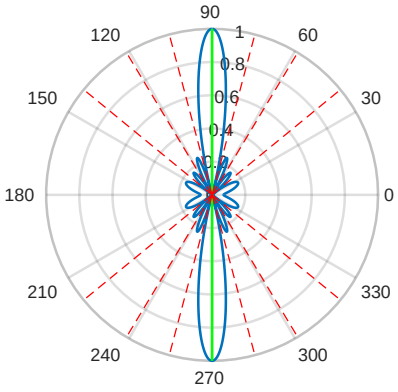

(f) Beam steered 90° from array axis. Beam width = 18.086°.

Figure B.6: Beam steer of 6 element array at 8.08 m element spacing with an operating frequency of 24 MHz.

Bibliography

[1] D. Barrick, "30 years of cmtc and codar," in *Current Measurement Technology, 2008. CMTC 2008. IEEE/OES 9th Working Conference on*, pp. 131–136, IEEE, 2008.

[2] L. M. Beal, W. P. De Ruijter, A. Biastoch, R. Zahn, *et al.*, "On the role of the agulhas system in ocean circulation and climate," *Nature*, vol. 472, no. 7344, pp. 429–436, 2011.

[3] P. L. Richardson, "Agulhas leakage into the atlantic estimated with subsurface floats and surface drifters," *Deep Sea Research Part I: Oceanographic Research Papers*, vol. 54, no. 8, pp. 1361–1389, 2007.

[4] Department of Environmental Affairs and Tourism, Republic of South Africa, "Fifteen years: a review of the department of environmental affairs and tourism," tech. rep., 2009.

[5] A. Ponsford, I. A. D'Souza, and T. Kirubarajan, "Surveillance of the 200 nautical mile EEZ using HFSWR in association with a spaced-based AIS interceptor," in *Technologies for Homeland Security, 2009. HST'09. IEEE Conference on*, pp. 87–92, IEEE, 2009.

[6] J. Eaves and E. Reedy, *Principles of modern radar*. Springer Science & Business Media, 2012.

[7] CCIR Rec., "Ground-wave propagation curves for frequencies between 10 kHz and 30 MHz," Recommendation 368-7, International Telecommunication Union, Geneva, 1992.

[8] T. Barris, "SANAE IV interferometric calibration," Master's thesis, University of Cape Town, 2017.

[9] Z. Patel, "The design and build of an antenna for high frequency surface wave radar," Bachelor's thesis, University of Cape Town, 2016.

[10] E. Shearman, "Propagation and scattering in MF/HF groundwave radar," in *IEE Proceedings F (Communications, Radar and Signal Processing)*, vol. 130, pp. 579–590, IET, 1983.

[11] G. Fabrizio, *High frequency over-the-horizon radar: fundamental principles, signal processing, and practical applications*. McGraw Hill Professional, 2013.

[12] H. Hertz and W. T. B. Kelvin, *Electric waves*. Macmillan London, 1893.

[13] A. Sommerfeld, "Propagation of waves in wireless telegraphy," *Ann. Phys*, vol. 28, no. 3, pp. 665–736, 1909.

[14] D. E. Barrick, "Theory of ground-wave propagation across a rough sea at dekameter wavelengths," tech. rep., DTIC Document, 1970.

[15] G. Goubau, "Waves on interfaces," *IRE Transactions on Antennas and Propagation*, vol. 7, no. 5, pp. 140–146, 1959.

[16] J. R. Wait, "The ancient and modern history of em ground-wave propagation," *IEEE Antennas and Propagation Magazine*, vol. 40, no. 5, pp. 7–24, 1998.

[17] K. Norton, "The propagation of radio waves over the surface of the earth and in the upper atmosphere," *Proceedings of the Institute of Radio Engineers*, vol. 24, no. 10, pp. 1367–1387, 1936.

[18] K. A. Norton, "The propagation of radio waves over the surface of the earth and in the upper atmosphere," *Proceedings of the Institute of Radio Engineers*, vol. 25, no. 9, pp. 1203–1236, 1937.

[19] K. A. Norton, "The calculation of ground-wave field intensity over a finitely conducting spherical earth," *Proceedings of the IRE*, vol. 29, no. 12, pp. 623–639, 1941.

[20] "IEEE standard definitions of terms for radio wave propagation," *IEEE Std 211-1997*, pp. i–, 1998.

[21] G. Apaydin and L. Sevgi, "Propagation modeling and path loss prediction tools for high frequency surface wave radars," *Turkish Journal of Electrical Engineering & Computer Sciences*, vol. 18, no. 3, pp. 469–484, 2010.

[22] G. N. Watson, "The diffraction of electric waves by the earth," *Proceedings of the Royal Society of London. Series A, Containing Papers of a Mathematical and Physical Character*, vol. 95, no. 666, pp. 83–99, 1918.

[23] J. Wait and L. Walters, "Curves for ground wave propagation over mixed land and sea paths," *IEEE Transactions on Antennas and Propagation*, vol. 11, no. 1, pp. 38–45, 1963.

[24] B. Kinsman, *Wind Waves: Their Generation and Propagation on the Ocean Surface*. Dover Books on Chemistry and Earth Sciences, Dover Publications, 1965.

[25] D. Barrick, "Remote sensing of sea state by radar," in *Engineering in the Ocean Environment, Ocean 72-IEEE International Conference on*, pp. 186–192, IEEE, 1972.

[26] T. Ponsford and J. Wang, "A review of high frequency surface wave radar for detection and tracking of ships," *Turkish Journal of Electrical Engineering & Computer Sciences*, vol. 18, no. 3, pp. 409–428, 2010.

[27] L. Sevgi, "Synthetic radar-signal environment: Computer generation of signal, noise, and clutter," *IEEE Antennas and Propagation Magazine*, vol. 49, no. 5, pp. 192–198, 2007.

[28] K. J. Hickey, E. W. Gill, J. A. Helbig, and J. Walsh, "Measurement of ocean surface currents using a long-range, high-frequency ground wave radar," *IEEE journal of oceanic engineering*, vol. 19, no. 4, pp. 549–554, 1994.

[29] C. Uluisik, G. Cakir, M. Cakir, and L. Sevgi, "Radar cross section (RCS) modeling and simulation, part 1: A tutorial review of definitions, strategies,

and canonical examples," *IEEE Antennas and Propagation Magazine*, vol. 50, no. 1, 2008.

[30] E. Knott, J. Schaeffer, and M. Tulley, *Radar Cross Section*. Electromagnetics and Radar Series, Institution of Engineering and Technology, 2004.

[31] L. Sevgi, A. Ponsford, and H. C. Chan, "An integrated maritime surveillance system based on high-frequency surface-wave radars. 1. theoretical background and numerical simulations," *IEEE Antennas and Propagation Magazine*, vol. 43, no. 4, pp. 28–43, 2001.

[32] G. Cakir, M. Cakir, and L. Sevgi, "Radar cross section (RCS) modeling and simulation, part 2: A novel FDTD-based RCS prediction virtual tool for the resonance regime," *IEEE Antennas and Propagation Magazine*, vol. 50, no. 2, pp. 81–94, 2008.

[33] L. Sevgi, "Target reflectivity and RCS interactions in integrated maritime surveillance systems based on surface-wave high-frequency radars," *IEEE Antennas and Propagation Magazine*, vol. 43, no. 1, pp. 36–51, 2001.

[34] L. Sevgi, "Target reflectivity and RCS modeling in HFSW radars," *IITRI Memorandum, May*, 1999.

[35] A. Ponsford, "Surveillance of the 200 nautical mile exclusive economic zone (EEZ) using high frequency surface wave radar (HFSWR)," *Canadian journal of remote sensing*, vol. 27, no. 4, pp. 354–360, 2001.

[36] S. Anderson, P. Edwards, P. Marrone, and Y. Abramovich, "Investigations with SECAR - a bistatic HF surface wave radar," in *Radar Conference, 2003. Proceedings of the International*, pp. 717–722, IEEE, 2003.

[37] S.-c. Wu, Z.-j. Yang, B.-y. Wen, Z. Shi, J. Tian, H. Gao, and X. Wu, "Test of HF ground wave radar OSMAR2000 at the eastern china sea," *JOURNAL-WUHAN UNIVERSITY NATURAL SCIENCES EDITION*, vol. 47, no. 1, pp. 111–117, 2001.

[38] Y. Hisaki, "Development of HF ocean radar in japan," in *Radar Conference, 2003. Proceedings of the International*, pp. 510–514, IEEE, 2003.

[39] D. E. Barrick, M. Evans, and B. Weber, "Ocean surface currents mapped by radar," *Science*, vol. 198, no. 4313, pp. 138–144, 1977.

[40] CODAR, "The SeaSonde." Brochure, March 2010.

[41] D. E. Barrick, "Fm/cw radar signals and digital processing," tech. rep., NATIONAL OCEANIC AND ATMOSPHERIC ADMINISTRATION BOULDER CO WAVE PROPAGATION LAB, 1973.

[42] D. E. Barrick, P. M. Lilleboe, and C. C. Teague, "Multi-station HF FMCW radar frequency sharing with GPS time modulation multiplexing," Feb. 15 2005. US Patent 6,856,276.

[43] K.-W. Gurgel, G. Antonischki, H.-H. Essen, and T. Schlick, "Wellen radar (WERA): a new ground-wave HF radar for ocean remote sensing," *Coastal engineering*, vol. 37, no. 3, pp. 219–234, 1999.

[44] T. Helzel, M. Kniephoff, and L. Petersen, "WERA: remote ocean sensing for current, wave and wind direction," in *2006 IEEE US/EU Baltic International Symposium*, pp. 1–8, IEEE, 2006.

[45] L. Wyatt, "HF radar for coastal monitoring - a comparison of methods and measurements," in *Oceans 2005-Europe*, vol. 1, pp. 314–318, IEEE, 2005.

[46] HELZEL, "Medium range remote ocean sensing system - 16 MHz." Brochure, September 2015.

[47] HELZEL, "Medium range remote ocean sensing system - 24-26 MHz." Brochure, September 2015.

[48] K.-W. Gurgel, "Wera guide," 2009. http://wera.cen.uni-hamburg.de/WERA_Guide/WERA_Guide.shtml.

[49] A. Ponsford, R. Dizaji, and Z. Ding, "An HF surface wave radar based integrated maritime surveillance system," in *The 34-th International Symposium METRA*, pp. 29–30, 2003.

[50] A. M. Ponsford, L. Sevgi, and H. C. Chan, "An integrated maritime surveillance system based on high-frequency surface-wave radars. 2. operational status and system performance," *IEEE Antennas and Propagation Magazine*, vol. 43, no. 5, pp. 52–63, 2001.

[51] A. M. Ponsford, R. M. Dizaji, and R. McKerracher, "HF surface wave radar operation in adverse conditions," in *Radar Conference, 2003. Proceedings of the International*, pp. 593–598, IEEE, 2003.

[52] R. Dizaji, T. Ponsford, and R. McKerracher, "Noise suppression system and method for phased-array based systems," Mar. 15 2005. US Patent 6,867,731.

[53] D. F. Reding, "The technological challenges of maritime information warfare," in *Microwaves, Communications, Antennas and Electronic Systems (COMCAS), 2015 IEEE International Conference on*, pp. 1–5, IEEE, 2015.

[54] J. Burger, D. O'Hagan, and A. Wilkinson, "Propagation and frequency selection considerations for high frequency surface wave radar," SATNAC, 2016.

[55] K. A. Norton, "System loss in radio-wave propagation," *Proc. IRE*, vol. 47, 1959.

[56] CCIR Rec., "Radio noise," Recommendation 372-9, International Telecommunication Union, Geneva, 2007.

[57] S. Rotheram, "Ground-wave propagation. part 1: Theory for short distances," in *IEE Proceedings F-Communications, Radar and Signal Processing*, vol. 128, pp. 275–284, IET, 1981.

[58] S. Rotehram, "Ground wave propagation, part 2: Theory for medium and long distances and reference propagation curves," in *IEE Proc. F. Commun. Radar & Signal Process*, vol. 128, pp. 285–295, 1981.

[59] B. R. Bean and E. Dutton, *Radio meteorology*. Dover Publications, 1966.

[60] CCIR Rec., "The radio refractive index: its formula and refractivity data," Recommendation 453-8, International Telecommunication Union, Geneva, 2001.

[61] J. Burger, D. O'Hagan, and A. Wilkinson, "High frequency surface wave radar demonstrator," SATNAC, 2017.

[62] R. McKerracher, P. Moo, and T. Ponsford, "Spectrum utilization: sense and adapt: operation on a noninterference and nonprotected basis," *IEEE Aerospace and Electronic Systems Magazine*, vol. 32, no. 12, pp. 30–34, 2017.

[63] T. Düsterwald, "Implementation of demonstrator riometer on a flexible FPGA backend - the first steps in adding a riometer mode to the superdarn radar at SANAE IV," Master's thesis, University of Cape Town, 2017.

[64] "Welcome to the red pitaya documentation," 2017. http://redpitaya.readthedocs.io/en/latest/index.html.

[65] C. Burger, *South African Radio League Introduction to Amateur Radio: A study guide for the Radio Amateur Examination*. South African Radio League (SARL), 2016.

[66] Mini-Circuits®, P.O. Box 350166, Brooklyn, New York, *Coaxial Low Noise Amplifier ZFL-500HLN+ ZFL-500HLN*, May 2007.

[67] Mini-Circuits®, P.O. Box 350166, Brooklyn, New York, *Coaxial Low Noise Amplifier ZFL-500LN+ ZFL-500LN*, July 2010.

[68] D. Barrick, "Miniloop antenna operation and equivalent circuit," *IEEE transactions on antennas and propagation*, vol. 34, no. 1, pp. 111–114, 1986.

[69] D. H, "Wide range tunable transmitting loop antenna," June 28 1971. US Patent 3,588,905.

[70] E. C. Jordan and C. Andrews, "Electromagnetic waves and radiating systems," *American Journal of Physics*, vol. 19, no. 8, pp. 477–478, 1951.

[71] R. C. Johnson and H. Jasik, "Antenna engineering handbook," *New York, McGraw-Hill Book Company, 1984, 1356 p. No individual items are abstracted in this volume.*, pp. 3–1 to 3–12, 1984.

[72] D. E. Barrick and B. J. Lipa, "Evolution of bearing determination in hf current mapping radars," *Oceanography*, vol. 10, no. 2, pp. 72–75, 1997.

[73] R. H. Khan and D. Mitchell, "Waveform analysis for high-frequency fmicw radar," in *IEE Proceedings F (Radar and Signal Processing)*, vol. 138, pp. 411–419, IET, 1991.

[74] R. Khan, B. Gamberg, D. Power, J. Walsh, B. Dawe, W. Pearson, and D. Millan, "Target detection and tracking with a high frequency ground wave radar," *IEEE Journal of Oceanic Engineering*, vol. 19, no. 4, pp. 540–548, 1994.

[75] D. Barrick, B. Lipa, P. Lilleboe, and J. Isaacson, "Gated fmcw df radar and signal processing for range/doppler/angle determination," Nov. 1 1994. US Patent 5,361,072.

[76] L. R. Wyatt, J. J. Green, A. Middleditch, M. D. Moorhead, J. Howarth, M. Holt, and S. Keogh, "Operational wave, current, and wind measurements with the pisces hf radar," *IEEE Journal of Oceanic Engineering*, vol. 31, no. 4, pp. 819–834, 2006.

[77] S. Mahabeer, *Extending the HF Radar Capabilities to Monostatic and FMiCW*. Bachelor's thesis, University of Cape Town, 2017.

[78] F. Raab, "Idealized operation of the class e tuned power amplifier," *IEEE transactions on Circuits and Systems*, vol. 24, no. 12, pp. 725–735, 1977.

[79] N. O. Sokal and A. D. Sokal, "Class E-A new class of high-efficiency tuned single-ended switching power amplifiers," *IEEE Journal of solid-state circuits*, vol. 10, no. 3, pp. 168–176, 1975.

[80] A. J. Wilkinson and J. K. Everard, "Transmission-line load-network topology for class-e power amplifiers," *IEEE Transactions on microwave theory and techniques*, vol. 49, no. 6, pp. 1202–1210, 2001.

[81] J. Everard and A. King, "Broadband power efficient class E amplifiers with a non-linear CAD model of the active MOS device," *Journal of the Institution of Electronic and Radio Engineers*, vol. 57, no. 2, pp. 52–58, 1987.